

**UNDERSTANDING OXYGEN VACANCY FORMATION, INTERACTION, TRANSPORT,
AND STRAIN IN SOFC COMPONENTS VIA COMBINED THERMODYNAMICS AND
FIRST PRINCIPLES CALCULATIONS**

By

Tridip Das

A DISSERTATION

Submitted to
Michigan State University
in partial fulfillment of the requirements
for the degree of

Chemical Engineering-Doctor of Philosophy

2017

ABSTRACT

UNDERSTANDING OXYGEN VACANCY FORMATION, INTERACTION, TRANSPORT, AND STRAIN IN SOFC COMPONENTS VIA COMBINED THERMODYNAMICS AND FIRST PRINCIPLES CALCULATIONS

By

Tridip Das

Understanding of the vacancy formation, interaction, increasing its concentration and diffusion, and controlling its chemical strain will advance the design of mixed ionic and electronic conductor (MIEC) materials via element doping and strain engineering. This is especially central to improve the performance of the solid oxide fuel cell (SOFC), an energy conversion device for sustainable future.

The oxygen vacancy concentration grows exponentially with the temperature at dilute vacancy concentration but not at higher concentration, or even decreases due to oxygen vacancy interaction and vacancy ordered phase change. This limits the ionic conductivity. Using density functional theory (DFT), we provided fundamental understanding on how oxygen vacancy interaction originates in one of the typical MIEC, $\text{La}_{1-x}\text{Sr}_x\text{FeO}_{3-\delta}$ (LSF). The vacancy interaction is determined by the interplay of the charge state of multi-valence ion (Fe), aliovalent doping (La/Sr ratio), the crystal structure, and the oxygen vacancy concentration and/or nonstoichiometry (δ). It was found excess electrons left due to the formation of a neutral oxygen vacancy get distributed to Fe directly connected to the vacancy or to the second nearest neighboring Fe, based on crystal field splitting of Fe $3d$ orbital in different Fe-O polyhedral coordination. The progressively larger polaron size and anisotropic shape changes with increasing Sr-content resulted in increasing oxygen vacancy interactions, as indicated by an increase in the oxygen vacancy formation energy above a critical δ threshold. This was consistent with experimental results showing that Sr-rich LSF and highly oxygen deficient compositions are prone to oxygen-vacancy-

ordering-induced phase transformations, while Sr-poor and oxygen-rich LSF compositions are not. Since oxygen vacancy induced phase transformations, cause a decrease in the mobile oxygen vacancy site fraction (X), both δ and X were predicted as a function of temperature and oxygen partial pressure, for multiple LSF compositions and phases using a combined thermodynamics and DFT approach. A detailed oxygen vacancy migration barrier calculation gave the oxygen ionic diffusivity and conductivity.

Oxygen vacancy also causes chemical strain, which was treated as a scalar in the literature. However, in many materials, it should be a tensor, which is anisotropic. We illustrate this effect on CeO_2 , in which it explained a puzzling experiment, which shows significant amplification of measured strain on applied bias in non-stoichiometric Gd doped ceria. The presence of highly localized $4f$ valence orbital in Ce causes charge disproportionation on the formation of neutral oxygen vacancy, producing anisotropic chemical strain in ceria with cubic symmetry. Understanding of δ and X and anisotropic chemical strain in the lattice has led to the design of better MIEC via element doping and strain engineering of the lattice.

Copyright by
TRIDIP DAS
2017

Dedicated to the Tax Payers of United States of America
(for funding my research)

ACKNOWLEDGEMENTS

I am grateful to my advisor Prof. Yue Qi for introducing me to the world of atomistic modeling. She taught me density functional theory (DFT) and helped me to learn many more computational recipes by challenging my abilities. I also want to thank Prof. Jason D. Nicholas for his constant guidance and motivation. I am grateful to my advisors for their effort and desire to help me whenever I needed their support, even on the weekends. I want to thank my committee member Prof. Wei Lai and Prof. Benjamin Levine for their valuable inputs in my thesis work.

I acknowledge the funding from National Science Foundation (Award Number DMR-1410850, National Science Foundation CAREER Award No. CBET-1254453), and from Department of Energy (Award Number DE-FE0023315).

I also acknowledge my colleagues, friends, families and high performance computing center (HPCC) of Michigan State University for their support.

TABLE OF CONTENTS

<i>LIST OF TABLES.....</i>	<i>ix</i>
<i>LIST OF FIGURES.....</i>	<i>x</i>
1. Introduction.....	1
1.1 <i>Factors Influencing Oxygen Vacancy Formation in Perovskite.....</i>	<i>6</i>
1.2 <i>Oxygen Vacancy Interaction via Vacancy Polaron.....</i>	<i>11</i>
1.3. <i>Effect of the oxygen vacancy interaction on Ionic conductivity at SOFC operating conditions.....</i>	<i>13</i>
1.4. <i>Anisotropic Chemical Strain Effect Due to Oxygen Vacancy Polaron.....</i>	<i>15</i>
2. Computational Details: Methodology developed and Used.....	17
2.1. <i>Magnetic Moment Interpreted Oxidation State Prediction</i>	<i>18</i>
2.1.1. <i>Selection of U Parameter.....</i>	<i>19</i>
2.1.2. <i>Determining Oxidation State on Fe</i>	<i>23</i>
2.1.3. <i>Advantage over Bader Charge.....</i>	<i>24</i>
2.2. <i>Determining Polaron Shape and Size from the Valance Change on Transition Metal</i>	<i>26</i>
2.3. <i>Calculation Method of Oxygen Vacancy Formation and Migration Barrier Energy ..</i>	<i>27</i>
2.3.1. <i>Oxygen Vacancy Formation Energy at 0 K.....</i>	<i>27</i>
2.3.2. <i>Predicting Vacancy Ordered Phase Transition.....</i>	<i>28</i>
2.3.3. <i>Calculating Oxygen Vacancy Migration Barrier</i>	<i>29</i>
2.4. <i>Thermodynamic Extension of DFT Calculated Energies</i>	<i>30</i>
2.4.1. <i>Converting Vacancy Formation Energy to Vacancy Formation Free Energy.....</i>	<i>30</i>
2.4.2. <i>Connecting Chemical Potential of Oxygen from 0 K to T K.....</i>	<i>31</i>
2.5. <i>Predicting Ionic Conductivity as a Function of Temperature and Phase Change in Air.</i>	<i>36</i>
2.5.1. <i>Oxygen Vacancy Concentration in Bulk Lattice.....</i>	<i>36</i>
2.5.2. <i>Mobility and Diffusivity of Oxygen Vacancy in Bulk Lattice.....</i>	<i>37</i>
2.6. <i>Anisotropic Chemical Strain Due to Oxygen Vacancy</i>	<i>37</i>
3. DFT+U as a Reliable Tool to Predict Lattice Structure and Electronic Properties of MIEC at Low Temperature.....	41
3.1 <i>Predicting Ground State Lattice Structure and Magnetic Ordering in $La_{1-x}Sr_xFeO_{3-\delta}$ Phases</i>	<i>42</i>
3.2. <i>Density of States for $LaFeO_{3-\delta}$ and $La_{0.5}Sr_{0.5}FeO_{3-\delta}$.....</i>	<i>43</i>
3.3. <i>Study of Different $SrFeO_{3-\delta}$ Phases.....</i>	<i>45</i>
3.3.1 <i>Magnetic Orientations of $SrFeO_{3-\delta}$ Phases.....</i>	<i>47</i>
3.3.2. <i>Density of States for $SrFeO_{3-\delta}$ Phases.....</i>	<i>48</i>
3.3.3. <i>Formation Enthalpy of Brownmillerite $SrFeO_{2.5}$.....</i>	<i>49</i>
3.3.4. <i>d-Orbital Splitting and Its Impact on the Iron Oxidation State</i>	<i>49</i>
3.3.5. <i>Solving the Debate on Fe Oxidation State at Square Pyramidal and Octahedral Sites</i>	<i>50</i>

<i>3.4. Choices of Crystal Structures at SOFC Operating Temperature</i>	51
<i>4. Oxygen Vacancy Interaction via Vacancy Polaron.....</i>	53
<i>4.1. Origin of Long Range Charge Transfer due to Oxygen Vacancy Polaron.....</i>	53
<i>4.2. Oxygen Vacancy Polaron in Different $La_{1-x}Sr_xFeO_{3-\delta}$ Phases.....</i>	55
<i>4.2.1. $LaFeO_{3-\delta}$.....</i>	56
<i>4.2.2. $SrFeO_{3-\delta}$.....</i>	58
<i>4.2.3. Rhombohedral and Cubic $La_{0.5}Sr_{0.5}FeO_{3-\delta}$.....</i>	61
<i>5. Oxygen Vacancy Formation sites and Formation Energy for Interacting and Non-interacting Vacancies at 0 K.....</i>	63
<i>5.1. Oxygen Vacancy Formation Sites in $SrFeO_{3-\delta}$ Phases</i>	63
<i>5.2. Oxygen Vacancy Formation Energies in $SrFeO_{3-\delta}$ Phases.....</i>	66
<i>5.3. Computationally Predicted Vacancy Ordered Phase Transition in $SrFeO_{3-\delta}$ Phases.....</i>	68
<i>6. Oxygen Vacancy Site Fraction as a Function of Temperature and Phase Change (in air) .</i>	72
<i>6.1. Oxygen Vacancy Site Fractions in Different $SrFeO_{3-\delta}$ Phases Predicted with Temperature in Air.....</i>	73
<i>6.2. Oxygen Vacancy Site Fractions in Different LSF Compositions Predicted with Temperature in Air.....</i>	76
<i>6.3. Effect of the Variation of U-Parameter on Oxygen Vacancy Formation</i>	79
<i>7. Oxygen Ionic Conductivity in $La_{1-x}Sr_xFeO_{3-\delta}$ – Considering Oxygen Vacancy Interaction and Phase Change</i>	82
<i>7.1 Oxygen Vacancy Migration in $La_{1-x}Sr_xFeO_{3-\delta}$</i>	83
<i>7.1.1 Oxygen Vacancy Migration in $LaFeO_{3-\delta}$</i>	84
<i>7.1.2 Oxygen Vacancy Migration in $La_{0.5}Sr_{0.5}FeO_{3-\delta}$.....</i>	85
<i>7.1.3 Oxygen Vacancy Migration in $SrFeO_{3-\delta}$.....</i>	88
<i>7.2 Oxygen Ionic Conductivity in $La_{1-x}Sr_xFeO_{3-\delta}$ as a Function of Temperature (in Air) ..</i>	92
<i>8. Anisotropic Chemical Strain Produced by Non-Stoichiometric Cubic $CeO_{2-\delta}$.....</i>	95
<i>8.1 Charge Disproportionation in Non-stoichiometric Ceria</i>	95
<i>8.2 PDOS of Perfect and Oxygen Vacancy Adjacent Ce</i>	97
<i>8.3 Calculating Anisotropic Chemical Strain.....</i>	99
<i>9. Conclusion and Future Work.....</i>	102
<i>9.1 Thesis Summary and Conclusion</i>	102
<i>9.2 Future Work</i>	104
<i>APPENDIX.....</i>	107
<i>BIBLIOGRAPHY.....</i>	110

LIST OF TABLES

Table 2.1. Spin-polarized Bader charge analysis of different LSF phases. Magnetic moment calculated by VASP and expected formal charge on Fe are also provided for comparison.....	25
Table 3.1. DFT predictions of stable LSF structures under ground-state conditions.	41
Table 3.1. Comparison of DFT-calculated and experimentally-measured lattice parameters, magnetic ordering, and band gaps for several phases of $\text{SrFeO}_{3-\delta}$ (“See DOS” in the last column of below-provided table refer to the Figure 3.1 for the density of states plot). N.C. stands for Not Calculated. Experimental Néel Temperature, T_N , is also listed for each phase.....	45
Table 5.1. The vacancy formation energies at different oxygen site calculated for all four crystalline structures. Each site is noted by its label in Figure 1.1, its position in Fe-O polyhedra, and the charge of the Fe ions in the Fe-O polyhedra. The bold values indicate the most favorable oxygen vacancy site.....	64
Table 8.1. Comparing calculated energy and bond lengths for different Vo-formation cases....	95

LIST OF FIGURES

Figure 1.1. Vacancy ordered phases of $SrFeO_{3-\delta}$: (a) cubic, (b) tetragonal, (c) orthorhombic, and (d) brownmillerite with increasing oxygen non-stoichiometry. The energetically favorable sites for vacancy creation are highlighted with dashed red circles. Fe-O polyhedra are colored according to the calculated charge state on Fe, as shown in the legend, with Fe-O octahedra and square pyramids containing $Fe^{+3.9}$ or Fe^{+4} dark brown, Fe-O octahedra containing $Fe^{+3.6}$ yellowish-green; $Fe^{+3.3}$ light purple; Fe^{+3} light brown, and Fe-O tetrahedra containing $Fe^{+3.2}$ light orange.	8
Figure 2.1. DFT calculated lattice structures for (a) orthorhombic $LaFeO_3$, (b) rhombohedral $La_{0.5}Sr_{0.5}FeO_3$, (c) cubic $La_{0.5}Sr_{0.5}FeO_3$ (high temperature phase), and (d) cubic $SrFeO_3$. Atoms are colored as La – green, Sr - blue, Fe – brown, O – red. The different Fe-O ₆ octahedra colors denote polyhedra with different Fe charge states: Fe^{3+} – light brown, $Fe^{3.5+}$ – moss green, Fe^{4+} – dark brown.	18
Figure 2.2. The plot of (a) magnetic moment and (b) lattice parameters as a function of U_{eff} parameter. The straight lines are experimental data, and blue and red correspond to the data for $SrFeO_3$ and $LaFeO_3$, respectively. Since $LaFeO_3$ is not cubic, red, green and pink colors in (b) are corresponding to scaled-lattice ($a/\sqrt{2}$, $b/2$, $c/\sqrt{2}$ respectively) of $LaFeO_3$.	20
Figure 2.3. Black squares represent the formal charge on Fe resulting from different La/Sr ratios in $La_xSr_{1-x}FeO_3$ calculated from the magnetic moment on Fe with a GGA+U(=3) (left y-axis). Blue diamonds show experimentally measured average Fe charge states for varying La/Sr ratios (right y-axis). The black dotted line represents the predicted linear relationship between the Fe charge state and the La/Sr ratio.	23
Figure 2.4. Compare different methods to obtain oxygen connection energy in Equation 2.5...	35
Figure 2.5. (a) CeO_2 unit cell showing O-Ce ₄ tetrahedral coordination and Ce-O bonding directions. (b) Charge distribution on Ce around neutral oxygen vacancy formation showing in a 2x2x2 supercell.	38
Figure 3.1. GGA+U (=3) partial density of states calculations for (a-b) orthorhombic $LaFeO_3$, (c-d) rhombohedral $La_{0.5}Sr_{0.5}FeO_3$. The gray and black lines represent the Fe 3d and O 2p states respectively.	44
Figure 3.2. GGA+U ($U_{eff} = 3$) PDOS for four different $SrFeO_{3-\delta}$ phases. The gray and black line represent Fe 3d and O 2p states respectively. The stoichiometric $SrFeO_3$ has shown metallic behavior. Whereas, band gaps are observed in oxygen deficient phases.	46
Figure 3.3. Crystal Field Theory explains d-orbital splitting and electronic distribution for different Fe-O polyhedra. (a) Square pyramidal Fe-O coordination, (b) octahedral Fe-O coordination (c) Compressed octahedral Fe-O coordination with Jahn-Teller distortion.	50

Figure 4.1. The charge distribution on Fe due to oxygen vacancy formation is described on vacancy containing lattice plane of a $4 \times 4 \times 4$ cubic SrFeO_3 supercell with a single oxygen vacancy at the center of the cell. Figure (a) is the lattice plane without relaxing the atom position (only electron cloud is allowed to relax after vacancy formation). Figure (b) is the lattice plane containing atoms after relaxing the atom positions. The light brown atoms are Fe and red atoms are O. The light blue Sr atoms are above or below the described planes. The oxygen vacancy is denoted with a black dot. Figure (a) and (b) contains the oxygen vacancy at the center of the (200) lattice plane. The charge on every Fe atom, rounded to the nearest tenth, is listed next to each Fe atom..... 53

Figure 4.2. Long-range charge transfer areas (denoted by the purple dashed lines in a-d) and perspective views of the $\text{La}_x\text{Sr}_{1-x}\text{FeO}_3$ lattice polarons (e-h) for (a, e) orthorhombic LaFeO_3 , (b,f) rhombohedral $\text{La}_{0.5}\text{Sr}_{0.5}\text{FeO}_3$, (c,g) cubic $\text{La}_{0.5}\text{Sr}_{0.5}\text{FeO}_3$, and (d,h) cubic SrFeO_3 . Note, in (a-d) different Miller planes were used for each phase to compare lattice orientation with same visual conformity. In (e-h) the polaron shape was highlighted by only drawing sides to those Fe-O polyhedra with a Fe atom that received excess electrons due to oxygen vacancy formation. In (a-d), the black lines indicate the border of the supercells used for computations, while the arrows provide an estimate of the polaron size by denoting the distance from the outermost charge-altered Fe atoms to the oxygen vacancy site. 56

Figure 4.3. Schematic of the d-orbital splitting in the Fe in different polyhedra showing that the excess electrons generated during oxygen vacancy formation (in red) will be localized to oxygen vacancy adjacent square pyramidal Fe in orthorhombic LaFeO_3 (a), and transferred to second nearest neighboring octahedral Fe in cubic SrFeO_3 (b). 57

Figure 4.4. Oxygen vacancy polaron shape in (a) tetragonal, (b) orthorhombic, (c) brownmillerite $\text{SrFeO}_{3-\delta}$. Fe-O polyhedra colored according to the charge on Fe.²⁷ Here, blue atoms are Sr, brown are Fe and red are O. 60

Figure 4.5. d-orbital splitting and energy distribution for different Fe-O polyhedra was derived from crystal field theory. (a) Square planar Fe-O coordination, (b) octahedral FeO coordination (c) tetrahedral Fe-O coordination. 60

Figure 5.1. The vacancy formation energy per oxygen vacancy, calculated from DFT for four different $\text{SrFeO}_{3-\delta}$ phases. 66

Figure 5.2. Energy required $\Delta E\delta$ to form the non-stoichiometric structures $(\text{SrFeO}_{3-\delta} + \frac{\delta}{2}\text{O}_2)$ from cubic SrFeO_3 68

Figure 5.3. GGA+U calculated oxygen vacancy formation energies for different $\text{La}_x\text{Sr}_{1-x}\text{FeO}_3$ compositions. The Fe-O polyhedra represent the charge on Fe in a perfect lattice. The lines are guides to the eye. 69

Figure 6.1. Dotted line represent δ increasing with T at $p\text{O}_2 = 0.21$ atm according to Equation 1.6 (dilute vacancy assumption) for cubic $\text{SrFeO}_{3-\delta}$ (ΔE_{vacf} from Figure 5.1 for different δ). Solid line represent δ increasing with T at atmospheric condition according to Equation 2.17 (interacting vacancy assumption) for cubic $\text{SrFeO}_{3-\delta}$ (where ΔE_{vacf} is a function of δ). 72

Figure 6.2. (a) Vacancy formation free energy with nonstoichiometry for all the phases (b) Nonstoichiometry is plotted as a function of temperature. (c) Vacancy formation site fraction is plotted as a function of temperature. (the data point corresponding to $3X_{\text{cubic}} = 0.5$ is neglected from fitting as at this vacancy site fraction cubic $\text{SrFeO}_{3-\delta}$ is easily transformed to brownmillerite and hence loses its available vacancy sites). 73

Figure 6.3. (a) The oxygen non-stoichiometry versus temperature in air,(b) the oxygen vacancy site fraction as a function of temperature in air, and (c) the oxygen vacancy site fraction as a function of temperature and La/Sr ratio for various $\text{La}_x\text{Sr}_{1-x}\text{FeO}_3$ phases. Note, the lines in (a-b) and are guides to the eye and the lines in (c) are the experimentally determined phase boundaries.^{44,65} The oxygen vacancy site fraction in (c) is denoted by the color overlay and the right-hand color scale. The X values in b) and c) are never zero. They are just smaller than can be resolved with the linear X scale chosen to highlight the X trends discussed here..... 77

Figure 6.4. (a) Compare the impact of U parameters on oxygen vacancy formation energy as a function of oxygen nonstoichiometry; (b) compare the calculated oxygen nonstoichiometry as a function of temperature with different U parameters with experimental values. 80

Figure 7.1. Oxygen migration in $\text{LaFeO}_{3-\delta}$. The pink atoms in (a) highlight the oxygen migration path, (b) shows the oxygen migration barrier along this path for two different δ , and (c) shows the charge change on the neighboring Fe atoms as a function of oxygen atom coordinate on its path (at $\delta = 0.06$). 85

Figure 7.2. Oxygen migration in LSF55. The pink atoms in (a) highlight the oxygen migration path in Rhombohedral LSF55 with $\delta = 0.04$, and (b) highlight the oxygen migration path in cubic LSF55 with $\delta = 0.13$. Figure (c) shows the oxygen migration barrier in rhombohedral and cubic LSF55. (d) shows the charge change on the oxygen vacancy neighboring Fe atoms in rhombohedral LSF55 as a function of oxygen atom coordinate (corresponds to Figure (a)). Figure (e) shows the charge change on the oxygen vacancy neighboring Fe atoms in cubic LSF55 as a function of oxygen atom coordinate (corresponds to Figure (b)). 87

Figure 7.3. Oxygen migration in cubic $\text{SrFeO}_{3-\delta}$. The pink atoms in Figure (a) highlight the oxygen migration path, Figure (b) shows the oxygen migration barrier along this path for two different δ , and Figure (c) shows the charge change on the neighboring Fe atoms as a function of oxygen atom coordinate on its path. 89

Figure 7.4. Oxygen migration in tetragonal $\text{SrFeO}_{3-\delta}$. (Left) non-red smaller atoms highlights the oxygen migration paths. Paths are defined with Wyckoff positions of oxygen atoms in the perfect lattice; P1: $4c \rightarrow 16k \rightarrow 8h \rightarrow 16k \rightarrow 4c$; P2: $4c \rightarrow 16k \rightarrow 16m \rightarrow 16k \rightarrow 4c$; P3: $4c \rightarrow 16k \rightarrow 4c$. (Right) oxygen migration barrier at different coordinates (ζ) of the path. 90

Figure 7.5. Oxygen migration in orthorhombic $\text{SrFeO}_{3-\delta}$. (Left) non-red smaller atoms highlight the oxygen migration paths. Paths are defined with Wyckoff positions of oxygen atoms in the perfect lattice; P1: $2b \rightarrow 16r \rightarrow 16r \rightarrow 2b$ (c-direction); P2: $2b \rightarrow 16r \rightarrow 4j \rightarrow 16r \rightarrow 2b$; P3: $2b \rightarrow 16r \rightarrow 16r \rightarrow 2b$ (a-direction). (Right) oxygen migration barrier at different coordinates (ζ) of the path. 90

Figure 7.6. Oxygen vacancy (a) concentration (b) ion diffusivity, and (c) ion conductivity in different LSF compositions as a function of temperature in air. In Figure legends ‘cubic SFO’ represent cubic $\text{SrFeO}_{3-\delta}$ data. ‘other SFO’ represent combined data for tetragonal, orthorhombic, and brownmillerite phase in Figure 7.6(a) and tetragonal and orthorhombic phases in Figure 7.6(b,c). ‘LSF55(combined)’ represents the LSF55 data with phase change from rhombohedral to cubic. ‘rhomb LSF55’ in Figure 7.6(c) represent the computed oxygen ionic conductivity data for rhombohedral LSF55 phase..... 91

Figure 8.1. Charge distribution on Ce and displacement of O-atoms around neutral oxygen vacancy (V_O^{--}). Red-O moved away from oxygen vacancy site. Green-O came closer to oxygen vacancy site. Red Ce-O bond signify elongation with respect to bond length in perfect structure and blue Ce-O bond signify contraction..... 96

Figure 8.2. Partial density of states plot for Ce-5s, 5p, 5d, 4f and O-2p orbitals in pure CeO_2 . 97

Figure 8.3.(a) PDOS for Ce^{4+} -5d and Ce^{4+} -4f orbital for Ce^{4+} adjacent to V_O^{--} , after V_O^{--} formation in asymmetric case. Orbitals show same shape as Ce^{4+} in perfect CeO_2 .(b) PDOS for Ce^{3+} -5d and Ce^{3+} -4f orbital for Ce^{3+} adjacent to V_O^{--} , after V_O^{--} formation in asymmetric case. Figure shows localization of excess electron in 4f orbital. .(c) PDOS for $\text{Ce}^{3.5+}$ -5d and $\text{Ce}^{3.5+}$ -4f orbital for $\text{Ce}^{3.5+}$ adjacent to V_O^{--} , after V_O^{--} formation in symmetric case. Figure shows localization of excess electron in 4f orbital. This scenario is computational artifact as the structure was energetically unfavorable. 98

Figure 8.4. The oxygen vacancy formation energy varies with an applied strain in different directions. The slope of the strain versus energy curve gives the elastic dipole tensor mapped with applied strain direction..... 99

Figure 8.5.(a) Average expansion of single crystal ceria with increasing oxygen nonstoichiometry. (b) possible orientations of Ce^{3+} and Ce^{4+} atoms around oxygen vacancy..... 101

Figure 9.1. Ruddlesden-Popper type $\text{Sr}_3\text{Fe}_2\text{O}_7$ lattice with single oxygen vacancy (black atom) at the center. Blue, brown, and red atoms are Sr, Fe, and O respectively. $\text{Sr}_3\text{Fe}_2\text{O}_7$ can be a promising compound for low-temperature SOFC cathode..... 105

Figure 9.2. Crystal structure of 12.5% Gd/Sm/Pr (purple atoms) doped ceria (GDC/SDC/PDC). Here, Ce and O atoms are colored in yellow and red respectively. Gd/Sm/Pr atoms are randomly distributed in the lattice. 106

1. Introduction

Mixed Ionic Electronic Conductor (MIEC) oxides are used for a variety of electrochemical devices including gas sensors,¹ gas separation membranes,² memristors,³ solid oxide fuel cell (SOFC) electrode,⁴⁻⁷ opto-electronics⁸ etc. Different MIEC oxides with their aforementioned applications can be summarized by their usability as components of a single device, SOFC. It is a chemical to electrical energy conversion device suitable for a sustainable future, due to its high energy conversion efficiency, fuel flexibility and low cost.⁹ In a SOFC device, oxygen from air gets incorporated in the surface layer of the cathode as oxygen ion by receiving two electrons from the cathode (transported through external circuit). Then the oxygen ion transports through cathode, electrolyte, anode, and to the anode surface, where it reacts with the fuel, producing water and electricity (if the fuel is hydrogen) or carbon-di-oxide, water, and electricity (if the fuel is natural gas or syngas). Based on the type of MIEC compound, electronic or oxygen ionic transport prevails over one another.^{10,11} For example, the SOFC electrolyte is desired to transport only oxygen ion through it and it should block the transport of the electron. Therefore, fluorite type compounds: CeO_{2-δ},¹² Gd_{1-x}Ce_xO_{2-δ} (GDC),¹³ Pr_{1-x}Ce_xO_{2-δ} (PDC),¹⁴ Sm_{1-x}Ce_xO_{2-δ} (SDC),¹⁵ or Y_{1-x}Zr_xO_{2-δ} (YSZ)¹⁶ etcetera with fast oxygen ion conductivity are used as SOFC electrolyte. Whereas, SOFC electrodes are desired to have good electron and oxygen ion conductivity.⁴ As a result compounds of ABO₃ perovskite family: La_{1-x}Sr_xFeO_{3-δ} (LSF),¹⁷ La_{1-x}Sr_xCoO_{3-δ} (LSC),¹⁸ La_{1-x}Sr_xCo_{1-y}Fe_yO_{3-δ} (LSCF),⁷ La_{1-x}Sr_xMnO_{3-δ} (LSM),¹⁹ La_{1-x}Sr_xCo_{1-y}Mn_yO_{3-δ} (LSCM),²⁰ Sm_{1-x}Sr_xCoO_{3-δ} (SSC),²¹ Ba_{1-x}Sr_xCo_{1-y}Fe_yO_{3-δ} (BSCF)² etcetera serve as the main component for SOFC electrode. Though conventional cathode was produced in a combination of good electronic conductor, LSM mixed with GDC, a good ionic conductor²² LSF or LSCF can independently work as a MIEC cathode.²³

Unfortunately, the performance of these MIEC compounds is often limited by poor oxygen ion transport within the material at low temperature (600°C or less).²⁴ To maintain desired oxygen

ionic conductivity, it is required to operate the SOFC at high temperature (800-1000°C), which causes premature aging for different SOFC components.^{25,26} Further, oxygen ion conductivity does not exponentially increase with temperature due to oxygen vacancy interaction at higher vacancy concentration.²⁷⁻²⁹ Therefore, to improve the performance of these MIEC compounds at low temperature via doping or lattice strain engineering, we need a thorough understanding of how different parameters (discussed later) regulate the oxygen ion conductivity in the MIEC. The oxygen ion conductivity consists of three components, as shown in Equation 1.1.

$$\sigma = cZe\mu \quad [1.1]$$

Where c is the vacancy concentration. Z is the charge on an ion as a multiple of e (the charge of an electron), and μ , known as the mobility of the ion. Oxygen vacancy formation and their self-interaction directly regulate oxygen vacancy concentration and oxygen ion diffusivity. Local charge redistribution (after oxygen vacancy formation) on (vacancy neighboring) transition metal and local lattice deformation around the vacancy-site (aka chemical strain field) causes oxygen vacancy interaction at a higher vacancy concentration, which largely influences the performance of these MIECs at high temperature. This thesis will investigate the oxygen vacancy formation, interaction, transport, and its' chemical strain effect in SOFC components with a focus on two important members of oxide families: perovskite type, LSF, and fluorite type, $\text{CeO}_{2-\delta}$.

Many factors influence the oxygen vacancy formation and migration in perovskite LSF. These factors include the La/Sr ratio, phase change, charge distribution on multivalent Fe, and the interactions between the oxygen vacancies in LSF. These factors jointly impact the variation in oxygen ionic conductivity in LSF at SOFC operating conditions.^{17,24,30,31} To fully understand the complicated interplay among oxygen non-stoichiometry, δ , the varying charge on Fe around oxygen vacancy site, and phase change, several computational challenges have to be solved.¹⁷ First, it was difficult to predict the Fe oxidation state when Fe is present in a lattice with multiple

valences.^{32–36} With an accurate prediction of the Fe oxidation state in this thesis, the change in Fe oxidation state can be used to illustrate the excess electron distribution due to oxygen vacancy formation. The excess electron is also called “polaron”, whose shape and volume were used to explain the oxygen vacancy interaction. The interacting oxygen vacancy can lead to increasing vacancy formation energy with vacancy concentration, which means the vacancy cannot be treated as dilute defects anymore. Therefore, a new computational model is required and was developed in this thesis, to predict oxygen vacancy concentration dependent nonstoichiometry in both dilute and non-dilute cases. Using computationally predicted oxygen vacancy concentration and migration barrier data, the oxygen ionic conductivity can be calculated for LSF as a function of temperature and phase change, in the air. These results will be used to explain the loss of oxygen conductivity due to vacancy ordered phase transition observed in experiments.^{37,38}

Oxygen vacancy induced chemical strain in the lattice plays a significant role in mechanical failure at the electrode-electrolyte interface of SOFC. To enhance the mechanical compatibility between different parts and to arrest the failure at the interface, it is important to understand how the oxygen vacancy produces this chemical strain. Previous experimental study³⁹ investigated local lattice distortion and hypothesized anisotropic lattice distortion due to oxygen vacancy in a cubic $\text{CeO}_{2-\delta}$, but couldn't clearly explain the complicated lattice distortion. Due to the cubic symmetry of these fluorite structures, earlier computational studies calculated average chemical strain in place of complete strain tensor.^{40,41} As a result, they could not capture the anisotropic chemical strain in the cubic lattice. Therefore, previous experimental and computational studies could not provide a detailed explanation for the origin of huge chemical strain in GDC thin film on the application of electric field. This thesis will illustrate the reason behind anisotropic chemical strain with quantification of it in cubic ceria and explain the complicated lattice distortion around oxygen

vacancy. The fundamental reason behind the origin of the chemical strain tensor and its tensorial relationship with the crystallographic orientation of the lattice will help for better development of the SOFC electrolyte and phase shift device.⁴²

In summary, this thesis elucidates the role of oxygen vacancy formation, interaction and transport, which defines the performance of the MIEC compounds (SOFC components) at SOFC operating conditions, using first principle calculations combined with the thermodynamic approach. In the rest of Chapter 1, the present challenges and existing literature are discussed for specific materials and topics in more details. The rest of the thesis will be arranged as the following:

Chapter 2 introduced newly developed computational methods required for this study used to solve the defined challenges. For density functional theory (DFT) calculations, Hubbard-U parameter was selected based on the experimental magnetic moment and lattice length, to correctly predict the charge on multivalent Fe. Magnetic moment based charge prediction method for multivalent Fe solved a long-standing debate in literature for charge assignment in a lattice containing both Fe^{3+} and Fe^{4+} . This chapter also introduced the method to calculate oxygen vacancy polaron shape and size from valence change on transition metal. The methods to calculate oxygen vacancy formation energy and migration energy barrier with varying nonstoichiometry were also described. A new thermodynamic method developed to calculate oxygen vacancy site fraction, X for interacting vacancies was introduced. Methods to calculate oxygen vacancy concentration, ionic diffusivity, mobility and finally ionic conductivity were described. The derivation for anisotropic chemical strain tensor from energy change due to local deformation and the long-range elastic strain was also introduced in this chapter.

In Chapter 3, the reliability of first-principle calculations as a useful tool to predict ground state properties of different LSF compositions and phases was established by comparing the computed lattice structures, electronic properties like magnetic ordering and band gaps with experiments. This chapter also described all the LSF compositions and phases used in this thesis.

In Chapter 4, oxygen vacancy polaron shape and size were predicted from charge change on Fe around oxygen vacancy site. The shape and size of this polaron were explained from crystal field theory with the d-orbital splitting in Fe due to different Fe-O polyhedral coordination. This predicted polaron shape and size explained the reason behind oxygen vacancy interaction in different LSF compositions and lattice structures.

Chapter 5 determined the oxygen vacancy formation site and how formation energy changes as a function of oxygen non-stoichiometry in different LSF phases. The relationship between the oxygen vacancy formation site and the charge state on Fe was discussed. The critical vacancy concentration, beyond which oxygen vacancy formation energy increases with concentration, is correlated with the vacancy polaron size. When oxygen vacancy formation energy increases with its concentration, the vacancies are considered to be interacting. The interacting vacancies can lead to phase change, which was also discussed in this chapter.

In Chapter 6, both oxygen vacancy site fraction X and non-stoichiometry δ were predicted (in air) for different LSF compositions as a function of temperature and phase change. This calculation utilized the newly developed thermodynamic method for non-dilute (interacting) vacancies. The agreement of the calculated and experimental values of δ over a broad temperature range validates our model. Vacancy ordering induced phase change in LSF causes dropping X with increasing δ , but it is experimentally difficult to separate X and δ . Therefore X was computed, since it contributes to the mobile oxygen vacancy concentration in LSF.

In Chapter 7, oxygen vacancy migration barrier was calculated in different LSF compositions and phases. The oxygen vacancy migration pathway and how the migration influences the oxidation state on oxygen vacancy neighboring Fe were analyzed. Calculated oxygen vacancy concentration along with ionic mobility provided oxygen ion conductivity as a function of temperature and phase change in LSF compositions. These calculations suggested the LSF composition and phase with highest ionic conductivity at SOFC operating conditions.

In Chapter 8, anisotropic chemical expansion in cubic ceria was explained with complete chemical strain tensor along with detailed local lattice distortion. These findings explained the reason behind anomalous strain effect observed in doped ceria (on application of electric field) and directional strain produced in the lattice due to the oxygen vacancy.

Finally, based on the knowledge gained and computational methods developed in this thesis, a future research direction was proposed in Chapter 9, to find new SOFC cathode and to understand the chemical strain effect in SOFC electrolyte like Gd/Pr/Sm doped ceria.

1.1 Factors Influencing Oxygen Vacancy Formation in Perovskite

Multiple factors like the charge distribution on the multivalent Fe cations, interactions between the oxygen vacancies, and oxygen nonstoichiometry (δ) influence the oxygen vacancy formation in perovskite is known for past few decades.^{43,44} Whereas, the mechanistic details explaining the complicated interplay between these factors has yet to be fully established.^{5,6,30,45–47} In order to promote mobile oxygen vacancy concentrations in strontium ferrite and other perovskite type materials,^{28,29,48–51} it is critical to know the location of the oxygen vacancy formation site and the corresponding formation energy and concentration, which is in turn related to the non-uniformly

distributed charge states on the transition metals. Unfortunately, several difficulties encountered by past literature studies have prevented these relationships from being clearly established.^{32–36}

First, it has been experimentally difficult to definitively identify the oxygen vacancy formation sites within the lanthanum strontium ferrite lattice. As shown schematically in Figure 1.1 for $\text{SrFeO}_{3-\delta}$ (SFO) phases, X-ray⁴⁴ and neutron³² diffraction studies have shown that with increasing oxygen nonstoichiometry, the octahedral Fe-O coordination in cubic perovskite SrFeO_3 first transforms into a mixture of square pyramids and octahedra in tetragonal and orthorhombic strontium ferrite, and finally, transform into a mixture of octahedra and tetrahedra in the brownmillerite $\text{SrFeO}_{2.5}$ phase. However, due to the unordered arrangement of the as-formed oxygen vacancies, present experimental techniques have not able to identify their physical distribution within the strontium ferrite crystal structures. Second, despite the fact that various calculations have indicated that the oxygen vacancy formation energy varies with concentration in similar materials,^{28,29,48,49} this effect has not been accounted for in past studies on SFO. For instance, experimental studies have routinely obtained activation energies through linear fits of ionic conductivity versus inverse temperature,³⁸ assuming the activation energy is a constant, which only holds when the vacancies are dilute. Past modeling studies have either utilized dilute defect concentration models,⁵² or ignored the concentration dependence of vacancy formation energy,²⁴ so they cannot predict the vacancy concentration accurately in materials such as SFO^{38,53,54} with interacting point defects. Thus, it is unsurprising that past modeling studies comparing DFT-predicted oxygen vacancy formation energies⁵⁵ with experimentally fitted activation energies measured over large temperature and vacancy concertation spans have shown

large discrepancies.^{24,55,56} Because of this, accurate comparisons of either experimentally derived activation energies or directly measured oxygen nonstoichiometry^{44,57–59} with the results of

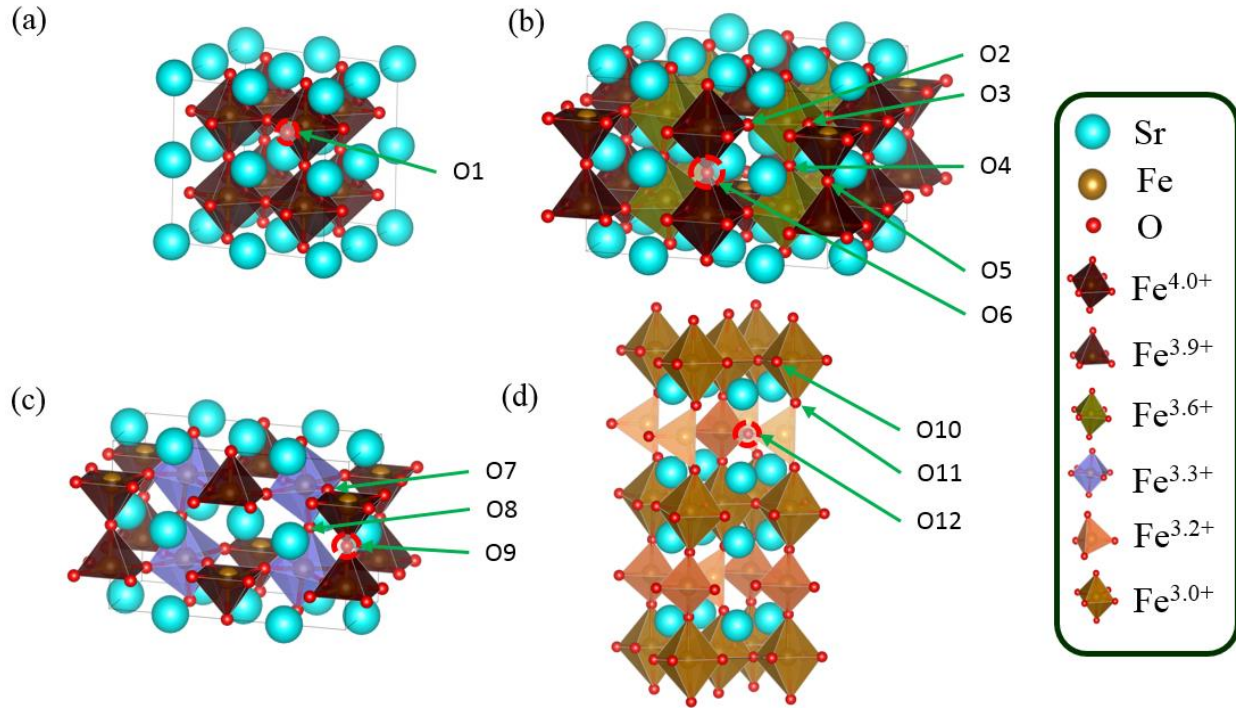


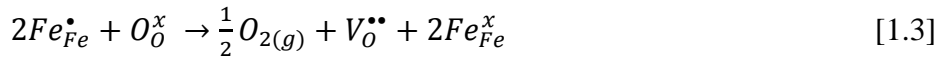
Figure 1.1. Vacancy ordered phases of $\text{SrFeO}_{3-\delta}$: (a) cubic, (b) tetragonal, (c) orthorhombic, and (d) brownmillerite with increasing oxygen non-stoichiometry. The energetically favorable sites for vacancy creation are highlighted with dashed red circles. Fe-O polyhedra are colored according to the calculated charge state on Fe, as shown in the legend, with Fe-O octahedra and square pyramids containing $\text{Fe}^{+3.9}$ or Fe^{+4} dark brown, Fe-O octahedra containing $\text{Fe}^{+3.6}$ yellowish-green; $\text{Fe}^{+3.3}$ light purple; Fe^{+3} light brown, and Fe-O tetrahedra containing $\text{Fe}^{+3.2}$ light orange.

combined DFT and thermodynamic models^{24,55} has been hard to achieve. Third, both experiments and computations have struggled to establish the $\text{Fe}^{3+}/\text{Fe}^{4+}$ ratios that exist within strontium ferrite as a function of oxygen non-stoichiometry. For instance, while it is known that with increasing oxygen non-stoichiometry the formal charge state on Fe (a.k.a the oxidation state) changes from Fe^{4+} in SrFeO_3 , to a mixture of Fe^{3+} and Fe^{4+} when \square is between 0 and ~ 0.5 ,⁵⁷ and finally to Fe^{3+} in $\text{SrFeO}_{2.5}$,³² it is still being debated if $(\text{Fe}^{4+})^{32,35}$ or $(\text{Fe}^{3+})^{33,34,36,60}$ sits in the square pyramidal site found in tetragonal and orthorhombic $\text{SrFeO}_{3-\delta}$.

It is well known that the low oxygen content of many “Sr-poor” LSF concentrations (such as the LSF end member LaFeO_{3-δ} (LFO) which has a large oxygen vacancy formation energy, ΔE_{vac}^f , of ~ 4 eV at 0 K)^{24,61} can be increased through the extrinsic aliovalent Sr substitution of La via the reaction (in Kröger-Vink notation):



However, under most conditions, the extrinsic aliovalent Sr dopant level, x in La_{1-x}Sr_xFeO_{3-δ}, does not independently determine δ because the mixed charge of Fe in La_{1-x}Sr_xFeO_{3-δ} (which varies from 3+ in LaFeO₃ to 4+ in SrFeO₃) can cause δ to vary from $0 \sim x/2$.^{61,62} In LSF, this internal redox reaction can be written as:⁶¹



In addition, the overall oxygen non-stoichiometry, δ , is not always proportional to the mobile oxygen vacancy site fraction, X . For instance, the LSF end member SFO has a very low $\Delta E_{vac}^f \approx 0.4$ eV and hence at room temperature it possess a δ of 0.03, but the X is so low that it seldom used for SOFC applications.^{20, 21} This is because as δ increases, the average distance between the oxygen vacancies shrinks, and beyond a critical δ (or below a critical vacancy-to-vacancy distance) oxygen vacancy interactions lead to an increase in the oxygen vacancy formation energy,^{28,29} and eventually, as in SFO, oxygen-vacancy interactions induce phase transformations that decrease X by rearranging oxygen vacancies into a non-mobile, orderly array.²⁰ This partitioning of δ between X and the number of non-mobile oxygen vacancies per formula unit structurally required to form the particular crystal structure, δ^0 , is summarized by the equation:

$$\delta = \delta^0 + (3 - \delta^0)X \quad [1.4]$$

While many past studies have justified the LSF conductivity maximum occurring at intermediate LSF compositions as a compromise between doping and oxygen vacancy ordering,⁶³ a detailed

understanding of the mechanistic reasons why some intermediate compositions and/or phases are better than others has yet to emerge.

Unfortunately, past attempts to understand the relationship between the Fe charge state distribution, the La:Sr ratio, and the oxygen vacancy interactions in LSF have been limited. For instance, Ritzmann *et al.*,²⁴ calculated that the oxygen vacancy formation energy, ΔE_{vac}^f , increased in $\text{La}_{0.75}\text{Sr}_{0.25}\text{FeO}_{3-\delta}$, decreased in $\text{La}_{0.5}\text{Sr}_{0.5}\text{FeO}_{3-\delta}$, and remained a constant in LFO, when δ increased from 1/32 to 1/8. However, their interesting δ -dependent oxygen vacancy formation energies did not contain an analysis of the oxygen vacancy interactions or the Fe oxidation states in LSF. Further, Mastrikov *et al.*,⁵⁵ showed that ΔE_{vac}^f increased with higher La:Sr ratio in LSF (from SFO to $\text{La}_{0.5}\text{Sr}_{0.5}\text{FeO}_{3-\delta}$ (LSF55) to LFO) at a fixed $\delta = 1/8$. This increase of ΔE_{vac}^f with increasing La:Sr ratio was qualitatively related to the oxidation state on Fe but the reasons for the measured δ peak around a La:Sr ratio of 0.6:0.4 were not discussed. Furthermore, even though the experimental results of Dann *et al.*,⁶⁴ Patrakeev *et al.*,⁶² and Fossdal *et al.*,⁶⁵ have confirmed that the $\text{La}_{1-x}\text{Sr}_x\text{FeO}_{3-\delta}$ crystal structure evolves from orthorhombic ($0 \leq x \leq 0.2$) to rhombohedral ($0.4 \leq x \leq 0.7$) to cubic ($0.8 \leq x \leq 1.0$) at room temperature, and Fossdal *et al.*⁶⁵ observed a rhombohedral to cubic second-order phase transition when rhombohedral LSF55 was heated from room temperature to 523 ± 50 K (in air), these phase changes were not well captured in previous DFT-based oxygen vacancy calculations. For example, Ritzmann *et al.*²⁴ and Mastrikov *et al.*⁵⁵ used a cubic supercell for all LSF structures where x ranged from 1/32 to 1/8, even though experiments have shown that LSF is not cubic at those La:Sr ratios. Recently, Taylor *et al.* used an orthorhombic supercell for LFO but unfortunately did not explore other La:Sr ratios.⁶⁶

Therefore, the aim of the present study was to correctly establish the underlying mechanistic relationships between the La:Sr ratio, the Fe charge state, the oxygen vacancy polaron

size and shape (discussed in Section 1.2), δ and X . Here, three different LSF compositions, $\text{LaFeO}_3-\delta$ (LFO), $\text{La}_{0.5}\text{Sr}_{0.5}\text{FeO}_3$ (LSF55) and $\text{SrFeO}_{3-\delta}$ (SFO) were studied. SFO and LFO represent the parent phases⁶⁵ of LSF and LSF55 was selected for its high oxygen ionic conductivity^{62,63} and as a representative structure of the commonly used SOFC cathode material LSF64 ($\text{La}_{0.6}\text{Sr}_{0.4}\text{FeO}_{3-\delta}$).^{6,61} The study objectives were achieved using a combined thermodynamics and DFT+ U approach performed by first, appropriately selecting a suitable U parameter (as described in Sections 2.1.1), second, using a magnetic moment interpreted charge calculation, instead of the traditional and in this case insensitive Bader charge analysis, to determine the Fe charge state (as described in Section 2.1.2), third, validating the DFT simulations with known experimentally determined physical properties (as described in Chapter 3), fourth, calculating the effect of oxygen vacancy interactions on ΔE_{vac}^f (as described in Chapter 4), and fifth, using a newly-developed thermodynamic model²⁷ to predict X for various LSF compositions and phases under SOFC operating conditions (described in Chapter 6).

1.2 Oxygen Vacancy Interaction via Vacancy Polaron

MIEC oxygen vacancy ordering is often discussed in terms of oxygen vacancy polarons, which Landau⁶⁷ defined as the excess charge (generated during the formation of a charge neutral oxygen vacancy) and the surrounding lattice strain field. Since the excess electrons generated during oxygen vacancy formation both screen the charge on their associated oxygen vacancy site and induce lattice distortions, they impact the formation of subsequent oxygen vacancies at high δ . While it is hard to exactly define polaron size and shape because the partial excess charges are distributed to both the Fe and O atoms around a missing lattice oxygen,^{68,69} for simplicity, one can estimate the polaron size and shape based on the spatial deviations in transition metal charge states

alone. For example, Castleton *et al.*,⁶⁹ defined the oxygen vacancy polaron in ceria as the localized electrons on two Ce atoms adjacent to an oxygen vacancy site.⁷⁰ In a recent study Das *et al.*,²⁷ also took this approach and found that the strong oxygen vacancy interactions in LSF end member, SFO was due to a very large oxygen vacancy polaron size. Specifically, it was found that electron occupancy and crystal-field-splitting-induced differences between the 3d electron orbitals of the square pyramidal coordinated, oxygen-vacancy-adjacent Fe atoms and the octahedrally-coordinated, oxygen-vacancy-second-nearest-neighboring Fe atoms caused the two electrons left behind during oxygen vacancy formation in cubic SFO to spread to the second nearest neighbor Fe (instead of the Fe directly connected to the vacancy) resulting in extended lattice distortions that promoted strong oxygen vacancy interactions.²⁷ However, the distribution of the excess electrons generated by oxygen vacancy formation in $\text{La}_{1-x}\text{Sr}_x\text{FeO}_{3-\delta}$ has not been examined. Further, a detailed understanding of the relationship between the Fe charge state distribution associated with polaron and oxygen vacancy interactions in LSF has been missing from the literature. This is partially due to the difficulty in determining the actual Fe charge distribution within LSF, for both experimentalists and theorists.^{24,43,61,62,71} For instance, while it is recognized that $\text{La}_{1-x}\text{Sr}_x\text{FeO}_{3-\delta}$ has a mixture of both Fe^{3+} and Fe^{4+} ions, it is still debated where Fe^{3+} or Fe^{4+} sits in vacancy-containing lattices.

This new “long-range charge transfer” mechanism results in large oxygen vacancy polaron sizes that cause strong oxygen vacancy interactions and an increase in the oxygen vacancy formation energy with increasing oxygen vacancy site fraction. The objective of the present work was to examine the impact of lanthanum doping on this SFO oxygen vacancy formation behavior and the oxygen vacancy migration behavior of a variety of LSF compositions and crystal structures.

Further, use this charge transfer concept to predict oxygen vacancy interactions in Mn or Co-containing perovskites, $\text{La}_{1-x}\text{Sr}_x\text{MnO}_{3-\delta}$ or $\text{La}_{1-x}\text{Sr}_x\text{CoO}_{3-\delta}$.

1.3. Effect of the oxygen vacancy interaction on Ionic conductivity at SOFC operating conditions

Performance of the MIEC materials is mostly limited due to an exponential loss in oxygen ionic conductivity at a lower temperature.⁷² To achieve the ultimate goal of designing MIEC materials with high ionic conductivity operating at a relatively lower temperature, we have to understand the factors (mentioned earlier) controlling the ionic conductivity in it. The specific aim of this study is to predict the oxygen ionic conductivity of the SOFC material from computationally predicted oxygen vacancy concentration and diffusivity. The ionic conductivity, σ can be predicted with Equation 1.1. Where, c is nothing but δ/V_u , (V_u : volume per formula unit) if there is no vacancy ordering in the lattice. In case of oxygen vacancy ordering, c should be related to X with below equation:

$$c = (3 - \delta^0)X/V_u \quad [1.5]$$

The above equation holds for both vacancies ordered and unordered lattices. For lattice without vacancy ordering, $\delta^0 = 0$. Therefore, in that case $\delta = 3X$, which satisfies previous relation.

Further, it is required to develop a thermodynamic model which can predict oxygen vacancy site fraction as a function of temperature, pressure, and oxygen vacancy concentration and then use that data to predict ionic conductivity. The model should be robust enough that it will efficiently predict the oxygen site fraction for both interacting and non-interacting vacancies. The thermodynamic model prior to this work used to predict vacancy site fraction is shown in Equation

1.6.⁵² Where, ΔG_{vac}^f is the vacancy formation free energy at the SOFC operating temperature (T) and partial pressure of oxygen (p). k_B denotes Boltzmann constant.

$$\frac{x}{1-x} = \exp\left(-\frac{\Delta G_{vac}^f(T,p)}{k_B T}\right) \quad [1.6]$$

Hence, it is required to develop a thermodynamic model as shown in Section 2.5, which can predict oxygen vacancy site fraction as a function of temperature, pressure and concentration dependent formation free energy.

Einstein relation can relate the mobility of an ion to diffusivity (D), is given as,

$$\mu = \frac{Z e D}{k_B T} \quad [1.7]$$

Furthermore, the diffusivity can be calculated as:

$$D = D_0 \exp\left(-\frac{E_a}{k_B T}\right) \quad [1.8]$$

Where, D_0 is the pre-factor of diffusion. E_a is the activation energy for diffusion can be obtained from vacancy formation free energy, ΔG_{vac}^f and migration energy, ΔH_{mig} . ΔH_{mig} can be calculated via nudged elastic band method (NEB). If this method is established to predict ionic conductivity at SOFC operating conditions, then we can directly compare the DFT predicted results with experimental measurements. Hence, this prediction will elucidate a method to directly predict ionic conductivity for interacting vacancies of newly designed materials without any experimental inputs.

1.4. Anisotropic Chemical Strain Effect Due to Oxygen Vacancy Polaron

Pure and doped Ceria are amongst the most studied nonstoichiometric oxides, due to its application as a commercial catalyst.^{73,74} The catalytic capability of ceria owes to the reversible transition between Ce⁴⁺ and Ce³⁺. The nonstoichiometric Gd-doped ceria (GDC) though mainly used for catalytic application but the reversible transition of Ce⁴⁺ and Ce³⁺ enables its' application for electrostriction.⁷⁵ The application of electric field on a nonstoichiometric GDC thin film orients the local chemical strain fields (with polaron) producing observable mechanical stress, is a good example of the electro-chemo-mechanical coupling concept.⁷⁶ The change of chemical strain field on the application of electricity implies the anisotropic nature of chemical strain in ceria, which is the prime focus of this study.

Previous experimental and computational studies were devoted to measure/calculate the average chemical strain effect in pure or doped ceria. For example, using molecular dynamics simulation Marrocchelli *et al.*⁴⁰ predicted average chemical expansion coefficient, α_C , by creating different amount of vacancies (δ) and predicting average strain (ε_C) at those δ . Then from the slope of ε_C with δ , $\alpha_C (= \varepsilon_C / \delta)$ was calculated. Further, using DFT Shenoy *et al.*⁴¹ calculated isotropic ε_C , assuming isotropic chemical strain field in ceria, due to its cubic symmetry. Shenoy *et al.* used only principle components of the elastic dipole tensor to calculate average chemical strain, neglecting anisotropic effect. Whereas, the orientation of chemical strain dipole on application of electric field suggests that, due to non-uniform bond distortion around oxygen vacancy site, the oxygen vacancy induced chemical strain is anisotropic in nature, which helped to orient the strain field on application of electricity.

The objective is to understand how the oxygen vacancy polaron causes asymmetric lattice distortion locally in cubic ceria, thus anisotropic chemical strain is produced in nonstoichiometric

ceria. To understand the oxygen vacancy induced anisotropic chemical strain due to non-uniform bond distortion around oxygen vacancy site, a complete strain tensor, $\boldsymbol{\varepsilon}_C$ should be used. The complete strain tensor can be calculated from elastic dipole tensor, \mathbf{G} and elastic stiffness tensor, \mathbb{C} as:⁴²

$$\boldsymbol{\varepsilon}_C = \frac{-\delta(\mathbb{C}^{-1}\mathbf{G})}{V_U} \quad [1.9]$$

Where δ is oxygen nonstoichiometry, and V_U is the volume per formula unit. The detailed derivation of the above equation is provided in Section 2.6. With this method, the reason behind anisotropic chemical strain tensor was quantified and its tensorial relationship with the crystallographic orientation of the lattice will explain the giant strain effect in GDC under electrical bias.⁴²

2. Computational Details: Methodology developed and Used

The plane wave based *ab initio* simulation package, VASP (Vienna *Ab initio* Simulation Package)⁷⁷ was used for all the ground state (0 K, zero pressure) calculations. Projector-augmented-wave (PAW)^{78,79} potentials with valence configurations of $5s^25p^65d^16s^2$ for La, $4s^24p^65s^2$ for Sr, $3d^74s^1$ for Fe, and $2s^22p^4$ for O were used to describe the valence electrons. The generalized gradient approximation (GGA) functional along with Perdew, Burke, and Ernzerhof (PBE)^{80,81} parameters were used to describe the exchange-correlation potentials of the constituting elements. As GGA predicted results suffer from self-interaction error in strongly correlated transition metal complexes,⁸² Fe was treated with the GGA+U method⁸³ with a $U_{\text{eff}} = 3$. A detailed discussion of the Fe atom U parameter selection process is provided in Sections 2.1.1. Spin-polarized calculations were performed and the magnetic moment on each Fe was calculated by spherical integration.⁸⁴ The accuracy of the electronic calculations was within 1 μeV . A single point energy calculation was performed to test the convergence of the cut-off energy and k -points for each input lattice. It was concluded from the k -mesh calculations that a k -spacing of 0.2 \AA^{-1} was sufficient for the required accuracy of 1 meV/atom when the cutoff energy was set to 500 eV. Ionic relaxations were performed until the Hellmann-Feynman force on each atom reached the order of 10 meV/ \AA .⁸⁵

First, the calculation methods were tested for their ability to accurately predict the experimentally observed LSF crystal structures, lattice parameters, and low-temperature Fe magnetic ordering arrangements. According to experiments, the representative LFO, SFO, and LSF55 compositions exhibit orthorhombic, cubic, and rhombohedral structures, respectively, at room temperature.^{44,46,86} In addition to the different crystalline structures shown in Figure 1, they can also exhibit magnetic ordering, as indicated by Mössbauer results showing G-type Fe

antiferromagnetic (AFMG) ordering for $0 < x < 0.3$ and paramagnetic Fe ordering for $x > 0.4$, at room temperature.⁸⁷

The ground state energy for all three oxygen-stoichiometric (i.e., $\delta = 0$) LSF compositions was calculated with six different initial structures (three ground state crystal structures, as shown in Figure 2.1, multiplied with two magnetic ordering arrangements), by allowing the cell shape and atom positions to relax. Among these six input structures, the one with the minimum energy per formula unit was considered as the (ground state) crystal structure for that composition. The calculated crystal structures, lattice parameters, bond lengths, low-temperature magnetic ordering arrangements, and band gaps for stoichiometric SFO, LSF55, and LFO were benchmarked with experimental or computational studies whenever available in the literature.

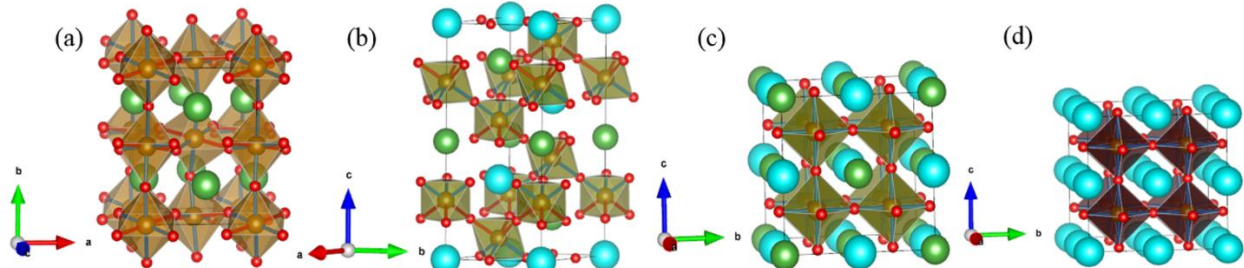


Figure 2.1. DFT calculated lattice structures for (a) orthorhombic LaFeO_3 , (b) rhombohedral $\text{La}_{0.5}\text{Sr}_{0.5}\text{FeO}_3$, (c) cubic $\text{La}_{0.5}\text{Sr}_{0.5}\text{FeO}_3$ (high temperature phase), and (d) cubic SrFeO_3 . Atoms are colored as La – green, Sr - blue, Fe – brown, O – red. The different Fe-O₆ octahedra colors denote polyhedra with different Fe charge states: Fe^{3+} – light brown, $\text{Fe}^{3.5+}$ – moss green, Fe^{4+} – dark brown.

2.1. Magnetic Moment Interpreted Oxidation State Prediction

Though Bader charge analysis is a widely used and efficient method to define formal charge on atoms,^{88,89} it is not universally applicable for all compounds.^{48,53} For example, Bader charge analysis on Fe in LaFeO_3 , $\text{La}_{0.75}\text{Sr}_{0.25}\text{FeO}_{3-\delta}$ and $\text{La}_{0.5}\text{Sr}_{0.5}\text{FeO}_3$ show a charge of 1.70 e , not able to determine the charge change on Fe due to change in La/Sr-ratio. Further, after oxygen vacancy

formation the charge on vacancy adjacent Fe was not significantly different for changing La/Sr-ratios.²⁴ Therefore, a new way to define charge on Fe was required. As a result, we propose a magnetic moment interpreted charge for a magnetic element, like Fe. As magnetic moment is directly related to a number of unpaired electrons, so from magnetic moment on Fe formal charge can be predicted and can be compared with experimental measurement. Only DFT study was not able to predict the magnetic moment on Fe correctly (refer to $U = 0$ in Figure 2.2(a)), and Hubbard- U was necessary for proper treatment of the localized $3d$ -electrons of Fe.

2.1.1. Selection of U Parameter

DFT with a Hubbard- U approach (DFT+U)⁹⁰ was used to address the on-site electronic interactions of the $3d$ -orbitals in the multivalent Fe atoms. This method has been shown to accurately predict the enthalpy of formation of oxides, the open circuit voltage in Li-ion batteries, phase diagrams, chemical reaction barriers, etc. for many transition-metal-containing compounds.^{30,91-93} In the DFT+U framework, spherically averaged Coulombic and exchange interactions for the electrons, denoted by U and J respectively, enter into DFT calculations as overhead terms.⁹⁴ Following the approach of Dudarev *et al.*,⁹⁰ these U and J parameters can be combined as $U_{\text{eff}} = U - J$, or used simply as a U parameter. The Hubbard- U parameter can be selected either directly employing *ab initio* methods like constrained-DFT^{94,95} or based on empirically fitting experimental properties such as the band gap, magnetic moment, lattice parameters, bulk modulus, etc.^{3,90,92,96,97} In some DFT+U studies, different transition metal charge states were treated with different U parameters. For example, Mosey *et al.*,⁹⁵ treated Fe^{2+} and Fe^{3+} with $U_{\text{eff}} = 3.7$ and 4.3 respectively, giving reasonable lattice parameter, magnetic moment, band gap and other physical property agreement for Fe_2O_3 and FeO . However, the energies calculated with different U parameters should not be

compared (since the electrons are more localized with increasing U), making it impossible to use that approach to perform comparative studies of different LSF phases containing mixed Fe oxidation states.

In the present study, because the local formal charge state on Fe was allowed to vary from $2+ \sim 4+$ (due to the changing La/Sr ratio and the changing oxygen vacancy content), a single U parameter was required to treat all the multi-valent Fe atoms. GGA+U calculations were performed for (orthorhombic, FM) LFO and (cubic, FM) SFO with the U parameter over a range of 0.2 to 4.0 eV. The U-parameter was selected based on a careful comparison with the experimentally observed magnetic moments (as shown in Figure 2.2(a)) and lattice parameters (as shown in Figure 2.2(b)) of the LSF end members. The reason behind the selection of U to match both LFO and SFO was that the charge on Fe in LSF varies between 3+ and 4+, and the charge on Fe in LSF can be further interpreted as a linear mixing of 3+ and 4+ (as shown in Figure 2.3).⁹⁸

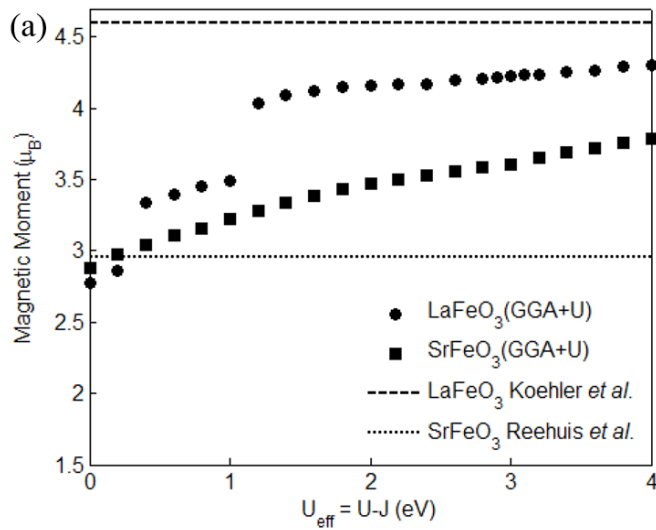


Figure 2.2. The plot of (a) magnetic moment and (b) lattice parameters as a function of U_{eff} parameter. The straight lines are experimental data, and blue and red correspond to the data for SrFeO_3 and LaFeO_3 , respectively. Since LaFeO_3 is not cubic, red, green and pink colors in (b) are corresponding to scaled-lattice ($a/\sqrt{2}$, $b/2$, $c/\sqrt{2}$ respectively) of LaFeO_3 .

Figure 2.2 (cont'd)

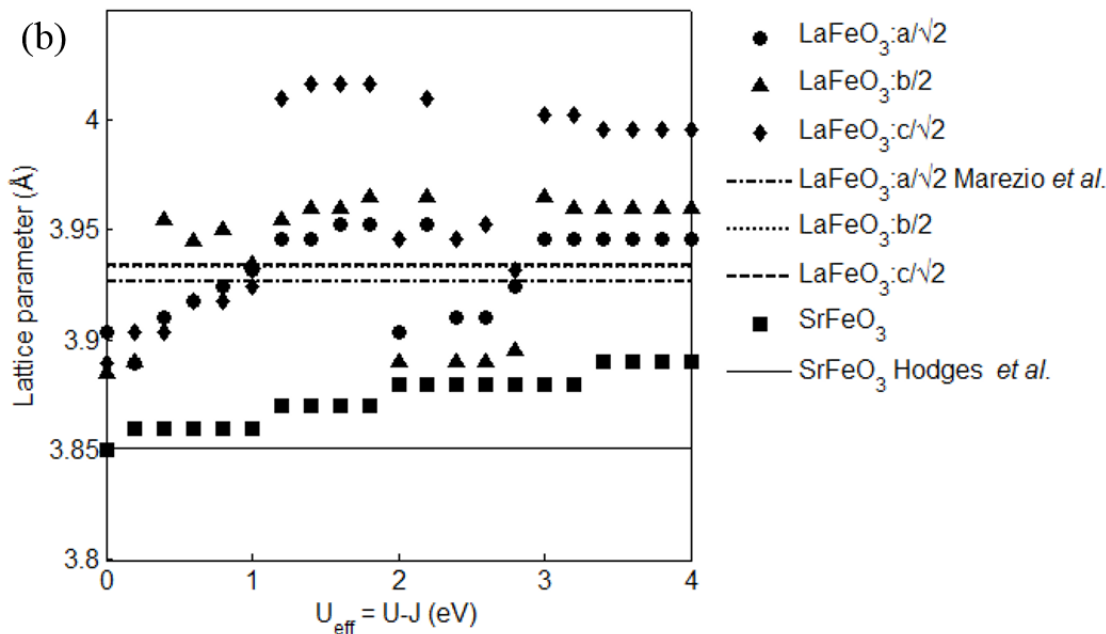


Figure 2.2(a) shows a comparison between the experimental and computed Fe magnetic moments with varying U-parameter (from 0.2 to 4) for LFO and SFO, represented by lines and solid dots, respectively. SFO showed a steady increase in the magnetic moment of Fe with increasing U parameter but the magnetic moment of Fe in LFO fluctuated (Figure 2.2(a)), possibly due to the existence of additional minima as a result of different possible electronic distributions.⁹⁹ The experimental magnetic moment for Fe in LFO was reported by Koehler *et al.*¹⁰⁰ as $\mu_{Fe^{3+}} = 4.6 \pm 0.2 \mu_B$ (Figure 2.2(a), dashed line) and it is a widely acceptable value in the literature.^{101–103} In contrast, difficulty in the experimental sample preparation of stoichiometric cubic SFO^{104,105} has resulted in a large variability in the experimentally measured Fe magnetic moments in SFO.^{32,105,106} Nevertheless, most of the experimental data indicates that Fe has a high spin state in SFO.^{104,107–109} In a recent comprehensive study, Reehuis *et al.*¹⁰⁵ measured the magnetic moment on Fe in stoichiometric cubic SFO as $\mu_{Fe^{4+}} = 2.96 \mu_B$ (Figure 2.2(a), dotted line) with neutron diffraction, at 2 K.

Figure 2.2(b) compares the computed lattice parameters of LFO and SFO with experimental results. Note, to allow a comparison of the computed and experimental lattice parameters in a single plot, all the LFO lattice parameters were divided by $\sqrt{2}$ before plotting in Figure 2.2(b). As done previously for SFO,²⁷ based on a comparison of the computed versus experimental lattice parameters and magnetic moments for both LFO and SFO in Figure 2.2, a $U_{\text{eff}} = 3$ was selected. With this value of U , the lattice parameters showed a maximum deviation of 1.75 % from their experimentally-measured room temperature values. The selection of $U_{\text{eff}} = 3$ also resulted in a reasonable agreement between the computed and experimentally measured magnetic moments. The computed magnetic moment was $\mu_{Fe^{3+}} = 4.23 \mu_B$ for Fe^{3+} in LFO, and was $\mu_{Fe^{4+}} = 3.61 \mu_B$ for the Fe^{4+} present in SFO, both of which were similar to the experimental values.^{100,101,105} In some earlier computational studies with multivalent Fe atoms, the focus was on Fe^{3+} containing compounds, for which a $U_{\text{eff}} = 4$ ¹¹⁰ or 5.4 ¹¹¹ was employed. However, only a few studies exist where Fe multi-valence states were treated with a single U parameter. For example, Muñoz-García *et al.*,⁴⁹ treated 2+, 3+, and 4+ charge states on Fe with $U_{\text{eff}} = 4$ and Ritzmann *et al.*,²⁴ used $U_{\text{eff}} = 5.4$, where the Fe charge state varied from 3+ to 3.5+. One consequence of using such a high U -parameter is that the vacancy formation energy might be underestimated.²⁷ For example, it was reported in our previous study that $U_{\text{eff}} = 4$ would lead to a lower oxygen vacancy formation energy in SFO, resulting in a $\sim 200^\circ\text{C}$ difference in the temperature required to generate the oxygen non-stoichiometry observed in cubic $SrFeO_{3-\delta}$ in the air.²⁷ Thus, when Ritzmann *et al.*,²⁴ used $U_{\text{eff}} = 5.4$ in their calculations, the underestimated vacancy formation energy led to an unphysical (negative) oxygen vacancy formation free energy at 700°C for LSF55. As will be shown in Chapter 3, a $U_{\text{eff}} = 3$ also gave the correct band gap and phases for various SFO compositions and phases.

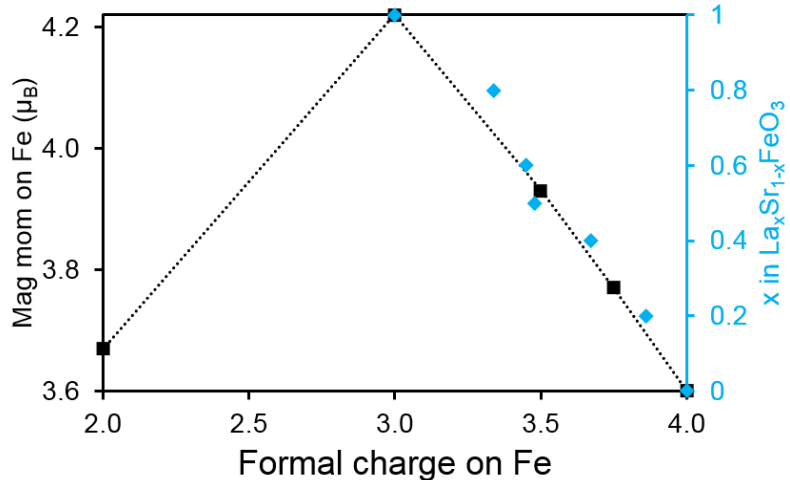


Figure 2.3. Black squares represent the formal charge on Fe resulting from different La/Sr ratios in $\text{La}_x\text{Sr}_{1-x}\text{FeO}_3$ calculated from the magnetic moment on Fe with a GGA+U(=3) (left y-axis). Blue diamonds show experimentally measured average Fe charge states for varying La/Sr ratios (right y-axis). The black dotted line represents the predicted linear relationship between the Fe charge state and the La/Sr ratio.

2.1.2. Determining Oxidation State on Fe

DFT with a Hubbard- U approach (DFT+U)⁹⁰ was used to address the on-site electronic interactions of the 3d-orbitals in the multivalent Fe atoms. This method has been shown to accurately predict the enthalpy of formation of oxides, the open circuit voltage in Li-ion batteries, phase diagrams, chemical reaction barriers, etc. for many transition-metal-containing materials.^{30,91–93} In the DFT+U framework, spherically averaged Coulombic and exchange interactions for the electrons, denoted by U and J respectively, enter into DFT calculations as overhead terms.⁹⁴ Following the approach of Dudarev *et al.*,⁹⁰ these U and J parameters can be combined as $U_{\text{eff}} = U - J$, or used simply as a U parameter. The Hubbard- U parameter can be selected either directly employing *ab initio* methods like constrained-DFT^{94,95} or based on empirically fitting experimental properties such as the band gap, magnetic moment, lattice parameters, bulk modulus, etc.^{3,90,92,96,97} In some DFT+U studies, different transition metal charge states were treated with different U parameters.

For example, Mosey *et al.*,⁹⁵ treated Fe^{2+} and Fe^{3+} with $U_{\text{eff}} = 3.7$ and 4.3 respectively, giving reasonable lattice parameter, magnetic moment, band gap and other physical property agreement for Fe_2O_3 and FeO . However, the energies calculated with different U parameters should not be compared (since the electrons are more localized with increasing U), making it impossible to use that approach to perform comparative studies of different LSF phases containing mixed Fe oxidation states.

In the present study, because the local formal charge state on Fe was allowed to vary from $2+ \sim 4+$ (due to the changing La/Sr ratio and the changing oxygen vacancy content), a single U parameter was required to treat all the multi-valent Fe atoms. GGA+ U calculations were performed for (orthorhombic, FM) LFO and (cubic, FM) SFO with the U parameter over a range of 0.2 to 4.0 eV. The U -parameter was selected based on a careful comparison with the experimentally observed magnetic moments (as shown in Figure 2.2(a)) and lattice parameters (as shown in Figure 2.2(b)) of the LSF end members. The reason behind the selection of U to match both LFO and SFO was that the charge on Fe in LSF varies between $3+$ and $4+$, and the charge on Fe in LSF can be further interpreted as a linear mixing of $3+$ and $4+$ (as shown in Figure 2.3).⁹⁸

2.1.3. Advantage over Bader Charge

The calculated total Bader charge analysis, as shown in Table 2.1, indicates charge on Fe in LFO, LSF55 and SFO were $2.00+$, $2.03+$ and $2.04+$ respectively, whereas the expected formal charge on Fe in these structures are $3.0+$, $3.5+$, and $4.0+$ respectively. This signifies that the calculated total Bader charge on Fe was insensitive to the local electronic environment in LSF, and therefore could not be used to determine the formal charge on Fe. Fortunately, the total unpaired electrons obtained via spin polarized Bader charge analysis of Fe show a significant variation from 3.88 to

4.64 e from SFO to LFO. Hence, the magnetic moment, which is a manifestation of the unpaired electrons in an element, was used to interpret the charge state on Fe. Accordingly, the magnetic moment calculated by VASP was used to interpret the formal charge state on Fe. Note, neither the spherical integration of charge used in a VASP calculation nor the Voronoi integration used in the Bader method gave the exact formal charge on Fe in LSF. Therefore, a magnetic moment of 4.23 μ_B for Fe was assigned to represent Fe^{3+} and 3.61 μ_B for Fe^{4+} in agreement with the LSF end member Fe charge states and magnetic moment discussed in Section 2.1.

Table 2.1. Spin-polarized Bader charge analysis of different LSF phases. Magnetic moment calculated by VASP and expected formal charge on Fe are also provided for comparison.

Phase	Bader Analysis						Expected formal charge	VASP magnetic moment (μ_B)	Magnetic moment interpreted charge
	Element	Up e	Down e	Total e	Unpaired e	Bader charge (q)			
LaFeO_3 (orthorhombic)	La	4.46	4.46	8.92	0.00	2.08+	3.0+	--	--
	Fe	5.32	0.68	6.00	4.64	2.00+	3.0+	4.23	3.0+
	O	3.74	3.62	7.36	0.12	1.36-	2.0-	--	--
$\text{La}_{0.5}\text{Sr}_{0.5}\text{FeO}_3$ (rhombohedral)	La	4.44	4.43	8.87	0.01	2.13+	3.0+	--	--
	Sr	4.21	4.21	8.42	0.00	1.58+	2.0+	--	--
	Fe	5.16	0.81	5.97	4.34	2.03+	3.5+	3.94	3.5+
	O	3.68	3.63	7.31	0.05	1.30-	2.0-	--	--
SrFeO_3 (cubic)	Sr	4.20	4.19	8.39	0.01	1.60+	2.0+	--	--
	Fe	4.92	1.04	5.96	3.88	2.04+	4.0+	3.61	4.0+
	O	3.63	3.59	7.22	0.04	1.21-	2.0-	--	--
SrFeO_2 (Planar)	Sr	4.22	4.23	8.45	0.01	1.55+	2.0+	--	--
	Fe	5.24	1.39	6.63	3.86	1.37+	2.0+	3.68	2.0+
	O	3.76	3.69	7.45	0.07	1.46-	2.0-	--	--

It is possible that after neutral oxygen vacancy generation, some oxygen-vacancy-neighboring Fe^{3+} atoms will adopt a charge closer to Fe^{2+} . Although Fe^{2+} was not considered in the U-parameter selection, its charge was calibrated with the magnetic moment of Fe^{2+} in (planar) SrFeO_2 . Since Fe^{2+} has the same number of unpaired electrons as Fe^{4+} , it gives rise to a magnetic moment of 3.68 μ_B which is close to the $\mu_{Fe^{4+}} = 3.61 \mu_B$ (and comparable to experimentally reported SrFeO_2 magnetic moment at 10 K).¹¹²

Figure 2.3 shows the computed magnetic moment and the formal charge on Fe compared to the experimentally measured average charge on Fe in LSF, which also shows a linear relationship. Hence, in the current work, an intermediate magnetic moment was interpreted as a linear interpolation between 3+ and 4+ charge states.⁹⁸ In LSF55, Fe is expected to carry a formal charge of 3.5+ and from the linear relation of charge and magnetic moment, $\text{Fe}^{3.5+}$ corresponds to a magnetic moment of $3.92 \mu_B$, which was very close to the VASP calculated magnetic moment of $3.94 \mu_B$ for $\text{Fe}^{3.5+}$ in rhombohedral LSF55. Overall, the selection of $U_{\text{eff}} = 3$ and the magnetic moment interpreted charge jointly captured the Fe charge state ranging from Fe^{2+} to Fe^{4+} in $\text{La}_x\text{Sr}_{1-x}\text{FeO}_{3-\square}$.

2.2. Determining Polaron Shape and Size from the Valance Change on Transition Metal

In 1933 Lev Landau,⁶⁷ proposed the concept of polaron as a quasiparticle. It was described as an electron moving in a dielectric crystal where the atoms move from their equilibrium positions to effectively screen the charge of an electron. Following the concept we have defined our oxygen vacancy polaron, where two excess electron left due to the oxygen vacancy formation gets distributed to the nearest neighboring Fe atoms, causing charge change and lattice distortion. For accuracy of the calculation if the magnetic moment interpreted charge on a Fe changed by $\pm 0.1e$ after oxygen vacancy formation, then it was considered as the “charge change” on Fe. Further, from charge change on Fe atoms neighboring to oxygen vacancy site, we found the extent of charge transfer and shape and size of the polaron. If the excess electron generated due to a neutral oxygen vacancy formation transferred to second nearest neighboring Fe, then it was named as “long range charge transfer”.

2.3. Calculation Method of Oxygen Vacancy Formation and Migration Barrier Energy

Oxygen vacancy formation and migration energies were calculated using DFT+U method. The 0 K calculated energy with temperature and pressure correction can be converted to experimentally measurable quantity like oxygen vacancy nonstoichiometry, diffusivity etc. The vacancy formation and migration energies were calculated with varying size of supercell for each LSF phases. If the calculated energy didn't change with lattice size then it was considered as dilute vacancy scenario, otherwise interacting vacancy scenario.

2.3.1. Oxygen Vacancy Formation Energy at 0 K

For the defect reaction,¹¹³ $O_O^x \rightleftharpoons V_O^{\bullet\bullet} + 2e' + \frac{1}{2}O_2$, the neutral oxygen vacancy formation energy (ΔE_{vac}^f) per vacancy at 0 K was calculated using the relationship:⁸⁵

$$\Delta E_{vac}^f = E_{defective}^{DFT} - E_{perfect}^{DFT} + \frac{1}{2}E_{O_2}^{DFT} \quad [2.1]$$

where $E_{defective}^{DFT}$ is the energy of a structure with one oxygen vacancy, $E_{perfect}^{DFT}$ is the energy of the perfect crystal structure, and $E_{O_2}^{DFT}$ is the energy of an oxygen molecule¹¹⁴ in its gas phase. $E_{O_2}^{DFT}$ was computed as -9.86 eV for an isolated oxygen molecule placed inside a $20 \times 20 \times 20 \text{ \AA}^3$ simulation cell, with a predicted bond length of 1.23 Å. The predicted energy and bond length are in well agreement with values reported in the literature.^{85,115,116} $E_{defective}^{DFT}$ was calculated in supercells of varying size containing a single oxygen vacancy, mimicking a broad range of oxygen nonstoichiometry. In $\text{SrFeO}_{3-\delta}$, increasing the absolute oxygen non-stoichiometry (δ) causes the oxygen vacancy site fraction (X) to increase until oxygen vacancy ordering induces a phase transformation that reduces the total number of lattice oxygen sites and resets X to zero; a fact which can be summarized with the Equation 1.4. Where δ^0 is the value of δ , when $X = 0$ for each

perfect crystal structure (i.e. δ^0 equals 0, 0.125, 0.25, and 0.5 in cubic SrFeO_3 , tetragonal $\text{SrFeO}_{2.875}$, orthorhombic $\text{SrFeO}_{2.75}$, and brownmillerite $\text{SrFeO}_{2.5}$, respectively). Hence, a single oxygen vacancy created in a supercell with n formula units of cubic strontium ferrite ($\text{Sr}_n\text{Fe}_n\text{O}_{3n}$) corresponded to a $\delta = 1/n$, while a single oxygen vacancy created in a supercell with n formula units of brownmillerite strontium ferrite ($\text{Sr}_n\text{Fe}_n\text{O}_{2.5n}$) corresponded to a $\delta = 0.5 + 1/n$.

It is important to note that as shown in Equation 1.4, the same δ can be achieved by having a large X in a structure with a low δ^0 or by having a small X in a structure with a higher δ^0 . For crystal structures containing multiple oxygen vacancy sites (Figure 1.1(b-d)), the oxygen vacancy formation energy was calculated for all possible sites in order to identify the site with the lowest oxygen vacancy formation energy. The largest supercell used for the cubic SFO, rhombohedral LSF55, cubic LSF55 and orthorhombic LFO calculations was 4x4x4, 3x3x3, 3x3x3, and 2x2x2, which represents an average distances of 15.52 Å, 16.55 Å, 16.58 Å, 12.78 Å between the vacancies for $\delta = 0.02, 0.02, 0.02$, and 0.03 respectively. The present study focuses on the variation of non-stoichiometry at a uniform distribution of the oxygen vacancies. DFT+U minimized lattice parameters were used in vacancy formation calculations, since it is estimated that the thermal expansion will only induce lattice parameter changes less than 3% between 0 and 1000 K.¹⁰⁶ Further, it is important to note that the material undergoes a continuous phase change in the measured temperature range.

2.3.2. Predicting Vacancy Ordered Phase Transition

It is known that DFT+U calculation does a poor job in predicting phase transition in materials, especially when metal to insulator phase transition happens but our selection of U parameter in this study was able to capture the energetically favored phases when oxygen vacancy ordered phase

transitions occurred at a certain oxygen non-stoichiometry. In order to determine energetically favorable arrangements, the excess energy (ΔE^δ) of various oxygen deficient structures (cubic, tetragonal, orthorhombic, and brownmillerite) with respect to the perfect cubic SrFeO₃ was defined and compared via the relation:

$$\Delta E^\delta = E_{SrFeO_{3-\delta}}^{DFT} + \frac{\delta}{2} E_{O_2}^{DFT} - E_{SrFeO_3}^{DFT} \quad [2.2]$$

where $E_{SrFeO_{3-\delta}}^{DFT}$ is the energy of the oxygen deficient arrangement of interest, $E_{O_2}^{DFT}$ is the energy of an isolated oxygen molecule, and $E_{SrFeO_3}^{DFT}$ is the energy of the perfect cubic SrFeO₃.

2.3.3. Calculating Oxygen Vacancy Migration Barrier

The oxygen migration barriers between all the possible oxygen vacancy sites in cubic, tetragonal, and orthorhombic SFO, rhombohedral LSF55, and orthorhombic LFO were calculated and compared at 0 K. Then, the impact of a change in the magnetic moment of the Fe atoms along the oxygen vacancy migration path was determined. The migration energy barrier can be converted to diffusivity using thermodynamic data as shown in Section 2.5.2. The migration energy can be calculated using Climb Image Nudge Elastic Band (CINEB) method¹¹⁷ which will also provide the transition state structure. In the NEB method, one only gets the minimum energy path (MEP).^{118,119} The maximum value of the potential energy along the path will give the activation energy (barrier) for the diffusion process. Using CINEB it not only gives the MEP but also finds the transition state structure at the saddle point.¹²⁰

2.4. Thermodynamic Extension of DFT Calculated Energies

DFT calculations are performed at 0 K and zero pressure. Therefore, to compare DFT calculated properties with experimentally observed results a thermodynamic extension to the DFT calculated properties is necessary.

2.4.1. Converting Vacancy Formation Energy to Vacancy Formation Free Energy

To facilitate comparisons between computational predictions and experimentally measurable properties (such as the oxygen vacancy concentration at finite temperatures), DFT computed oxygen vacancy formation energies were converted into temperature (T) and oxygen partial pressure (p_{O_2}) dependent oxygen vacancy formation free energies (ΔG_{vac}^f) via the relation:

$$\Delta G_{vac}^f(T, p_{O_2}) = E_{defective}(T, p_{O_2}) - E_{perfect}(T, p_{O_2}) + \frac{1}{2}\mu_{O_2}(T, p_{O_2}) \quad [2.3a]$$

where $E_{defective}(T, p_{O_2})$, $E_{perfect}(T, p_{O_2})$ and $\mu_{O_2}(T, p)$ are the energy of a structure with a single oxygen vacancy, the energy of the perfect structure, and the chemical potential of oxygen gas, respectively, at a particular T and p_{O_2} . Here, $\mu_{O_2}(T, p)$ is defined via the relation:

$$\mu_{O_2}(T, p_{O_2}) = E_{O_2}^{DFT} + \Delta\mu_{O_2}^0(T) + kT\ln p_{O_2} \quad [2.3b]$$

where $E_{O_2}^{DFT}$ is the energy of an oxygen molecule, and the last two terms describe the change in the chemical potential of oxygen from 0 K to T , and under the partial pressure of p_{O_2} . These two terms are collectively referred to as the thermodynamic connection energy to the DFT calculated energy for isolated molecular oxygen. Equation 2.1 is the 0 K version of Equation 2.3a. Equations 2.3a and 2.3b can then be combined with Equation 2.1 to yield:

$$\Delta G_{vac}^f = \Delta E_{vac}^f + \frac{1}{2}(\Delta\mu_{O_2}^0(T) + kT\ln p_{O_2}) \quad [2.4]$$

where the free energy contribution due to the phonon vibration of the extra oxygen atom in the perfect lattice is lumped into $\Delta\mu_{O_2}^0(T)$.¹²¹

Defining the chemical potential of an individual atomic species in a crystalline compound is inherently difficult. In this case, the chemical potential of oxygen in crystal lattice was set by the temperature and pressure of the gas phase O₂, since it is in chemical equilibrium with lattice oxygen.¹²² The energy of oxygen dimer, $E_{O_2}^{DFT}$, and the subsequent oxygen vacancy formation energies are sensitive to the exact choice of exchange-correlation functional, pseudopotential etcetera in DFT calculations. This problem is mitigated by various methods of estimating $\Delta\mu_{O_2}^0(T)$ in the literature.^{121–124} In this paper, the method of Zhang *et al.*¹²¹ was modified to describe oxygen vacancy formation in materials containing Fe-O polyhedra.

Using the derivation provided in Section 2.4.2, $\Delta\mu_{O_2}^0(T)$ was broken into a thermodynamic connection energy from 0 K to room temperature ($\Delta\mu_{O_2}^0(T_r)$), and a thermodynamic connection energy from room temperature ($T_r = 298$ K) to a temperature of interest, T , using the expression:

$$\Delta\mu_{O_2}^0(T) = \Delta\mu_{O_2}^0(T_r) + \int_{T_r}^T C_p \, dT - T \int_{T_r}^T C_p / T \, dT - (T - T_r) S_r \quad [2.5]$$

where C_p is the specific heat of oxygen gas at temperature T , and S_r is the entropy of oxygen gas at the standard state.¹²⁵ It is important to note that the last three terms in Equation 2.5 are easily calculated from the data available in any thermochemistry handbook.^{125,126}

2.4.2. Connecting Chemical Potential of Oxygen from 0 K to T K

Assuming the oxygen atom in the lattice site is in chemical equilibrium with the gas phase oxygen molecule we can write Equation 2.6.

$$\mu_O(T, p) = \frac{1}{2}\mu_{O_2}(T, p) = \frac{1}{2}E_{O_2}^{DFT} + \frac{1}{2}\Delta\mu_{O_2}(T, p) \quad [2.6]$$

where $\Delta\mu_{O_2}(T, p)$ is the thermodynamic connection energy between DFT (0 K) calculated energy of an isolated oxygen molecule with free energy of oxygen molecule at any temperature, T and partial pressure, p . Equation 2.7 brakes $\Delta\mu_{O_2}(T, p)$ into three parts. The first part, $\Delta H_{O_2}|_{0K}^T$ is the enthalpy of connection energy. All the enthalpy related terms in this derivation are highlighted in red color. The second part, $T\Delta S_{O_2}|_{0K}^T$ is related to entropy correction. All the entropy related terms are highlighted in green color. The third part, $kT\ln\left(\frac{p}{p_0}\right)$ is the pressure correction term and highlighted in blue color.

$$\Delta\mu_{O_2}(T, p) = \Delta H_{O_2}|_{0K}^T - T\Delta S_{O_2}|_{0K}^T + kT\ln\left(\frac{p}{p_0}\right) \quad [2.7]$$

Equation 2.8 substitutes the enthalpy and entropy related terms into their integral form.

$$\Delta\mu_{O_2}(T, p_0) = \int_{0K}^T C_p dT - T \int_{0K}^T \frac{C_p}{T} dT + kT\ln\left(\frac{p}{p_0}\right) \quad [2.8]$$

The enthalpy contribution to the connection energy is obtained by integrating the heat capacity, C_p over the temperature range 0 K to T (Equation 2.8) and it is separated into two parts as shown in Equation 2.9 for the ease of calculation. Similarly, the entropy term of the connection energy was also calculated in two parts as shown in Equation 2.10.

$$\Delta\mu_{O_2}(T, p_0) = \Delta h_{O_2}|_{0K}^{T_r=298K} + \int_{T_r=298K}^T C_p dT - T \int_{0K}^T \frac{C_p}{T} dT + kT\ln\left(\frac{p}{p_0}\right) \quad [2.9]$$

Here, $\Delta h_{O_2}|_{0K}^{T_r=298K}$ is the connection enthalpy for oxygen molecule between 0 K and standard state (298 K) which can be obtained in multiple ways as explained in next section.

$$\Delta\mu_{O_2}(T, p_0) = \Delta h_{O_2}|_{0K}^{T_r=298K} + \int_{T_r=298K}^T C_p dT - T \int_{0K}^{T_r=298K} \frac{C_p}{T} dT - T \int_{T_r=298K}^T \frac{C_p}{T} dT + kT\ln\left(\frac{p}{p_0}\right) \quad [2.10]$$

Rearrange the terms in Equation 2.10, it becomes

$$\Delta\mu_{O_2}(T, p) = \Delta h_{O_2}|_{0K}^{Tr=298K} - T \int_{0K}^{Tr=298K} \frac{C_p}{T} dT + \int_{Tr=298K}^T C_p dT - T \int_{Tr=298K}^T \frac{C_p}{T} dT + kT \ln\left(\frac{p}{p_0}\right)$$

[2.11]

Subtracting and adding $T_r \int_{0K}^{Tr=298K} \frac{C_p}{T} dT$ in Equation 2.11 helps us to relate terms with chemical potential of oxygen, as shown in later steps.

$$\begin{aligned} \Delta\mu_{O_2}(T, p) &= \Delta h_{O_2}|_{0K}^{Tr=298K} - T_r \int_{0K}^{Tr=298K} \frac{C_p}{T} dT - (T - T_r) \int_{0K}^{Tr=298K} \frac{C_p}{T} dT + \int_{Tr=298K}^T C_p dT \\ &\quad - T \int_{Tr=298K}^T \frac{C_p}{T} dT + kT \ln\left(\frac{p}{p_0}\right) \end{aligned}$$

[2.12]

Now, $\int_{0K}^{Tr=298K} \frac{C_p}{T} dT$ is the standard entropy and can be obtained from thermodynamic handbook data and represented as S_r in Equation 2.13.

$$\begin{aligned} \Delta\mu_{O_2}(T, p) &= \Delta h_{O_2}|_{0K}^{Tr=298K} - T_r \int_{0K}^{Tr=298K} \frac{C_p}{T} dT - (T - T_r) S_r + \int_{Tr=298K}^T C_p dT \\ &\quad - T \int_{Tr=298K}^T \frac{C_p}{T} dT + kT \ln\left(\frac{p}{p_0}\right) \end{aligned}$$

[2.13]

$$\begin{aligned} \Delta\mu_{O_2}(T, p) &= \Delta h_{O_2}|_{0K}^{Tr=298K} - T_r \int_{0K}^{Tr=298K} \frac{C_p}{T} dT + \int_{Tr=298K}^T C_p dT - T \int_{Tr=298K}^T \frac{C_p}{T} dT \\ &\quad - (T - T_r) S_r + kT \ln\left(\frac{p}{p_0}\right) \end{aligned}$$

[2.14]

Defining the enthalpy and entropy of connection between 0 K and 298 K ($\Delta h_{O_2}|_{0K}^{Tr=298K} - T_r \int_{0K}^{Tr=298K} \frac{C_p}{T} dT$) to be the change in chemical potential of oxygen $\Delta\mu_{O_2}^0(T_r)$ between 0 K and standard state, leads to:

$$\Delta\mu_{O_2}^0(T) = \Delta\mu_{O_2}^0(T_r) + \int_{T_r=298K}^T C_p dT - T \int_{T_r=298K}^T \frac{C_p}{T} dT - (T - T_r) S_r$$

[2.15]

The 0 K to T_r connection energy for oxygen molecule, $\Delta\mu_{O_2}^0(T_r)$ can be calculated in various ways. For instance, Reuter *et al.*¹²⁴ used enthalpy and entropy data for oxygen at low temperatures from a thermochemical handbook¹²⁷ to estimate $\Delta\mu_{O_2}^0(T_r)$ as $T \rightarrow 0$ for their RuO₂ surface calculations. In contrast, Lee *et al.*¹²³ and Wang *et al.*⁹² computed $\Delta\mu_{O_2}^0(T_r)$ by utilizing metal oxide formation reactions. They first took the connection energy of the reaction as the difference between DFT calculated formation enthalpy of oxides and their corresponding enthalpy of formation at standard state, then subtracted the connection energies of metal and oxides obtained by integrating heat capacity and entropy data obtained from thermodynamics handbooks, in a temperature range of 0 K to T_r . We followed the method of Zhang *et al.*¹²¹ They constructed metal oxide thermodynamic cycles to calculate $\Delta\mu_{O_2}^0(T_r)$ for various oxides and showed that it varies with the forming elements since different metal-oxygen bonds are formed.¹²¹ Since Fe-O polyhedra play the lead role in determining the oxygen vacancy concentration in the SrFeO_{3- δ} system, a $\Delta\mu_{O_2}^0(T_r)$ value of -0.56 eV for iron oxide from Zhang *et al.* was used to model SrFeO_{3- δ} . The advantage of Zhang *et al.*'s metal oxide formation based approach¹²¹ is that it implicitly accounts for the vibrational contribution of the oxygen atom in the lattice structure of the metal oxide, and is therefore compatible with the use of Equation 2.4. Various methods exist in the literature to calculate the oxygen connection energy and the chemical potential of oxygen.

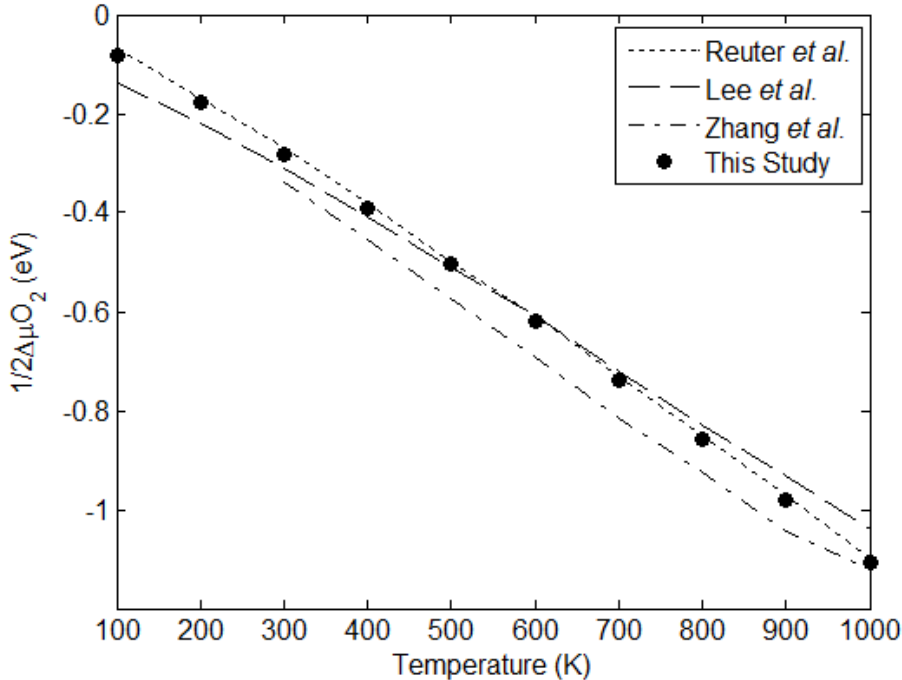


Figure 2.4. Compare different methods to obtain oxygen connection energy in Equation 2.5.

Here, the computed oxygen connection energy, $0.5\Delta\mu_{O_2}(T, p = 1\text{atm})$, was compared in a broad temperature range determined using the present model against other methods available in the literature, as shown in Figure 2.4. Reuter *et al.*¹²⁴ used the CRC handbook values for oxygen connection energy to connect chemical potential of oxygen from 0 K to thermodynamic standard state and they also considered the contribution of phonons. Lee *et al.*¹²³ used an average oxide formation energy shift for oxygen connection energy in their study. All three methods give the same trend of $\Delta\mu_{O_2}^0(T, p)$ decreasing with temperature and similar $\Delta\mu_{O_2}^0(T, p)$ values (which differ by less than 0.1 eV). This suggests that the free energy contribution due to the phonon vibration of the extra oxygen atom in the perfect lattice is not large enough to alter the conclusions presented in this paper. The 0.1eV difference in ΔG_{vac}^f will impact more when ΔG_{vac}^f is small. At most, the predicted $\delta(T)$ relationship shown in Figure 6.4(b) could shift by ~200K at low δ region and by ~100K at high δ region.

2.5. Predicting Ionic Conductivity as a Function of Temperature and Phase Change in Air

To calculate ionic conductivity, σ using Equation 1.1, it is required to compute oxygen vacancy concentration and ionic mobility first, as Z and e are constant for oxygen vacancies.

2.5.1. Oxygen Vacancy Concentration in Bulk Lattice

Oxygen vacancy concentration is directly related to oxygen vacancy concentration as shown in Equation 1.5. If the vacancy formation energy is independent of the oxygen non-stoichiometry (as in case of materials with a dilute concentration of oxygen vacancies), the site fraction of oxygen vacancies (X) at the SOFC operating conditions can be calculated via the expression:^{52,53}

$$\frac{X}{1-X} = \exp\left(-\frac{\Delta G_{vac}^f(T,p)}{RT}\right) \quad [2.16]$$

where R is the ideal gas constant and ΔG_{vac}^f is the vacancy formation free energy calculated via Equation 2.4. However, if ΔG_{vac}^f varies with X (as would be the case for interacting, non-dilute oxygen vacancies), the right hand side of the Equation 2.16 has to be modified to include the change in ΔG_{vac}^f with X . In some cases (for example, cubic SrFeO_{3- \square}), the ΔE_{vac}^f can change as much as 1 eV with X . When this change is more dominant than the configurational entropy contribution (which is ~0.1 eV at temperature > 600°C) due to ordered oxygen vacancies induced by periodic boundary conditions, Equation 2.16 becomes:

$$\frac{X}{1-X} = \exp\left(-\frac{\Delta G_{vac}^f(T,p,X)}{RT}\right) \quad [2.17]$$

(to account for the complex defect configurational entropy contribution, Equation 2.5 should be modified accordingly following the method discussed by Xi *et al.*)¹²⁸ Equation 2.17 needs to be solved to find the correct operating temperature, T for a predetermined pressure, p_{O_2} with

calculated vacancy formation energy for a particular non-stoichiometry. Here, a numerical method with an incremental search technique, presented in the Appendix, was developed to solve Equation 2.17 as X was varied in each phase, T was varied from 0-2000 K and p_{O_2} was held constant at 0.21 atm.

2.5.2. Mobility and Diffusivity of Oxygen Vacancy in Bulk Lattice

Calculated oxygen ion migration barrier with CINEB method (described in Section 2.3.3) will be used to calculate ionic diffusivity in solids. As the ultimate goal is to calculate ionic conductivity using Equation 1.1, so for the calculation of diffusivity in Equation 1.8 only migration barrier will be used in place of activation energy.¹²⁹ Because in Equation 1.1 vacancy concentration already incorporated the free energy of vacancy formation. The diffusivity prefactor D_0 can be calculated from jump distance (d), jump frequency (v), and jump correlation factor (f) using below equation:¹³⁰

$$D_o = \frac{1}{6} f d^2 v \quad [2.18]$$

In a lattice with multiple vacancy migration pathways, d represent the average jump distance. The jump frequency, v was assumed as 10^{13} Hz following the solid state diffusion.¹³¹ Jump correlation factor, f was assumed as 1.¹³² Once diffusivity is calculated at a certain temperature, the calculation of ionic mobility is straight forward from Equation 1.7.

2.6. Anisotropic Chemical Strain Due to Oxygen Vacancy

A 2x2x2 ceria cubic-supercell (Figure 2.5) was used for chemical strain calculation with a single oxygen vacancy (V_O^{--}) formation ($\delta = 0.03125$). Such a low δ was selected to avoid any vacancy-vacancy interaction due to periodic boundary condition.²⁷ In this 2x2x2 $CeO_{2-\delta}$ supercell

the average distance between oxygen vacancies is 11.0 Å. Fully spin-polarized calculations with generalized gradient approximation with Hubbard-*U* (GGA+U) was performed on a perfect and oxygen vacancy containing (defective) lattices. $U_{\text{eff}} = 4.5$ was used to treat Ce *4f* for highly localized nature of *f*-orbital, following the rotationally invariant approach proposed by Dudarev *et al.*⁹⁰ and calculated for ceria by Farbis *et al.*¹³³ This U_{eff} value for Ce *4f* has provided satisfactory results, as reported in previous literature.^{134,135} The partial density of states analyses for Ce atoms adjacent to oxygen vacancy site can confirm the electron localization after the formation of neutral oxygen vacancy. In earlier studies, it was observed that oxygen vacancy produces complicated local deformation due to the charge disproportionation on Ce ($4\text{Ce}^{4+} + 2e^- \rightarrow 2\text{Ce}^{4+} + 2\text{Ce}^{3+}$).^{136,137}

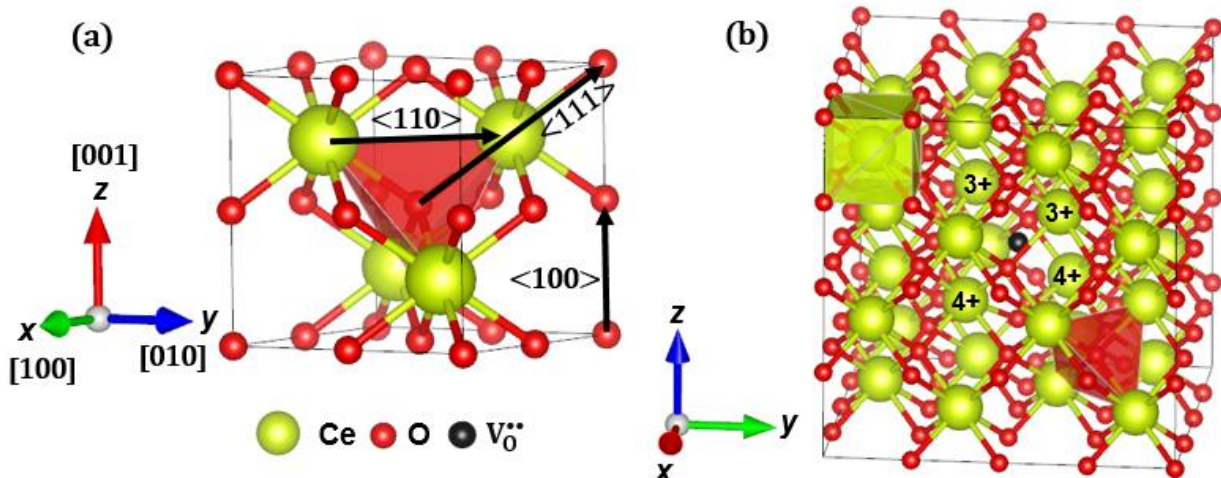


Figure 2.5. (a) CeO_2 unit cell showing O-Ce₄ tetrahedral coordination and Ce-O bonding directions. (b) Charge distribution on Ce around neutral oxygen vacancy formation showing in a 2x2x2 supercell.

Esch *et al.* has shown experimentally, the charge localization on Ce (surface and subsurface) after $\text{V}_0^{\bullet\bullet}$ formation.¹³⁸ Nolan *et al.*¹³⁹ observed charge localization on *f*-orbital forming Ce^{3+} but their two Ce^{3+} were not equidistant from $\text{V}_0^{\bullet\bullet}$. Though the charge disproportionation was observed in previous studies, they didn't use the local lattice deformation to calculate the chemical

strain tensor for the defect containing structure.¹³⁹ In stoichiometric CeO₂ fluorite structure, Ce-O₈ forms cubic coordination but O-Ce₄ forms a tetrahedral coordination (Figure 2.5(b)). As each O is connected with the four Ce⁴⁺ atoms, on formation of V_O^{••}, two electrons should be distributed to the four adjacent Ce atoms but due to the presence of highly localized 4f orbital (as discussed above) two electrons are localized to two Ce-atoms converting them to Ce³⁺, whereas, other two remained Ce⁴⁺. The charge localization is shown in Equation 2.19 with Kröger-Vink notation.



Following the computational study of Tang *et al.*¹⁴⁰ and Castleton *et al.*,¹⁴¹ calculations were performed with two different scenarios. In the first case, atom positions were relaxed after V_O^{••} formation keeping the cell volume constant, where four Ce atoms equally moved away from the V_O^{••} site producing uniform distortion. In the second case, after V_O^{••} formation two Ce atoms were perturbed then atom positions were relaxed keeping the cell volume constant. In second case two Ce atoms moved further than other two, causing asymmetric distribution of Ce atoms around V_O^{••}.

The anisotropic chemical strain coefficient tensor was calculated following the work of James *et al.*⁴² The chemical strain tensor was calculated by minimizing the total energy, ΔE_{total} which consists of energy due to local deformation from oxygen vacancy formation, ΔE_{short} and the energy due to long-range elastic strain, ΔE_{long} . Short range energy change, ΔE_{short} was originated due to local strain dipole, G from the V_O^{••}. The strain dipole can be calculated, taking first order Taylor expansion of V_O^{••} formation energy with strain applied, $E_{V_O^{••},\varepsilon}^f = E_{V_O^{••},\varepsilon=0}^f + G: \varepsilon$, where $E_{V_O^{••},\varepsilon=0}^f$ is the V_O^{••} formation energy without any applied strain. Taking derivative of the preceding equation with respect to ε , we obtain $G = dE_{V_O^{••},\varepsilon}^f/d\varepsilon$. Energy for the short and long range interaction can be obtained as $\Delta E_{short} = \frac{\delta}{V_U} G: \varepsilon$, and $\Delta E_{long} = \frac{1}{2}(\mathbb{C}: \varepsilon): \varepsilon$ respectively. Where, V_U is the volume per formula unit of the perfect CeO₂ and \mathbb{C} is the elastic stiffness tensor of the perfect lattice. Chemical strain tensor, ε_C and chemical expansion coefficient tensor, α_C can

be obtained by minimizing the total energy with respect to ε_C from Equation 2.20. The derivation is provided below:

$$\Delta E_{total} = \Delta E_{short} + \Delta E_{long} = \frac{\delta}{V_U} G : \boldsymbol{\varepsilon} + \frac{1}{2} (\mathbb{C} : \boldsymbol{\varepsilon}) : \boldsymbol{\varepsilon} \quad [2.20]$$

$$\frac{d\Delta E_{total}}{d\boldsymbol{\varepsilon}} = \frac{d\Delta E_{short}}{d\boldsymbol{\varepsilon}} + \frac{d\Delta E_{long}}{d\boldsymbol{\varepsilon}} = 0 \quad [2.21]$$

$$\frac{d\Delta E_{short}}{d\boldsymbol{\varepsilon}} = \frac{d}{d\boldsymbol{\varepsilon}} \left(\frac{\delta}{V_U} \mathbf{G} : \boldsymbol{\varepsilon} \right) = \frac{\delta}{V_U} \mathbf{G} \quad [2.22]$$

$$\frac{d\Delta E_{long}}{d\boldsymbol{\varepsilon}} = \frac{1}{2} \frac{d}{d\boldsymbol{\varepsilon}} \{ (\mathbb{C} : \boldsymbol{\varepsilon}) : \boldsymbol{\varepsilon} \} = \frac{1}{2} \left\{ \frac{d(\mathbb{C} : \boldsymbol{\varepsilon})}{d\boldsymbol{\varepsilon}} \right\} : \boldsymbol{\varepsilon} + \frac{1}{2} (\mathbb{C} : \boldsymbol{\varepsilon}) : \frac{d\boldsymbol{\varepsilon}}{d\boldsymbol{\varepsilon}} \quad [2.23]$$

$$\frac{d\Delta E_{long}}{d\boldsymbol{\varepsilon}} = \frac{1}{2} \left\{ \mathbb{C} : \frac{d\boldsymbol{\varepsilon}}{d\boldsymbol{\varepsilon}} \right\} : \boldsymbol{\varepsilon} + \frac{1}{2} (\mathbb{C} : \boldsymbol{\varepsilon}) : \frac{d\boldsymbol{\varepsilon}}{d\boldsymbol{\varepsilon}} = \frac{1}{2} (\mathbb{C} : \boldsymbol{\varepsilon}) + \frac{1}{2} (\mathbb{C} : \boldsymbol{\varepsilon}) = \mathbb{C} : \boldsymbol{\varepsilon} \quad [2.24]$$

$$\frac{d\Delta E_{total}}{d\boldsymbol{\varepsilon}} = \frac{\delta}{V_U} \mathbf{G} + \mathbb{C} : \boldsymbol{\varepsilon} = \mathbf{0} \quad [2.25]$$

$$\varepsilon_C = \frac{-\delta (\mathbb{C}^{-1} \mathbf{G})}{V_U} \quad [2.26]$$

$$\alpha_C = \frac{\varepsilon_C}{\delta} = \frac{-(\mathbb{C}^{-1} \mathbf{G})}{V_U} \quad [2.27]$$

3. DFT+U as a Reliable Tool to Predict Lattice Structure and Electronic Properties of MIEC at Low Temperature

This Section studies the perfect LSF lattices with DFT+U (0 K) calculations. Here, we have summarized properties like magnetic orientation, band structure, lattice parameters etc from 0 K calculations. The predicted properties can be compared with low-temperature experimental observations.

Table 3.1. DFT predictions of stable LSF structures under ground-state conditions.

Method GGA + U (=3)			SrFeO ₃		LSF55			LaFeO ₃		
Input Crystal Structure	Spin	ΔE (eV)	μ _B	tilt angle	ΔE (eV)	μ _B	tilt angle	ΔE (eV)	μ _B	tilt angle
Orthorhombic (PNMA)	FM	0.00	3.61	177	0.00	3.94	161	0.26	4.23	152
	AFM	0.23	3.41	175	0.04	3.76	159	0.00	4.06	154
Rhombohedral (R32)	FM	0.00	3.61	180	0.00	3.94	164	0.34	4.24	155
	AFM	0.26	3.48	173	0.06	3.78	164	0.05	4.06	157
Cubic (FM-3M)	FM	0.00	3.61	180	0.09	3.94	180	0.88	4.14	180
	AFM	0.26	3.50	180	0.14	3.74	180	0.40	4.03	180
Experimental (low temp)*		Helical ¹⁰⁵	2.96 ¹⁰⁵	180 ¹⁴²	FM ⁸⁷	3.92 ⁸⁷	166 ¹⁴³	AFM ¹⁴⁴	4.6±0.2 ¹⁰⁰	157 ⁸⁶

The bold phase data under each column signify the stable structure with the preferred magnetic orientation.

The tilt angle column denotes the average octahedral tilt among Fe-O octahedra in the lattices.

* The last row contains experimental data for comparison.

Figure 2.1 shows the energetically favored crystal structures for LFO, SFO, and LSF55. In order to determine the ground state lattice structure for each LSF composition, three possible crystal structures each with two possible Fe magnetic ordering arrangements (ferromagnetic, FM, and anti-ferromagnetic, AFMG), were computed. From energy minimization, the stable, lowest-energy structures, presented in Table 3.1, were determined and illustrated in Figure 2.1. In Table 3.1, ΔE denotes the excess energy of a structure above the minimum energy of each composition, the ‘μ_B’ column denotes the magnetic moment on Fe in the structure, and the “tilt angle” denotes the Fe-O₆ octahedral tilt angle (which varies with the lattice structure and La/Sr ratio).

3.1 Predicting Ground State Lattice Structure and Magnetic Ordering in La_{1-x}Sr_xFeO_{3-δ} Phases

In accordance with experiments,¹⁰⁰ the orthorhombic (*Pbnm*) crystal structure with AFMG ordering was predicted as the stable LFO structure. The calculated lattice of 5.672 Å x 7.923 Å x 5.582 Å also compared well to the experimentally reported lattice parameters.^{86,100} The Fe-O₆ octahedra in LFO showed a Z-out distortion (the b-axis in Figure 2.1(a)) with four 2.040 Å Fe-O bonds in the XY plane (the ac plane in Figure 2.1(a)) and two 2.057 Å bonds in the Z-direction (b-axis in Figure 2.1(a)). These Fe-O bond lengths are comparable to the experimentally measured average bond length of 2.006 Å.⁸⁶ The computed octahedral tilt was 154° (the bond angle of Fe-O-Fe) which was comparable to experimentally reported octahedral tilt of 157°.⁸⁶

For stoichiometric SFO, the predicted phase is the experimentally reported low-temperature cubic structure (space group: *Pm*̄*3m*) with FM Fe ordering and a lattice parameter of 3.881 Å, which agreed well with experiments³² (note, FM ordering was used to simplify the experimentally-reported helical Fe magnetic orientation arrangement in the 2K neutron diffraction SFO study of Reehuis *et al.*).¹⁰⁵ The predicted magnetic moment on Fe was 3.61 μ_B, which is similar to a literature DFT+U value of 3.7 μ_B calculated with U=5.4.¹⁰¹ All the Fe-O bond lengths in SFO were equal to 1.940 Å due to octahedral (O_h) symmetry (Figure 2.1(d)) and were comparable to the experimentally reported bond length of 1.928 Å (measured at room temperature).¹⁴⁵ A detailed study on other SFO phases are provided in Section 3.3.

For LSF55, the cubic, orthorhombic, rhombohedral structures were computed. The unit cell for rhombohedral LSF55 was depicted by a hexagonal lattice following the work of Kharton *et al.*⁴⁶ In light of the 0 to ~600K single phase behavior of LSF55 observed by X-ray diffraction^{65,143,145} and the insensitive oxygen vacancy formation energy on the site ordering of La/Sr simulated by Ritzmann *et al.*,²⁴ a La/Sr ordered LSF55 phase was assumed. Thus, the 6a

Wyckoff positions were assumed to be equally shared by La and Sr and an alternate layer of La-O and Sr-O was assumed, separated by the Fe-containing layer, as shown in Figure 3.1(b). The present calculations correctly predicted that a hexagonal (rhombohedral) lattice structure with an *R*32 space group is energetically favorable for LSF55. The calculated lattice length of the hexagonal unit cell was $a = 5.564 \text{ \AA}$ and $c = 13.451 \text{ \AA}$, and compared well with the experimental values ($a = 5.5150 \text{ \AA}$, $c = 13.4287 \text{ \AA}$).⁴⁶ In any octahedron, three of the calculated Fe-O bond lengths were 1.986 \AA and the other three were 1.971 \AA . Along the Fe-O-Fe-O direction, the Fe-O-Fe bond angle between two Fe-O₆ octahedra alternated between 166° and 161° and the Fe-O bond lengths also alternated between 1.986 and 1.971 \AA . These calculated bond lengths are comparable to experimentally reported the average Fe-O bond length of 1.954 \AA (at room temperature).¹⁴⁵ Although it was predicted that FM order had a lower energy than AFM, the energy difference was only ~0.06 eV/f.u., and hence not in disagreement with the AFM magnetic orientation measured in LSF55 with Mössbauer spectroscopy at 78 K.⁹⁸

3.2. Density of States for LaFeO_{3- δ} and La_{0.5}Sr_{0.5}FeO_{3- δ}

Figure 3.1 shows the band gap for each energetically favored lattice structure. The partial density of states (PDOS) was calculated for both FM and AFMG ordering in LFO as shown in Figures 3.1(a) and 3.1(b). The computed band gap was 0.5 and 2.0 eV for FM and AFMG ordering, respectively. The band gap predicted in AFMG LFO was comparable to the experimentally observed optical band gap of 2.1 eV measured at room temperature.¹⁴⁶ Cubic SFO shows a metallic behavior,¹⁰⁵ as correctly predicted in Figure 3.2(a). The detailed study on measured properties for the different SrFeO_{3- \square} phases are provided in Section 3.3. The PDOS was calculated for both FM and AFMG magnetic ordering in LSF55 and reported in Figure 3.1(c) and 3.1(d). Though there

are few DOS observed close to Fermi energy with an FM orientation (Figure 3.1(c)), the AFMG ordered structure has an energy gap of 1.6 eV, comparable to earlier computational studies.²⁴ Overall, the DFT settings successfully predicted that orthorhombic AFM, rhombohedral (hexagonal) (FM or AFM), and cubic (FM) were stable structures for LFO, LSF55, and SFO, respectively, at low temperature.

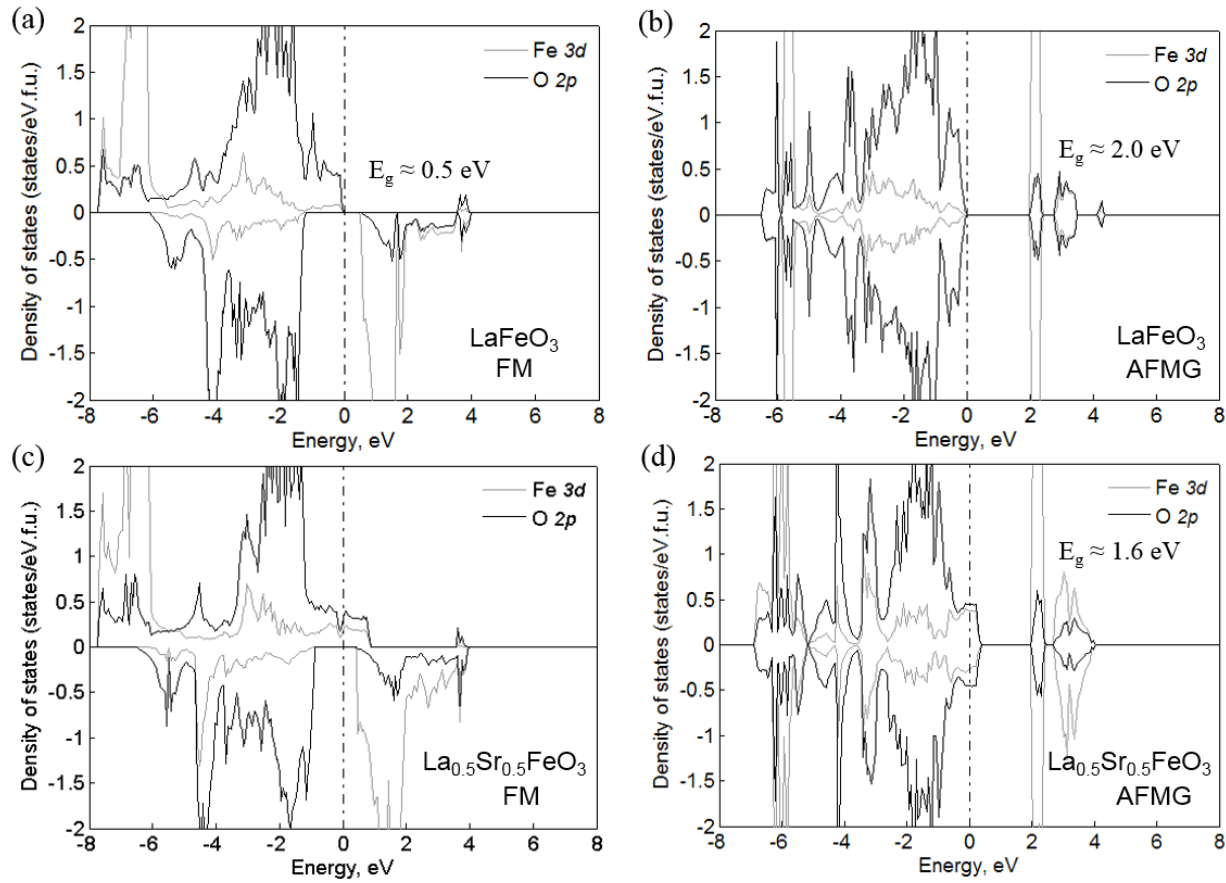


Figure 3.1. GGA+U (=3) partial density of states calculations for (a-b) orthorhombic LaFeO_3 , (c-d) rhombohedral $\text{La}_{0.5}\text{Sr}_{0.5}\text{FeO}_3$. The gray and black lines represent the Fe 3d and O 2p states respectively.

3.3. Study of Different $\text{SrFeO}_{3-\delta}$ Phases

Table 3.1. Comparison of DFT-calculated and experimentally-measured lattice parameters, magnetic ordering, and band gaps for several phases of $\text{SrFeO}_{3-\delta}$ (“See DOS” in the last column of below-provided table refer to the Figure 3.1 for the density of states plot). N.C. stands for Not Calculated. Experimental Néel Temperature, T_N , is also listed for each phase.

Phase	Symmetry	T_N (K)	Mag. Order	Energy /f.u. (eV)	Lattice Parameter			Band Gap, E_g (eV)
					a	b	c	
SrFeO_3	cubic (Pm $\bar{3}$ m)	133 ¹⁰⁵	Calc	FM	-32.70	3.88	-	Metallic
				AFMG	-32.44	3.89	-	N.C.
			Expt	Helical at 2K ¹⁰⁵	-	3.85 ^{32*}	-	Metallic ¹⁰⁵
$\text{SrFeO}_{2.875}$	tetragonal (I4/mmm)	75 ¹⁰⁵	Calc	FM	-32.03	11.03	-	7.76
				AFMG	-31.95	11.04	-	7.78
			Expt	Helical at 2K ¹⁰⁵	-	10.93	-	7.70 ^{32*} < 1 ¹⁴⁷
$\text{SrFeO}_{2.75}$	Orthorhombic (Cmmm)	232 ¹⁰⁵	Calc	FM	-31.30	11.09	7.78	5.52
				AFMG	-31.40	11.05	7.80	5.51
			Expt	AFMG at 2K ¹⁰⁵	-	10.97	7.70	5.47 ^{32*} 1 – 1.5 ¹⁴⁷
$\text{SrFeO}_{2.5}$	Brownmillerite (Ibm2)	700 ¹⁴⁸	Calc	FM	-29.83	5.58	15.70	5.77
				AFMG	-30.10	5.57	15.62	5.74
			Expt	AFMG at 4.8K ¹⁴⁸	-	5.53	15.57	5.67 ^{149#} 1.5 ± 0.2 ₁₄₇

* Calculated from neutron powder diffraction data

Calculated from powder X-ray diffraction data

Figure 1.1 shows the calculated perfect crystal structures (at $X=0$), the charge state of Fe, and the various oxygen sites for each of the perfect $\text{SrFeO}_{3-\delta}$ phases observed from 0-1000°C in the air: cubic SrFeO_3 , tetragonal $\text{SrFeO}_{2.875}$, orthorhombic $\text{SrFeO}_{2.75}$, and brownmillerite $\text{SrFeO}_{2.5}$. Table 3.1 lists the computed lattice parameter, magnetic ordering, and band gap information on these phases with the DFT settings discussed in Section 2.1.1. As discussed, $U_{eff} = 3$ led to the best agreement of magnetic moment and lattice parameters with the experimental values for both LaFeO_3 and SrFeO_3 bulk structures compared to other U-parameters over the range of 0.2 to 4.0.

The computed lattice parameters for all four phases of $\text{SrFeO}_{3-\delta}$ were also in good agreement with experimental results.

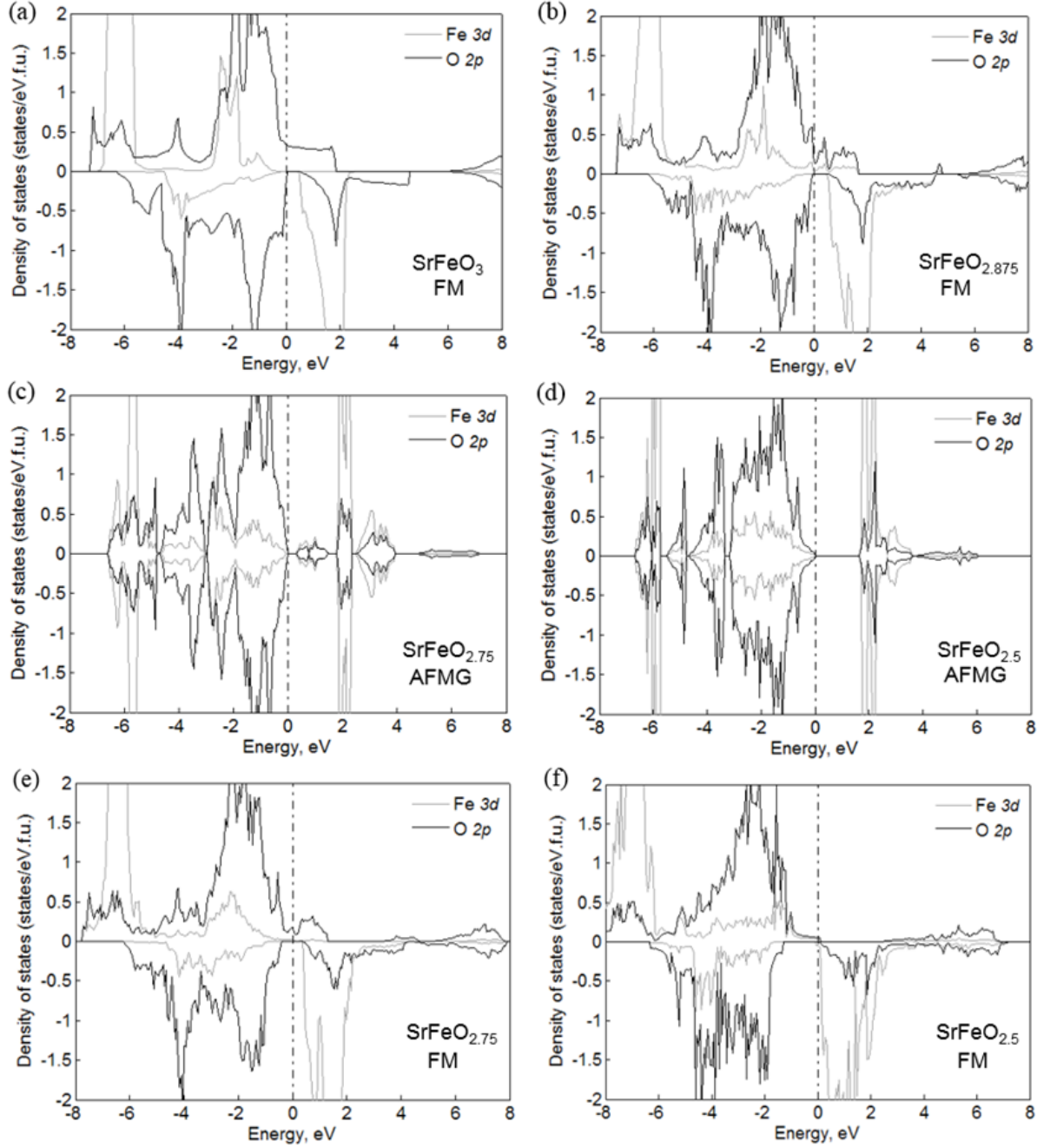


Figure 3.2. GGA+U ($U_{\text{eff}} = 3$) PDOS for four different $\text{SrFeO}_{3-\delta}$ phases. The gray and black line represent Fe 3d and O 2p states respectively. The stoichiometric SrFeO_3 has shown metallic behavior. Whereas, band gaps are observed in oxygen deficient phases.

3.3.1 Magnetic Orientations of SrFeO_{3-δ} Phases

SrFeO_{3-δ} displays complicated magnetic ordering. Reehuis *et al.*¹⁰⁵ detected incommensurate magnetic structure in cubic SrFeO₃ (helical) and SrFeO_{2.87} with neutron diffraction at 2 K. They also reported commensurate G-type antiferromagnetic (AFMG) ordering for SrFeO_{2.75} in the same study. Greaves *et al.*¹⁵⁰ reported AFMG ordering on brownmillerite SrFeO_{2.5} by analyzing neutron powder diffraction data collected at 4.2 K. For cubic SrFeO₃, 0 K DFT+U ($U_{eff} = 3$) calculated energies for different AFM (G, A, C) and ferromagnetic (FM) configurations indicate that FM has the lowest energy (AFMG and FM energies are compared in Table 3.1). Due to computational complexity, FM ordering for Fe in cubic SrFeO₃ was chosen instead of helical ordering. Like the helical magnetic structure, FM ordering also maintains the metallicity of cubic SrFeO₃, as later shown with the density of states calculations. Further, these low temperature (0 K) calculations indicate that while the FM structure has lower energy in cubic and tetragonal phases, orthorhombic and brownmillerite phases show lower energy in AFMG structures.^{105,150} In addition, the calculations correctly predict the experimentally-observed AFM structures in SrFeO_{2.75} and SrFeO_{2.5}. Although Fe ions in SrFeO_{3-δ} phases display AFM orientation at low temperature,¹⁵¹ the energy difference is small (less than 0.26 eV). Furthermore, these materials are well above their Neel temperatures at the SOFC operating temperatures of interest.^{105,152,153} Therefore, in the present work it was not considered necessary to account for antiferromagnetic ordering¹²³ when performing oxygen vacancy formation computations at SOFC operating temperatures, and only ferromagnetic ordering was utilized. As orthorhombic and brownmillerite phases prefer AFMG orientation at low temperature, we have calculated oxygen vacancy formation in these two phases. Our calculations showed that vacancy formation energies in AFMG orthorhombic and brownmillerite phases were ~0.4 and ~0.2 eV higher than their ΔE_{vac}^f (1.3 and 3.0 eV respectively)

in FM phases. Further converting these oxygen vacancy formation energy to Gibbs free energy using Equation 4 and relating corresponding oxygen nonstoichiometry with temperature applying Equation 7 showed that AFMG orthorhombic and brownmillerite phases overestimated the required temperature for the oxygen nonstoichiometry by 280°C and 140°C respectively at $p_{O_2} = 0.21$ atm. Therefore, it was reasonable to perform oxygen vacancy calculations on FM $SrFeO_{3-\delta}$ phases.

3.3.2. Density of States for $SrFeO_{3-\delta}$ Phases

It is known that GGA calculations underestimate the band gap in materials, and GGA+U sometimes can predict band gaps closer to experimental values.¹⁵⁴ Figure 3.2 shows the GGA+U ($U_{eff} = 3$) predicted partial density of states (PDOS) plots of Fe 3d and O 2p orbitals in the phases of $SrFeO_{3-\delta}$. In order to compare with low-temperature experimental results, the PDOS for the four low-temperature phases were first plotted in Figure 3.2 (a-d). Figure 3.2(a) shows that no band gap exists in the bulk cubic FM $SrFeO_3$ structure, consistent with its observed metallic behavior.¹⁰⁵ Figure 3.2(d) shows Brownmillerite AFMG $SrFeO_{2.5}$ has a clear band gap of 1.7 eV, which is comparable to the experimental band gap of 1.5 ± 0.2 eV.¹⁴⁷ Figure 3.2(b) shows that tetragonal FM $SrFeO_{2.875}$ has no distinct band gap. However, the density of states is relatively low within the region of the Fermi level to 0.3 eV above, which may be related to the observed small band gap in this phase. Figure 3.2(c) shows orthorhombic AFMG $SrFeO_{2.75}$ has a band gap of ~ 1.7 eV but small polaron states exist in the band gap region. No experiments on the exact composition of these two phases have been reported. However, experimental bandgap values of 1.5 ± 0.2 and 1.0 ± 0.2 eV were observed for non-stoichiometric $SrFeO_{3-\delta}$ i.e., $SrFeO_{2.52}$ and $SrFeO_{2.82}$ respectively.¹⁴⁷ GGA+U ($U_{eff} = 3$) gives reasonable values of band gaps in $SrFeO_{3-\delta}$, especially since it captures the metallic to insulator transition from cubic $SrFeO_3$ to Brownmillerite $SrFeO_{2.5}$. Since the oxygen

vacancy concentrations will be computed using FM phases, Figure 3.2(e) and 3.2(f) present the PDOS for these two structures. These figures show that a low DOS exists around and below the Fermi level in orthorhombic FM $\text{SrFeO}_{2.75}$ and Brownmillerite FM $\text{SrFeO}_{2.5}$, consistent with the high electronic conductivity in these phases at SOFC operating conditions.

3.3.3. Formation Enthalpy of Brownmillerite $\text{SrFeO}_{2.5}$

Before calculating the oxygen vacancy formation energy, the enthalpy of formation for brownmillerite (FM and AFMG both) phases were calculated and compared with experimental data to further calibrate the choice of DFT+U parameters. The formation enthalpy of brownmillerite $\text{SrFeO}_{2.5}$ from its constituent simple oxides was calculated as 0.58 eV and 0.86 eV for FM and AMFG phases, respectively using Equation 3.1:



The enthalpy of formation of the FM brownmillerite phase is comparable with previous computational results obtained using the GGA method (0.54 eV)¹⁵⁵ and with experimental estimation at room temperature (0.48 ± 0.02 eV).¹⁵⁶

3.3.4. *d*-Orbital Splitting and Its Impact on the Iron Oxidation State

Outside a crystal lattice, the half-filled outer *d*-orbital of Fe^{3+} (with a [Ar] $3d^5$ electron configuration) makes it energetically more stable than Fe^{4+} (with a [Ar] $3d^4$ electron configuration). However, in strontium ferrite, crystal field Fe-O *d*-orbital splitting dramatically alters the local charge state of iron. As clearly demonstrated in the calculations here and determined from the literature of Fe magnetic moment experiments,^{32,33} the outer Fe *3d* electrons in strontium ferrite adopt a high spin configuration. Thus, Fe^{4+} in SP coordination has $e_g^2 b_{2g}^1 a_{1g}^1$ configuration that

requires significant amounts of energy (based on the high energy of the SP b_{1g} site in Figure 3.3(a)) to make it a Fe^{3+} with an $e_g^2 b_{2g}^1 a_{1g}^1 b_{1g}^1$ electron configuration. In contrast, Figure 3.3(b) and past experiments¹⁰⁵ show that the Oh coordinated Fe^{4+} in cubic SrFeO_3 with an electronic configuration of $t_{2g}^3 e_g^1$ requires less energy to become Fe^{3+} (based on the lower energy of the Figure 3.3(b) e_g orbital compared to the Figure 3.3(a) b_{1g} orbital). Even in distorted Oh of tetragonal strontium ferrite (as shown in Figure 3.3(c)), Fe^{4+} with a $b_{2g}^1 e_g^2 b_{1g}^1$ electron configuration that can relatively easily be reduced compared to the Fe^{4+} in SP. This is the underlying reasons for the various Fe charge distributions found within different $\text{SrFeO}_{3-\delta}$ phases.

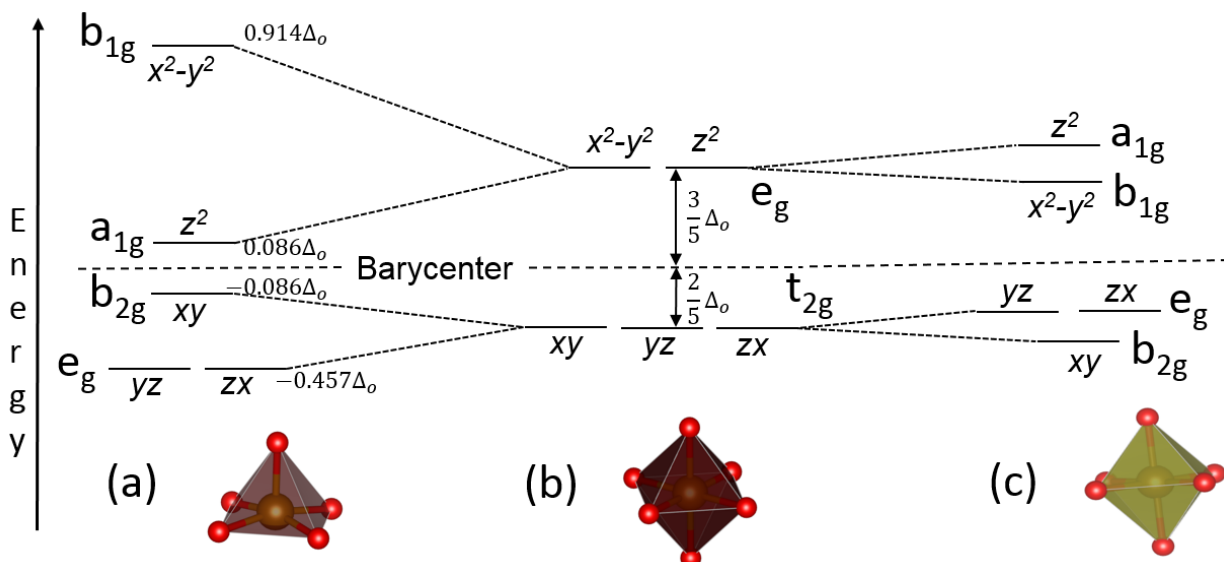


Figure 3.3. Crystal Field Theory explains d-orbital splitting and electronic distribution for different Fe-O polyhedra. (a) Square pyramidal Fe-O coordination, (b) octahedral Fe-O coordination (c) Compressed octahedral Fe-O coordination with Jahn-Teller distortion.

3.3.5. Solving the Debate on Fe Oxidation State at Square Pyramidal and Octahedral Sites

The Fe charge distribution reported here also resolves the debate regarding the charge state of Fe ions in strontium ferrite phases containing mixed iron oxidation states, such as tetragonal $\text{SrFeO}_{2.875}$ and orthorhombic $\text{SrFeO}_{2.75}$. In particular, there has been much debate over whether SP

coordinated iron is Fe^{4+} ^{32,35} or Fe^{3+} .^{33,34,36,60} For instance, Hodges *et al.*³² concluded from their Mössbauer study and empirical bond strength analysis that Fe^{4+} and Fe^{3+} ions occupy the SP and Oh sites respectively. Adler³⁵ produced similar conclusions based on his Mössbauer analysis. On the contrary, Schmidt *et al.*³³ assigned the Fe inside the SP to be Fe^{+3} and the Fe inside Oh to be Fe^{+4} , based on the magnetic structure obtained from Mössbauer measurements. Unfortunately, Schmidt *et al.*'s conclusion may be due to the incorrect assumption that the observed Fe-O octahedra compression resulted from Fe^{+4} induced Jahn-Teller distortions.³³ This assumption is at odds with 1) literature Mössbauer studies on cubic SrFeO_3 showing that octahedrally coordinated Fe^{+4} has no Jahn-Teller distortion,^{142,157} and 2) results here indicating there is no Jahn-Teller distortion for Fe-O Oh containing Fe^{+4} in either SrFeO_3 or $\text{SrFeO}_{2.875}$. In fact, Jahn-Teller distortions are only observed for octahedra containing Fe with oxidation states ranging from +3 to +3.6 based on the present work. In contrast to the results reported here, DFT calculations by Vidya *et al.*³⁴ and Ravindran *et al.*^{36,60} have also claimed SP iron to be Fe^{+3} . However, those modeling results are likely to be incorrect since those studies did not apply U corrections to their GGA-based simulations, and U parameters are generally needed to correct the orbital energies of partially occupied localized *d*-states in Fe-O polyhedra.⁹¹

3.4. Choices of Crystal Structures at SOFC Operating Temperature

Since high temperature oxygen vacancy nonstoichiometry is important for SOFC applications, oxygen vacancy formation was studied in the high-temperature LSF phases experimentally determined to be stable.^{65,158} In terms of high-temperature crystal structure, although LFO transforms from orthorhombic to rhombohedral at 1278 ± 5 K (in air), rhombohedral LFO was not considered since the phase transition temperature is above typical SOFC operating temperatures. On the other hand, LSF55 shows a second order phase transition from rhombohedral to high-temperature cubic at around 523 ± 50 K (in air).⁶⁵ For this reason, oxygen vacancy formation

calculations were performed in both cubic and rhombohedral LSF55 phases. The rhombohedral LSF55 structure is shown in Figure 2.1(c). SFO undergoes multiple vacancy ordering induced phase transitions as it progresses from cubic to tetragonal to orthorhombic to brownmillerite in a temperature range of 273 to 1273 K.⁴⁴ The oxygen vacancy formation calculations in these four SFO phases were performed by Das *et al.*,²⁷ and some of those computational results are presented in this paper for comparison. As shown in Figure 2.1, in all these structures, the perovskite (ABO_3) B-site (transition metal, here Fe) was coordinated to six oxygen atoms, forming an octahedral (Oh) Fe-O₆ coordination.¹⁵⁹ All the oxygen atoms were shared by two octahedra at their corners. After oxygen vacancy formation, the octahedral Fe adjacent to oxygen vacancy formation site went into Fe-O₅ square-pyramidal (SP) coordination.

In term of magnetic ordering, the Néel temperature for LFO is 750 K¹⁰⁰, and it is rapidly reduced with increasing Sr content. In fact, for LSF55 it is ~210 K,⁸⁷ and for SFO it is 133 K.¹⁰⁵ These Néel temperatures are much below the temperature range used for SOFC operation (and hence the oxygen vacancy site fraction calculations). Thus, Fe in all the LSF phases lose their magnetic ordering and become paramagnetic (PM) at the SOFC operating temperature (>1000 K). However, due to the computational complexity of modeling PM ordering, FM ordering was assumed on Fe,^{27,55} for all oxygen vacancy formation calculations.

4. Oxygen Vacancy Interaction via Vacancy Polaron

This study first time explains the oxygen vacancy interaction in compounds of LSF family via oxygen vacancy polaron. The oxygen vacancy polaron plays a significant role in controlling oxygen vacancy concentration due to vacancy interaction at a higher concentration as discussed in Chapter 5.

4.1. Origin of Long Range Charge Transfer due to Oxygen Vacancy Polaron

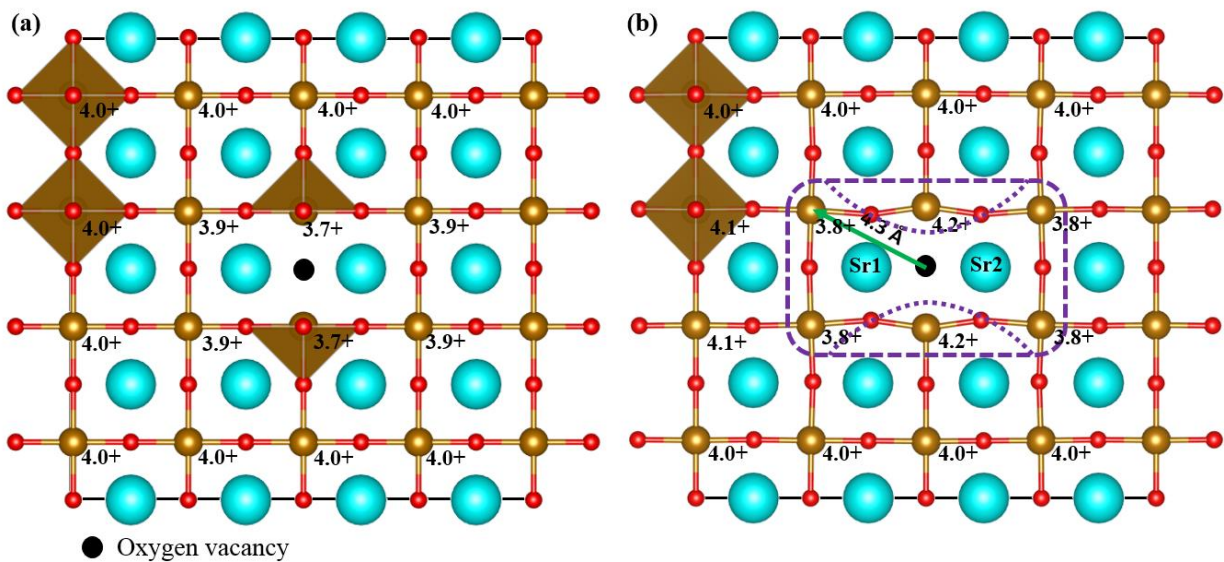


Figure 4.1. The charge distribution on Fe due to oxygen vacancy formation is described on vacancy containing lattice plane of a $4 \times 4 \times 4$ cubic SrFeO_3 supercell with a single oxygen vacancy at the center of the cell. Figure (a) is the lattice plane without relaxing the atom position (only electron cloud is allowed to relax after vacancy formation). Figure (b) is the lattice plane containing atoms after relaxing the atom positions. The light brown atoms are Fe and red atoms are O. The light blue Sr atoms are above or below the described planes. The oxygen vacancy is denoted with a black dot. Figure (a) and (b) contains the oxygen vacancy at the center of the (200) lattice plane. The charge on every Fe atom, rounded to the nearest tenth, is listed next to each Fe atom.

The strong long-range interactions between oxygen vacancies in cubic $\text{SrFeO}_{3-\square}$ can be explained by the unique charge transfer mechanism that occurs in this material, which is also due to the different Fe-O d -orbital splitting in Oh and SP. For instance, Figure 4.1 shows how oxygen

vacancy formation affects the charge of neighboring Fe in cubic $\text{SrFeO}_{2.98}$. Here, one oxygen vacancy is created at the center of a $4\times 4\times 4$ cubic SrFeO_3 supercell, in which the distance between the oxygen vacancies is 15.52 \AA (i.e. larger than the interaction distance of 11 \AA identified in Section 5.2). In this (200) oriented cross-section, the oxygen vacancies and the center of the Oh-Oh octahedra sit on the plane, while the Sr atoms sit above and below the plane. Figure 4.1(a) shows the unrelaxed crystal structure after an oxygen vacancy is created. Here, the Fe sits on the basal plane of the SP polyhedra, and oxygen vacancy formation has reduced the charge on the two iron atoms bordering the oxygen vacancy from $4+$ to $3.7+$. In contrast, Figure 4.1(b) shows that after atomic relaxation, the Fe relaxes into the SP structure by moving 0.10 \AA from the SP basal plane, and the O in the SP polyhedra have moved toward the SP Fe. Together, these changes decrease Fe-O bond lengths in the SP polyhedra and increase those in the neighboring Oh polyhedra. Further, after the atomic relaxation, the two iron atoms in SP coordination become $\text{Fe}^{4.2+}$. Due to the different Fe-O *d*-orbital splitting in Oh and SP, the SP iron adjacent to a newly created oxygen vacancy in a cubic or tetragonal $\text{SrFeO}_{3-\delta}$ structure (not shown) remains $4+$ by maintaining its unpaired electron and passes the electrons resulting from oxygen loss to nearby octahedrally coordinated iron instead of reducing its own oxidation state. The transfer of electrons to the second nearest neighboring Fe atoms, instead of localization on the Fe atoms connected to the oxygen vacancy (i.e. transfer to the first nearest neighbor Fe atom) is a previously unknown long-range charge transfer mechanism. This comparison also indicates that structural relaxations are a necessary step for observing Fe^{4+} in SP polyhedra. The charge transfer discussed here was calculated at 0 K , although electrons will be more delocalized, as this material remains paramagnetic at SOFC operating temperature, it is anticipated that the d-orbital splitting for Oh and SP coordination will qualitatively remain same (as shown in Figure 3.3) with increasing

temperature and/or a with change in oxygen partial pressure; only the gap between energy levels will change which is not going to impact the overall electronic distribution. Thus, the long-range charge transfer phenomena originated by different d-orbital splitting in Oh and SP will still present.

Surrounding each oxygen vacancy, the eight Fe atoms connected to the SP polyhedra via the SP basal plane oxygen are reduced from 4+ to 3.8+. Therefore, one can think of the vacancy polaron as having a “pan-cake” shape that encloses these reduced Fe atoms, where the purple dotted line in Figure 4.1(b) represents the cross-section of the pancake. As shown in Figure 4.1(b), the distance from the oxygen vacancy to the reduced Fe is ~4.3 Å. Due to the reduced charge on these Fe, vacancy formation around them becomes more difficult. This results in the increased oxygen vacancy formation energy when the distance between the vacancies is less than twice of 4.3 Å (i.e. when the vacancy polarons overlap). Thus, the long-range charge transfer on Fe is responsible for the strong vacancy interaction (indicated by the rapid increase in ΔE^δ when $\delta > 0.1$ in Figure 5.2) occurring when the distance among oxygen vacancies is within 8 Å, as is true for all SrFeO_3 -□ compositions with $\delta > 0.1$. Due to the anisotropic shape of the vacancy polaron, one would expect that they may prefer to be aligned along the short-axis of the pancake, which will be subject to future studies, and may illuminate the oxygen vacancy ordering and phase transformation mechanisms. This may lead to some low energy configurations, so ΔE_{vac}^f for cubic $\text{SrFeO}_{3-\square}$ at high □ will be lowered, but the increasing trend of ΔE_{vac}^f with □ should not change due to the long-range charge transfer induced repulsion interaction.

4.2.Oxygen Vacancy Polaron in Different $\text{La}_{1-x}\text{Sr}_x\text{FeO}_{3-\delta}$ Phases

In this section, the vacancy formation sites and the oxidation state changes on Fe upon oxygen vacancy generation in various LSF phases were analyzed to determine the shape and size of the

oxygen polarons shown in Figure 4.2. The Fe oxidation state changes on were explained by the electron occupancy and crystal-field-theory schematics shown in Figure 4.3.

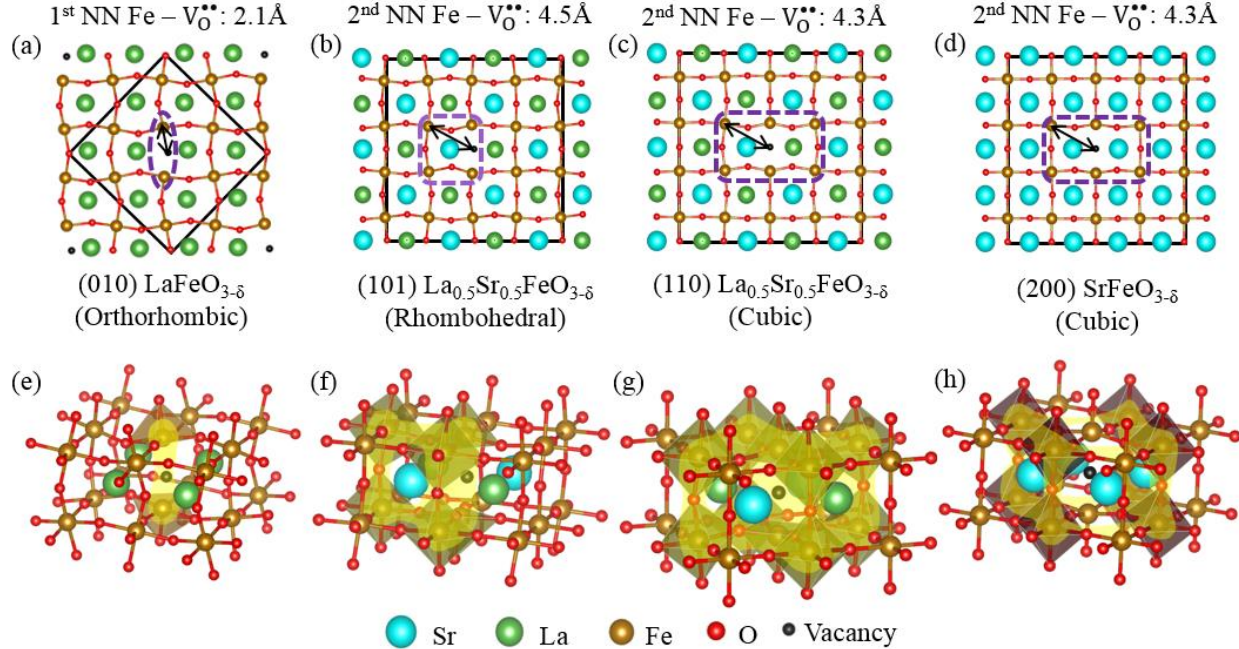


Figure 4.2. Long-range charge transfer areas (denoted by the purple dashed lines in a-d) and perspective views of the $\text{La}_x\text{Sr}_{1-x}\text{FeO}_3$ lattice polarons (e-h) for (a, e) orthorhombic LaFeO_3 , (b,f) rhombohedral $\text{La}_{0.5}\text{Sr}_{0.5}\text{FeO}_3$, (c,g) cubic $\text{La}_{0.5}\text{Sr}_{0.5}\text{FeO}_3$, and (d,h) cubic SrFeO_3 . Note, in (a-d) different Miller planes were used for each phase to compare lattice orientation with same visual conformity. In (e-h) the polaron shape was highlighted by only drawing sides to those Fe-O polyhedra with a Fe atom that received excess electrons due to oxygen vacancy formation. In (a-d), the black lines indicate the border of the supercells used for computations, while the arrows provide an estimate of the polaron size by denoting the distance from the outermost charge-altered Fe atoms to the oxygen vacancy site.

4.2.1. $\text{LaFeO}_{3-\delta}$

In LFO, there are two different oxygen vacancy formation sites, one of which is between the long (2.057 Å) and short (2.040 Å) Fe-O bonds while the other one is between two short (2.040 Å) Fe-O bonds (Figure 2.1(a)). The oxygen vacancy formation calculations showed that the two-different oxygen vacancy formation sites have similar oxygen vacancy formation energies, differing by less than 0.01eV (i.e. within the energy resolution of the present study). The magnetic moment

interpreted charge discussed in Section 2.1, showed that after oxygen vacancy formation, the two Fe atoms connected to the oxygen vacancy site changed their charge states from 3+ to 2.3+, while all the other Fe atoms in the lattice maintained their charge at 3+ (as in perfect LFO).

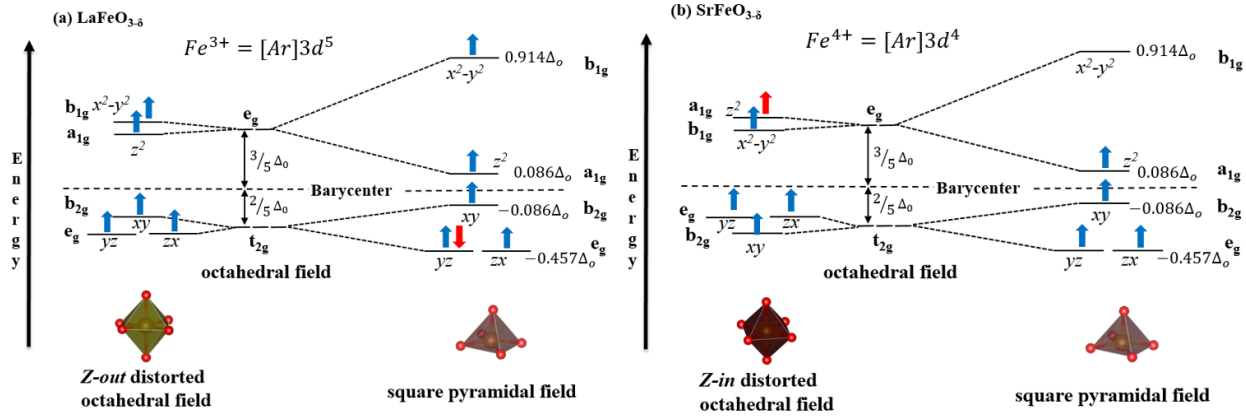


Figure 4.3. Schematic of the d -orbital splitting in the Fe in different polyhedra showing that the excess electrons generated during oxygen vacancy formation (in red) will be localized to oxygen vacancy adjacent square pyramidal Fe in orthorhombic LaFeO_3 (a), and transferred to second nearest neighboring octahedral Fe in cubic SrFeO_3 (b).

This indicates that after oxygen vacancy formation, the excess electrons generated by neutral oxygen vacancy formation remained localized to the oxygen vacancy adjacent area and formed a relatively small polaron, as shown in Figure 4.2(a). This charge localization can be simply explained by the electronic distribution on the oxygen-vacancy-adjacent Fe d -orbitals. According to crystal field theory, the Fe d -orbitals in the octahedral coordination found in the perfect LFO lattice split into $t_{2g}^3 e_g^2$, which can be further split into $b_{2g}^1 e_g^2 b_{1g}^1 a_{1g}^1$ due to Jahn-Teller distortions, as shown in Figure 4.3(a). All the Fe atoms in perfect LFO are in the 3+ high-spin state with each Fe containing five electrons in its $3d$ orbital ($[\text{Ar}] 3d^5$), indicated by the blue arrows in Figure 4.3(a). As a geometric consequence of losing a neighboring oxygen during oxygen vacancy formation, the two first-nearest-neighboring Fe atoms become SP coordinated, creating a different d orbital splitting situation of $e_g^2 b_{2g}^1 a_{1g}^1 b_{1g}^1$. To minimize the system energy, the two electrons produced during neutral oxygen vacancy formation are distributed to the lowest

energy level of *d*-orbitals of each Fe in the SP coordination. Hence, in LFO the excess (i.e. polaron) electrons remain localized and adjacent to the oxygen vacancy site. A schematic of the polaron (shown in yellow in Figure 4.2(a) and with a perspective view of oxygen vacancy adjacent lattice area in Figure 4.2(e)), show the resulting small LaFeO_{3-δ} polaron which is elongated along the Z direction with a length of ~4.0 Å.

4.2.2. SrFeO_{3-δ}

In cubic SFO, as discussed in Section 4.1 the electrons produced by a neutral oxygen vacancy formation do not remain localized on the first-nearest-neighboring Fe connected to the oxygen vacancy. The Fe in perfect SFO has an [Ar] 3d⁴ 4+ charge state, i.e., 4 electrons in the 3*d* orbitals, as indicated by the blue arrows in Figure 4.3(b). After oxygen vacancy formation, the excess electrons generated due to oxygen vacancy formation (i.e. the red arrows in Figure 4.3(b)) transfer to a_{1g} level in the Oh-Fe atoms instead of a higher energy b_{1g} of the nearest-neighbor, SP-coordinated Fe ions. Further, since there are eight second-nearest neighboring Oh-Fe present with the same a_{1g} energy level around each oxygen vacancy site, the excess electrons are distributed between these eight Fe atoms to produce the “pancake” shaped polaron shown in Figures 4.1(d) and 4.1(h) with an estimated polaron diameter and height of ~7.8 and ~3.9 Å, respectively.

Figure 4.4(a) shows that the oxygen vacancy polaronic distribution in tetragonal SFO structure resembles the polaron shape in cubic SFO (Figure 4.2(h)). Here, the formation of an oxygen vacancy pushes the excess electrons to the second nearest neighboring octahedral (Oh) Fe rather than localizing it to the oxygen vacancy adjacent square-pyramidal (SP) Fe. The charge on the oxygen-vacancy-adjacent SP-Fe remains ~4+ (a result obtained from a magnetic moment analysis) before and after oxygen vacancy formation. In contrast, the charge on the second nearest neighboring Oh-Fe atoms is reduced from 3.6+ to 3.3+ due to a gain in partial electrons. Due to

symmetry, the two electrons are shared between the eight second nearest neighbor Oh-Fe atoms and the shape of the polaron is denoted by the dashed purple line in Figure 4.4(a).

Unlike tetragonal SFO, the excess electrons left behind by neutral oxygen vacancy formation remain localized to the oxygen-vacancy-adjacent Fe atoms in orthorhombic and brownmillerite SFO. This occurs because, in orthorhombic SFO, oxygen vacancy generation occurs next to Fe^{4+} ions originally in square pyramidal coordination and transform to a square planar (SP) coordination with oxygen vacancy formation (as shown in Figure 4.4(b)). Since a Figure 4.5(a) SP $d_{x^2-y^2}$ electron would have a relatively high-energy state, after oxygen vacancy formation the five electrons in SP- Fe^{3+} adopt a low spin configuration after oxygen vacancy formation (with one electron each in the z^2 and xy states and three electrons shared between the yz and zx states). The orthorhombic to brownmillerite phase transition is brought about by the need to accommodate the electrons generated by oxygen vacancy formation. Because the second-nearest neighbor Fe atoms in orthorhombic SFO are octahedrally coordinated and have 5 electrons (each one occupying one of the electron states in Figure 4.5(b)) it is not energetically favorable for the electrons formed by oxygen vacancy formation to be transferred to the second nearest neighbors. Further, since localization of these extra electrons on the nearest SP-Fe would significantly increase the energy of the system, the FeO_4 SP coordination undergoes a structural transformation to tetrahedral (Td) coordination (with a comparatively lower energy state for 5 unpaired d-orbital electrons, as shown in Figure 4.5(c)), in the process causing the orthorhombic to brownmillerite phase transition.

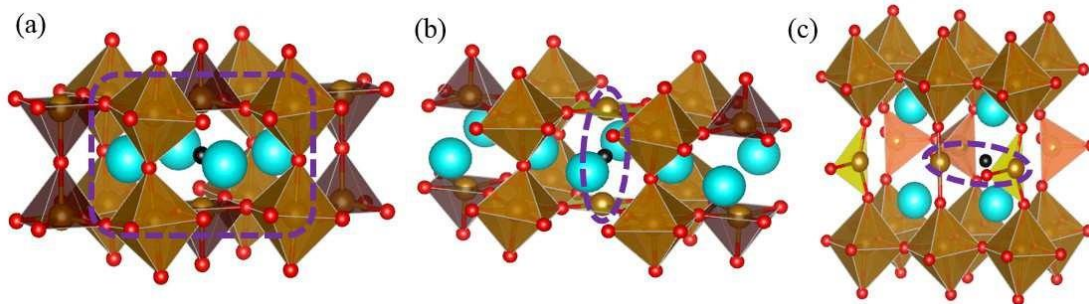


Figure 4.4. Oxygen vacancy polaron shape in (a) tetragonal, (b) orthorhombic, (c) brownmillerite $\text{SrFeO}_3.\delta$. Fe-O polyhedra colored according to the charge on Fe.²⁷ Here, blue atoms are Sr, brown are Fe and red are O.

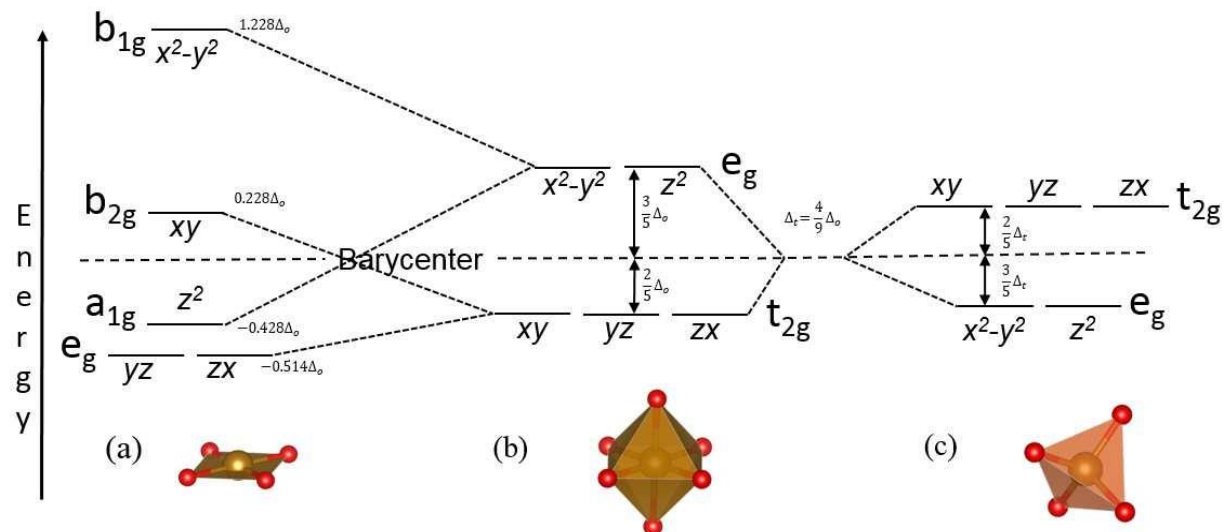


Figure 4.5. d-orbital splitting and energy distribution for different Fe-O polyhedra was derived from crystal field theory. (a) Square planar Fe-O coordination, (b) octahedral FeO coordination (c) tetrahedral Fe-O coordination.

For dilute oxygen vacancy formation ($\delta < 0.1$), the vacancy formation energies for cubic SFO, rhombohedral LSF55, and orthorhombic LFO are 0.4, 1.6, and 3.5 eV respectively. This ~ 3 eV variation shows that even in the dilute range the La/Sr ratio dramatically impacts the oxygen vacancy concentration. Furthermore, it is significant to note that maximum oxygen vacancy site fraction that can be achieved in SFO, LSF, and LFO within SOFC operating conditions is $\sim 10\%$ that occurs at 600°C in orthorhombic SFO.¹⁶⁰

4.2.3. Rhombohedral and Cubic $\text{La}_{0.5}\text{Sr}_{0.5}\text{FeO}_{3-\delta}$

In both stoichiometric rhombohedral and stoichiometric cubic LSF55, the computationally predicted charge state on Fe is 3.5+. This indicates that, on average, formally there are four and a half electrons in the Fe *d*-orbitals. One could imagine, as a combination of LFO and SFO, the excess electrons due to oxygen vacancy formation could, therefore, be distributed to both the first and second nearest neighboring Fe atoms and this is indeed the case, as shown in Figures 4.2(f) and 4.2(g).

In cubic LSF55, after oxygen vacancy formation all the Oh-Fe connected to the SP-Fe via two 180° Fe-O-Fe bonds bend to 160°. The charge on first and second nearest neighboring Fe atoms were 3.35+, suggesting that the electrons left behind by neutral oxygen vacancy formation were distributed to the first (two SP-Fe) and second (eight Oh-Fe) nearest neighboring Fe atoms to the oxygen vacancy. Thus, as shown in Figures 4.2(c) and 4.2(g), in cubic LSF55 the oxygen vacancy polaron exhibit a “pancake” shaped polaron with an average diameter and height of ~8.3 and ~4.0 Å, respectively.

In rhombohedral LSF55, the polaron size is smaller than that in cubic LSF55, due to larger Fe-O polyhedra tilt angle in the rhombohedral structure. The oxygen vacancy formation calculations showed that oxygen vacancy formation in the Sr-O₃ plane was energetically favorable, compared to oxygen vacancy formation in the La-O₃ plane, by ~0.1 eV. After oxygen vacancy formation, the two SP Fe charge changed to 3.6+ from 3.5+. In contrast, the four Oh-Fe connected with the tilted Fe-O-Fe bond shown in Figure 4.2(c) gained electrons and became 3.3+ from 3.5+. This difference is related to the Fe-O-Fe bond angle. Note there are four Oh-Fe connecting the four O atoms at the square bottom of the SP-Fe polyhedra, via a Fe-O-Fe bridge. In rhombohedral LSF55, two of the Fe-O-Fe bond angles are ~170° (compared to 180° in the cubic structure) and

the other two Fe-O-Fe bond angles are $\sim 153^\circ$ (i.e they are more bent). Since a more bent bond angle results in more Jahn-Teller distortions, the split e_g energy level in the more tilted Oh will be at a lower energy state and the excess electrons generated by oxygen vacancy formation will preferably transfer to the more titled Oh-Fe atoms, as shown in Figures 4.2(c) and 4.2(g). In rhombohedral LSF55, these excess electrons produced a quarter of a “pancake” like polaron shape (Figure 4.2(f)). The polaron size was approximately one-fourth of that in cubic LSF55, with an average polaron radius and height of 4.3 and 4.0 Å, respectively.

As shown in Figure 4.2, the size of the polaron is the smallest in LFO and it increases with increasing Sr doping LSF. The small and more localized polaron in LFO can screen the charge of the oxygen vacancy more effectively, thus the oxygen vacancies will remain non-interacting and will not impact each other’s polaronic strain field until they are very close. However, the larger and more delocalized polarons can not screen the vacancy charge effectively, and thus the vacancies may start to interact, even at a large distance. Therefore, in the next section, the oxygen vacancy formation energy as a function of vacancy concentration was studied and correlated with the polaron size.

5. Oxygen Vacancy Formation sites and Formation Energy for Interacting and Non-interacting Vacancies at 0 K

In most of the LSF phases, multiple oxygen vacancy formation sites are available, observed from the symmetry. For vacancy formation calculation it is important to find all the possible vacancy formation sites and after that energetically favorable vacancy formation site which will give oxygen vacancy formation energy for that structure.

5.1. Oxygen Vacancy Formation Sites in $\text{SrFeO}_{3-\delta}$ Phases

The dashed red circles in Figure 1.1 identify the preferred oxygen vacancy generation sites, as determined by comparing the Table 5.1 oxygen vacancy formation energies for the various oxygen sites within each crystal structure. Figure 1.1(a) shows that in a perfect cubic SrFeO_3 , all of the oxygen atoms are situated at the corners of symmetrical Fe-O octahedra, 1.94 Å from the central Fe ion, and shared between two neighboring octahedra (here the designation Oh is used to denote an octahedron, while the oxygen site at the corner of two neighboring octahedra is denoted as Oh-Oh). The high order of geometric symmetry (point group: O_h) and the single Fe^{4+} oxidation state ensures that only one type of oxygen site (denoted O1) is present in cubic SrFeO_3 . Also, according to Mössbauer spectroscopic study, the charge on Fe in cubic SrFeO_3 does not show a charge disproportionation reaction, like what happens in CaFeO_3 (where $\text{Fe}^{4+} \rightarrow \text{Fe}^{3+} + \text{Fe}^{5+}$).¹⁶¹ When an oxygen atom leaves the Oh-Oh site in cubic SrFeO_3 , an oxygen vacancy is formed and the two neighboring Oh-Oh polyhedra collapse into two square pyramidal (SP) polyhedra. Curiously, for reasons described in Section 3.3.4, the two iron atoms bordering this oxygen vacancy (the ones now in SP coordination) remain as Fe^{4+} .

In contrast, Figure 1.1(b) shows that in perfect tetragonal $\text{SrFeO}_{2.875}$ both octahedral (Oh) and square pyramidal (SP) polyhedra are present. Charge interpretation based on the magnetic

moment of iron indicates that the SP coordinated iron is Fe^{4+} while the Oh coordinated iron is either $\text{Fe}^{3.6+}$ (denoted as Oh1) or $\text{Fe}^{3.9+}$ (denoted as Oh2). The Oh1 octahedra are deformed and tilted (producing a Fe-O-Fe bond angle of 168.67° between two Oh1 octahedra) while there is no tilt between two Oh2 octahedra (producing a Fe-O-Fe bond angle of 180° , just as in the cubic SrFeO_3 structure). As shown in Table 5.1, the most favorable oxygen vacancy formation site in tetragonal $\text{SrFeO}_{2.875}$ (denoted as the O6 or Oh2-Oh2 site) is at the corner shared by two Oh2 octahedra.

Table 5.1. The vacancy formation energies at different oxygen site calculated for all four crystalline structures. Each site is noted by its label in Figure 1.1, its position in Fe-O polyhedra, and the charge of the Fe ions in the Fe-O polyhedra. The bold values indicate the most favorable oxygen vacancy site.

Compound	Label of O in Figure 1.1	Position in Fe-O Polyhedra	The charge state of Fe	ΔE_{vac} (eV)
SrFeO_3 (cubic)	O1	Oh-Oh	+4 --- +4	0.71
	O2	Oh1-Oh2	+3.6 --- +3.9	1.06
	O3	Oh1-SP	+3.6 --- +4	1.05
	O4	Oh1-Oh1	+3.6 --- +3.6	1.14
	O5	SP-SP	+4 --- +4	1.15
	O6	Oh2-Oh2	+3.9 --- +3.9	0.92
$\text{SrFeO}_{2.75}$ (orthorhombic)	O7	Oh-SP	+3.3 --- +3.9	2.07
	O8	Oh-Oh	+3.3 --- +3.3	2.12
	O9	SP-SP	+3.9 --- +3.9	1.25
$\text{SrFeO}_{2.5}$ (brownmillerite)	O10	Oh-Oh	+3 --- +3	3.44
	O11	Oh-Td	+3 --- +3.2	3.28
	O12	Td-Td	+3.2 --- +3.2	3.00

Figure 1.1(c) shows that in the perfect orthorhombic $\text{SrFeO}_{2.75}$ structure only a single type of Oh polyhedron (all containing a $\text{Fe}^{3.3+}$ ion) and a single type of SP polyhedron (all containing a $\text{Fe}^{3.9+}$ ion) are present. These results clearly show that this structure is not made up of iron atoms that are distinctly 3+ or 4+ in charge, as has been postulated using the concept of formal charge,³² but instead made up of iron atoms with fractional oxidation states interpreted from the calculated

magnetic moment. This results from internal redox reactions with the neighboring oxygen atoms that result in informal charges on the oxygen atoms.¹⁶² Comparing Figure 1.1(b) and 1.1(c), the orthorhombic strontium ferrite can be considered as tetragonal strontium ferrite which has lost one oxygen from the Oh₂-Oh₂ site and where the two neighboring Oh₂-Oh₂ polyhedra have collapsed into two SP polyhedra. The two iron atoms in these SP polyhedra remain ~4+, while the iron atoms in the neighboring Oh sites reduce their charge to 3.3+ with the transformation from tetragonal to orthorhombic SrFeO_{2.75}. In the orthorhombic structure, all of the Oh polyhedra are deformed and tilted (producing a Fe-O-Fe bond angle of 165.22° between two Oh polyhedra). As shown in Table 5.1, the most favorable oxygen vacancy formation site in orthorhombic SrFeO_{2.75} is at the shared corner of two SP polyhedra.

Figure 1.1(d) shows that in the brownmillerite SrFeO_{2.5} structure both Oh and tetrahedral (Td) Fe-O coordination is present. Although some literature sources have claimed that all Fe ions in SrFeO_{2.5} carry a formal charge state of Fe³⁺ in SrFeO_{2.5},³² the analysis here indicates that Td Fe has a magnetic moment of 4.11 μ_B and a charge of 3.2+, while the Oh Fe has a magnetic moment of 4.22 μ_B and a charge of 3+. This agrees with experimentally measured Mössbauer data indicating that the magnetic moment of Oh Fe is slightly higher than that on Td Fe.¹⁴⁸ As shown in Table 5.1, the most favorable oxygen vacancy formation site in brownmillerite SrFeO_{2.5} is at the shared corner of two Td polyhedra (at O12).

The charge disproportionation of Fe in oxygen deficient SrFeO_{3-δ} phases (Figure 1.1) is accompanied by gradual loss of occupied states near the Fermi level (Figure 3.2), causing a reduction in the electronic conductivity. This phenomenon has been reported by Hirai *et al.* during charge disproportion induced phase transformation in tetragonal SrFeO_{3-δ} at 70 K.¹⁶³ As demonstrated in Table 5.1, in each of the strontium ferrite structures modeled here, oxygen atoms

bonded to the highest charged Fe atoms in polyhedra are always the most favorable locations for oxygen vacancy formation.

5.2. Oxygen Vacancy Formation Energies in $\text{SrFeO}_{3-\delta}$ Phases

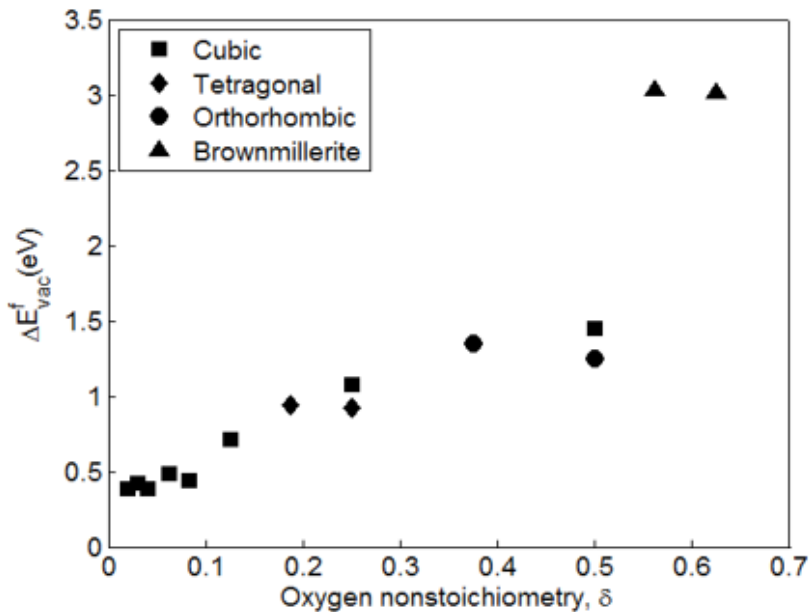


Figure 5.1. The vacancy formation energy per oxygen vacancy, calculated from DFT for four different $\text{SrFeO}_{3-\delta}$ phases.

Figure 5.1 shows the oxygen vacancy formation energy (ΔE_{vac}^f) calculated using Equation 2.1 (on a per vacancy basis) for cubic, tetragonal, orthorhombic, and brownmillerite strontium ferrite as a function of oxygen nonstoichiometry (plotted in terms of the absolute non-stoichiometry, \square). For these calculations, only the site with the lowest oxygen vacancy formation energy in each phase identified in Table 5.1 was utilized. It is important to note that the trends observed here should also hold at high temperature since Equation 2.4 indicates that oxygen's temperature and pressure effects will shift the formation energy in each phase by the same amount. Figure 5.1 reveals that the 0 K oxygen vacancy formation energy increases with each phase transition. This is because, as discussed in Section 4.1, oxygen vacancy formation is always the easiest next to the iron with

higher oxidation state, which decreases in quantity with each new structure. It is important to note that the vacancy formation energy in cubic $\text{SrFeO}_{3-\delta}$ is a very low 0.4 eV, which explains why the material has such a high oxygen vacancy concentration at room temperature in air and why it has been difficult to produce stoichiometric cubic SrFeO_3 .^{32,44} Figure 5.1 also shows that the oxygen vacancy formation energy in cubic $\text{SrFeO}_{3-\square}$ exhibits a constant low value (~ 0.4 eV) for $\delta < 0.05$; increases to ~ 0.5 eV for $0.05 < \delta < 0.1$; and quickly increases with concentration when $\delta > \sim 0.1$. The increase in oxygen vacancy formation energy with increasing oxygen non-stoichiometry is due to oxygen vacancy interactions. A similar trend due to oxygen vacancy interactions was also reported by Kuklja *et al.*²⁹ in their computational work on cubic and hexagonal $\text{Ba}_x\text{Sr}_{1-x}\text{Co}_y\text{Fe}_{1-y}\text{O}_{3-\delta}$. None of the other $\text{SrFeO}_{3-\square}$ phases (tetragonal, orthorhombic and brownmillerite $\text{SrFeO}_{3-\square}$) exhibits a significant dependence of the oxygen vacancy formation energy on the oxygen vacancy concentration. The concentration dependent oxygen vacancy formation energy in cubic $\text{SrFeO}_{3-\square}$ indicates oxygen vacancies start to interact around $\delta \sim 0.05$, when the average distance between oxygen vacancies are ~ 11 Å, and the interaction becomes stronger when $\delta > 0.1$ as the average oxygen vacancy distance decreases to ~ 8 Å. This average distance between neighboring oxygen vacancies is more than 4 times larger than the Fe-O bond distance (1.94 Å).

5.3. Computationally Predicted Vacancy Ordered Phase Transition in $\text{SrFeO}_{3-\delta}$ Phases

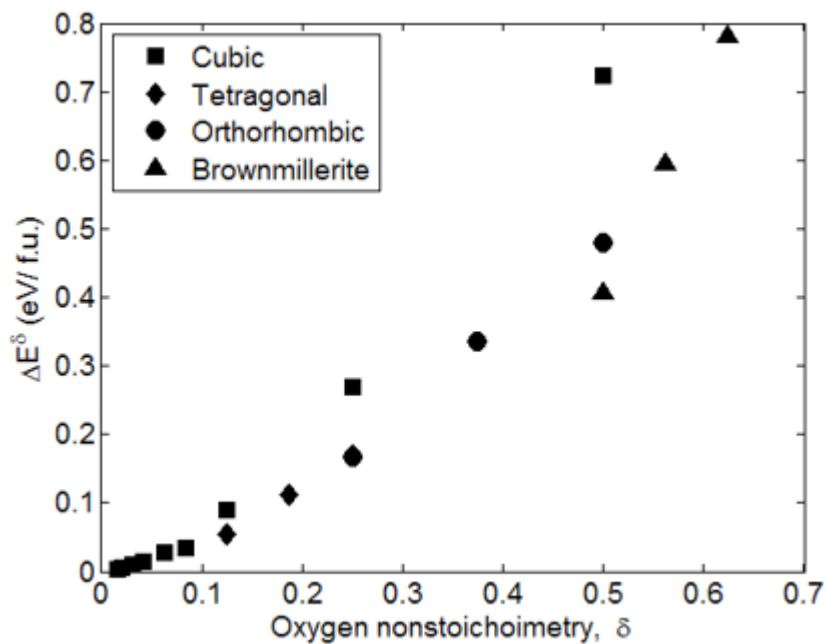


Figure 5.2. Energy required (ΔE^δ) to form the non-stoichiometric structures ($\text{SrFeO}_{3-\delta} + \frac{\delta}{2}\text{O}_2$) from cubic SrFeO_3 .

Experimentally, with increasing T and the increasing δ accompanying it, strontium ferrite displays several phase transitions as it progresses from cubic SrFeO_3 to tetragonal $\text{SrFeO}_{2.875}$ (with $\delta^0=0.125$), to orthorhombic $\text{SrFeO}_{2.75}$ (with $\delta^0=0.25$), and finally to brownmillerite $\text{SrFeO}_{2.5}$ (with $\delta^0=0.5$). However, it has not been clear if these phase changes are induced by T or by δ . Thankfully, DFT calculations such as those in Figure 5.2 where the X for any structure can be arbitrarily increased as long as δ is $> \delta^0$ for the structure of interest (including those not observed in nature because of a phase transformation to a lower energy crystal structure) allow the effects of oxygen non-stoichiometry alone to be examined. Specifically, Figure 5.2 shows that at 0 K cubic strontium ferrite has the lowest energy from $0 < \delta < 0.125$, tetragonal strontium ferrite has the lowest energy from $0.125 < \delta < 0.25$, tetragonal and orthorhombic strontium ferrite have similar energies from $0.25 < \delta < 0.50$, and brownmillerite has the lowest energy for $\delta > 0.50$. This suggests that oxygen

non-stoichiometry instead of temperature is the dominant force driving the strontium ferrite phase transformations observed from 0–1400 °C in air. Further, these DFT calculations indicate that the enthalpy gain in the cubic to tetragonal or orthorhombic to brownmillerite phase transitions are larger than the configurational entropy contributions.

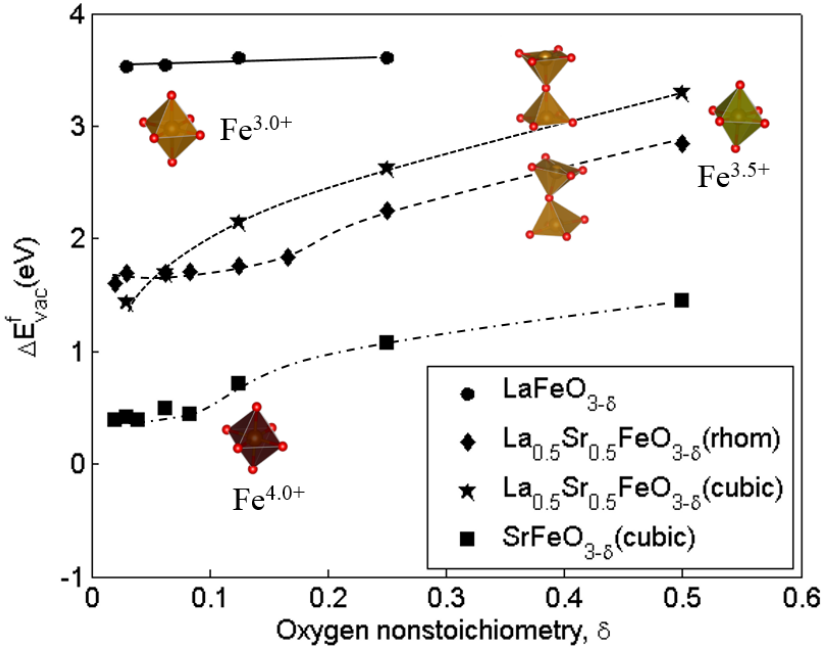


Figure 5.3. GGA+U calculated oxygen vacancy formation energies for different $\text{La}_x\text{Sr}_{1-x}\text{FeO}_3$ compositions. The Fe–O polyhedra represent the charge on Fe in a perfect lattice. The lines are guides to the eye.

In Figure 5.3, the DFT+U calculated oxygen vacancy formation energies for various LSF phases are plotted versus increasing oxygen nonstoichiometry per formula unit (i.e. δ). Vacancy formation energies of cubic SFO replotted from Figure 5.1 for comparison purpose. The vacancy formation energies in LFO remained constant at 3.57 ± 0.04 eV and did not show any significant interaction even at high oxygen nonstoichiometry (i.e. at $\delta = 0.25$). This is consistent with the small and localized vacancy LFO polaron that allows the oxygen vacancies to be very close without interacting (and hence treated as dilute).

Figure 5.3 also shows that rhombohedral LSF55, which as shown in Figure 4.2 has tilted Fe-O polyhedra and a small polaron size compared to the untilted Fe-O polyhedra and large polaron sizes found in cubic LSF55, exhibits a lower oxygen vacancy formation energy and less oxygen vacancy interactions than cubic LSF55. The vacancy formation energy in rhombohedral LSF55 remained constant at \sim 1.7 eV for $\delta \leq 0.25$ until the polarons began to overlap at an average distance between oxygen vacancies of \sim 7 Å, larger than the polaron size due to its irregular shape. In contrast, cubic LSF55 showed an increasing trend even for $\delta < 0.1$, due to its much larger polaron size. Note, in cubic LSF55 it was not computationally possible to find a dilute limit for oxygen vacancy formation. This is because the atomic position relaxation of the cubic LSF55 supercell with very low oxygen non-stoichiometry ($\delta = 0.03$) resulted in increased octahedral tilt around each oxygen vacancy site producing a locally rhombohedral LSF55 structure. This resulted in the calculated cubic LSF55 oxygen vacancy formation energy that was less than that found in rhombohedral LSF55 (1.4 eV vs. 1.7 eV) at very low oxygen non-stoichiometry. This suggests that cubic LSF55 may only exist at higher δ and/or temperature values far from the rhombohedral to cubic LSF phase boundary.

Overall, the oxygen vacancy formation energies in rhombohedral and cubic LSF55 suggest that smaller polaron size leads to weaker interaction among oxygen vacancies. Further, the observed trends with La:Sr ratio indicate that progressively larger polaron sizes result in increasing oxygen vacancy formation energies with increasing Sr or δ . This behavior is consistent with experimental results showing that Sr-rich LSF and highly oxygen deficient compositions are more prone to oxygen-vacancy-ordering-induced phase transformations, while Sr-poor and oxygen rich LSF compositions are not.⁶³

In addition, the crystal-field-theory based polaron size estimation technique presented here can be applied to other perovskite structures. For example, LaMnO₃ has a structure similar to LaFeO₃, which shows almost no oxygen vacancy interactions. However, Mn³⁺ has the same number of d-electrons as Fe⁴⁺ (i.e. both have an electron configuration of [Ar] 3d⁴). Therefore, the excess electrons generated by oxygen vacancy formation should be distributed to the O²⁻-coordinated Fe, and thus the long-range charge transfer observed in SrFeO₃ should also occur in LaMnO₃ and result in a large oxygen vacancy polaron size that leads to strong vacancy interactions that cause the increasing vacancy formation energy with \square , as reported by Lee *et al.*²⁸

6. Oxygen Vacancy Site Fraction as a Function of Temperature and Phase Change (in air)

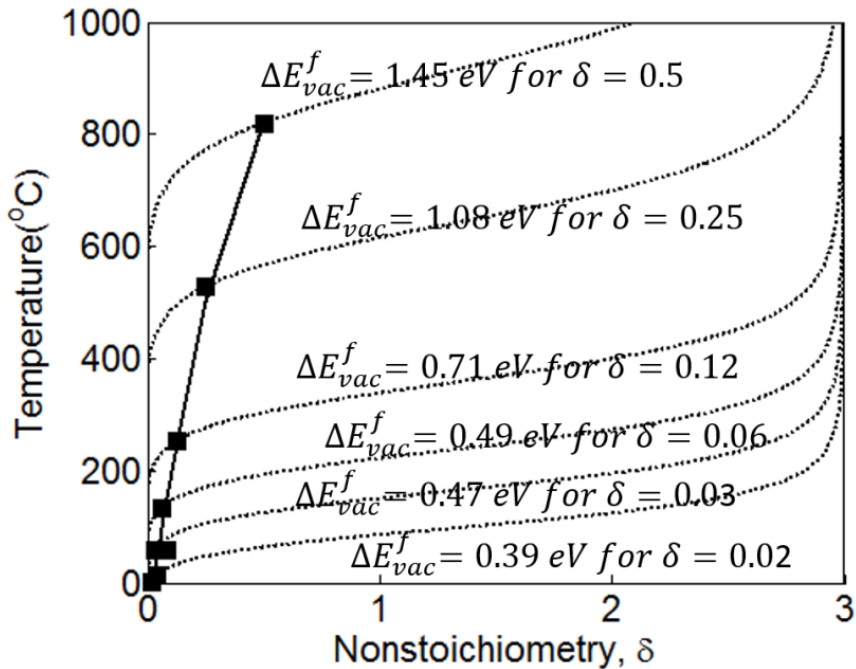


Figure 6.1. Dotted line represent δ increasing with T at $pO_2 = 0.21$ atm according to Equation 1.6 (dilute vacancy assumption) for cubic $SrFeO_{3-\delta}$ (ΔE_{vac}^f from Figure 5.1 for different δ). Solid line represent δ increasing with T at atmospheric condition according to Equation 2.17 (interacting vacancy assumption) for cubic $SrFeO_{3-\delta}$ (where ΔE_{vac}^f is a function of δ).

It is important to correctly account for the concentration dependence of the oxygen vacancy formation energy when calculating the equilibrium oxygen non-stoichiometry. Specifically, Figure 6.1 shows that using the dilute model and assuming concentration independent oxygen vacancy formation energy values for cubic $SrFeO_{3-\delta}$ (the dashed lines) to predict oxygen non-stoichiometry values (i.e. following Equation 1.6 or 2.16) leads to results that are wildly different from experimentally observed values and sometimes unphysical. For instance, assuming $\Delta E_{vac} = 0.4$ eV for cubic $SrFeO_{3-\delta}$ (the smallest value calculated in Figure 5.1) results in a $\delta \leq 0.02$ at $0^\circ C$ that quickly rises to ~ 3 at $300^\circ C$ after applying the thermodynamic connection energy of T at $p_{O_2} = 0.21$ atm. This result is unphysical because a $\delta=3$ would indicate that cubic strontium ferrite would

be completely reduced to its constituent metals at 300°C, despite the fact that strontium ferrite is stable to well above 800°C.^{44,158} Similarly, assuming a concentration independent cubic strontium ferrite oxygen vacancy formation energy of $\Delta E_{vac} = 1.45$ eV (the largest value calculated for cubic SrFeO_{3- δ} in Figure 5.1) and the necessary thermodynamic connection energy predict that cubic strontium ferrite is stable at high temperature, and that the predicted oxygen non-stoichiometry at 25°C in air is many orders of magnitude below experimental value.⁴⁴ It is important to note that when oxygen vacancies interact, their formation energy increases with the site fraction X (especially in cubic phase). Therefore $\Delta G_{vac}^f(T, p, X)$ depends on temperature, oxygen partial pressure, and the vacancy site fraction, as demonstrated in Figure 6.2 and in previous studies.^{24,164}

6.1. Oxygen Vacancy Site Fractions in Different SrFeO_{3- δ} Phases Predicted with Temperature in Air

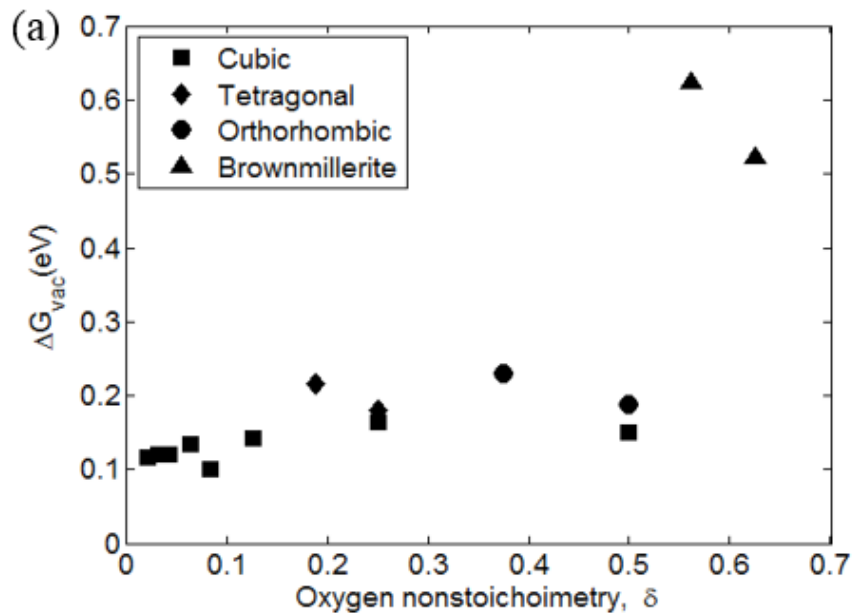
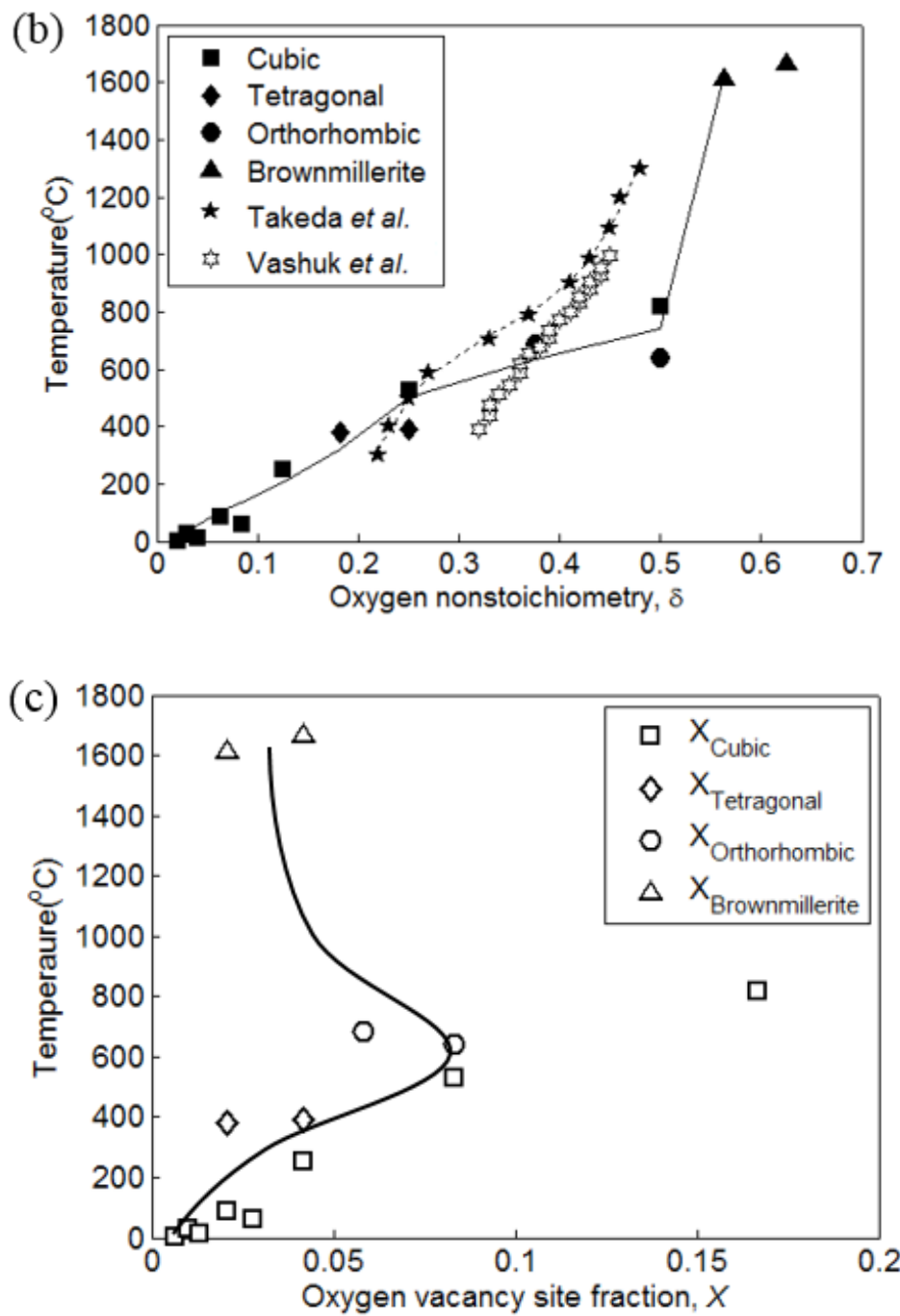


Figure 6.2. (a) Vacancy formation free energy with nonstoichiometry for all the phases (b) Nonstoichiometry is plotted as a function of temperature. (c) Vacancy formation site fraction is plotted as a function of temperature. (the data point corresponding to $3X_{cubic} = 0.5$ is neglected from fitting as at this vacancy site fraction cubic SrFeO_{3- δ} is easily transformed to brownmillerite and hence loses its available vacancy sites).

Figure 6.2 (cont'd)



It is therefore important to apply the non-dilute model and solve Equation 2.17 to calculate the oxygen vacancy site fraction X . The solid line in Figure 6.1 shows that much more realistic oxygen

non-stoichiometry values can be obtained using the full range of concentration-dependent ΔE_{vac}^f values obtained in Figure 5.1 using Equation 2.17.

Figure 6.2(a) shows the full range of temperature and oxygen partial pressure corrected concentration-dependent free energy of oxygen vacancy formation, $\Delta G_{vac}^f(T, p, X)$, calculated via Equation 2.4 for the various strontium ferrite phases as a function of oxygen non-stoichiometry. Although only modest increases in ΔG_{vac}^f occur with δ for $\delta < 0.5$, the ΔG_{vac}^f jumps dramatically once the brownmillerite phase forms.

Based on the solution of Equation 2.17, a unique relationship between X and T can be obtained for each phase, so \square and T relationship can be obtained in a broad temperature as well. Figure 6.2(b) compares the experimentally measured and our predicted oxygen non-stoichiometry of strontium ferrites (a trend line is added as the moving average) from 300-1300°C in the air. The computationally predicted oxygen non-stoichiometry vs. temperature is similar to the experimentally measured values of both Takeda *et al.*⁴⁴ and Vashuk *et al.*⁵⁷ Such agreement demonstrates that the DFT+U predicted oxygen vacancy formation sites and activation energies reported here are correct and it is important to account for the concentration dependent vacancy formation energy in predicting vacancy concentrations. That said, some deviation between the computationally-predicted and experimentally-measured oxygen non-stoichiometry exists. This deviation may result from multiple phases can coexist within several oxygen non-stoichiometry windows.⁴⁴

Lastly, Figure 6.2(c) shows the strontium ferrite oxygen vacancy site fraction as a function of temperature. Interestingly, the oxygen vacancy site fraction (which together with the charge and oxygen vacancy diffusivity determines the oxygen vacancy concentration important to so many

MIEC applications) peaks around 600°C then declines at higher temperatures due to the much larger oxygen vacancy formation energy in the brownmillerite structure compared to the cubic, tetragonal, and orthorhombic structures (Figure 5.1). As will be explored in a future publication,¹⁶⁵ since the cubic structure shows the lowest oxygen vacancy formation energy but suffers from strong vacancy interactions caused by the long-range electron transfer, it is reasonable to suggest that dopants (such as La on the Sr site as occurs in the commonly used SOFC material $\text{La}_{0.6}\text{Sr}_{0.4}\text{FeO}_{3-\delta}$)⁶ that can localize electrons around an oxygen vacancy may reduce the interaction between oxygen vacancies and eliminate vacancy ordering, allowing for cubic $\text{SrFeO}_{3-\square}$ with high ionic conductivity. This possibility will be explored in a future paper.

6.2. Oxygen Vacancy Site Fractions in Different LSF Compositions Predicted with Temperature in Air

Figure 6.3 shows the oxygen vacancy site fraction as a function of temperature and partial pressure of oxygen ($p_{\text{O}_2} = 0.21 \text{ atm}$) for three different LSF compositions calculated using the non-dilute oxygen vacancy site fraction calculation method of Equation 6. This method was developed and used for SFO to predict the \square and X as a function of temperature in SFO in the air, and (considering phase changes in the material) the predicted trends compared well with the experimental TGA data.

Figure 6.3(a) compares the calculated oxygen vacancy non-stoichiometry, δ , in rhombohedral and cubic LSF55 structures with experimentally measured data¹¹ and shows reasonably good agreement at SOFC operating temperatures (600 °C ~1200 °C). The experimental data in Figure 6.3(a) also shows that for LSF55 the slope of the \square vs temperature relation decreases with increasing temperature. This is caused by rhombohedral to cubic phase

transformation at high temperature⁶⁵ and the stronger oxygen vacancy interactions in cubic LSF55 than in rhombohedral LSF55 at low temperature.

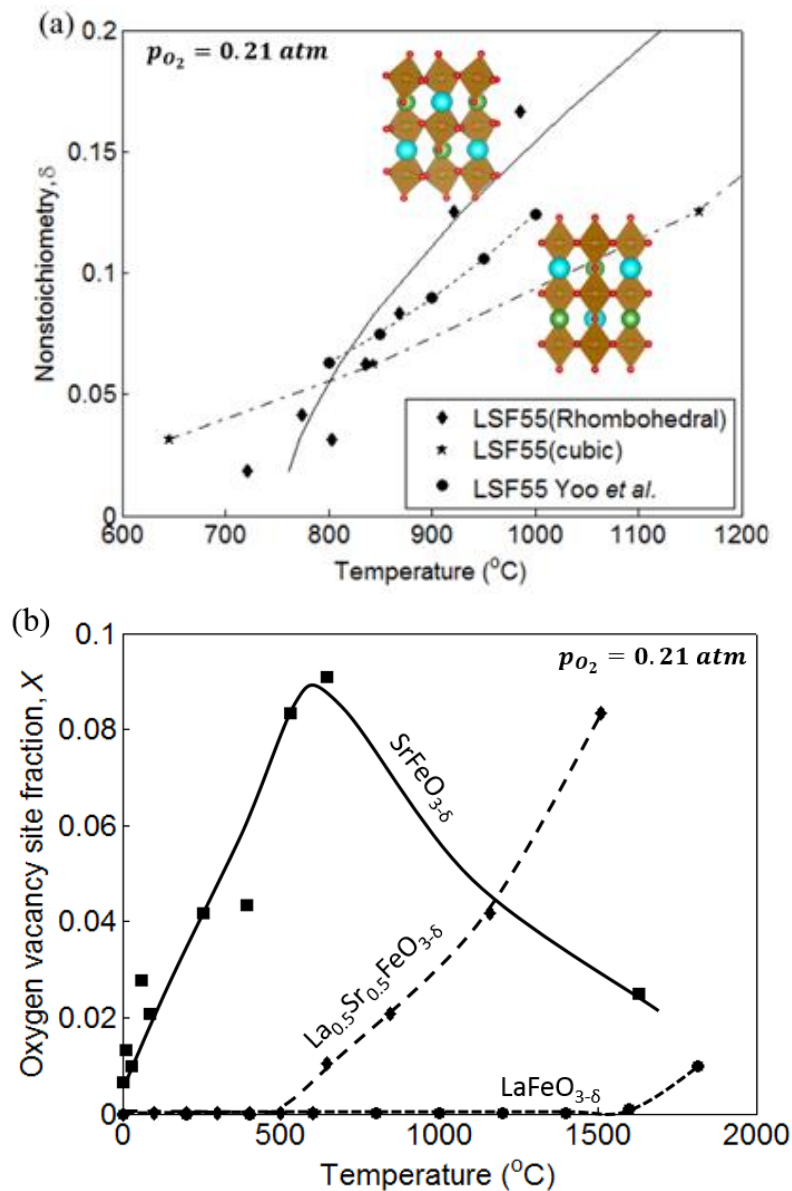
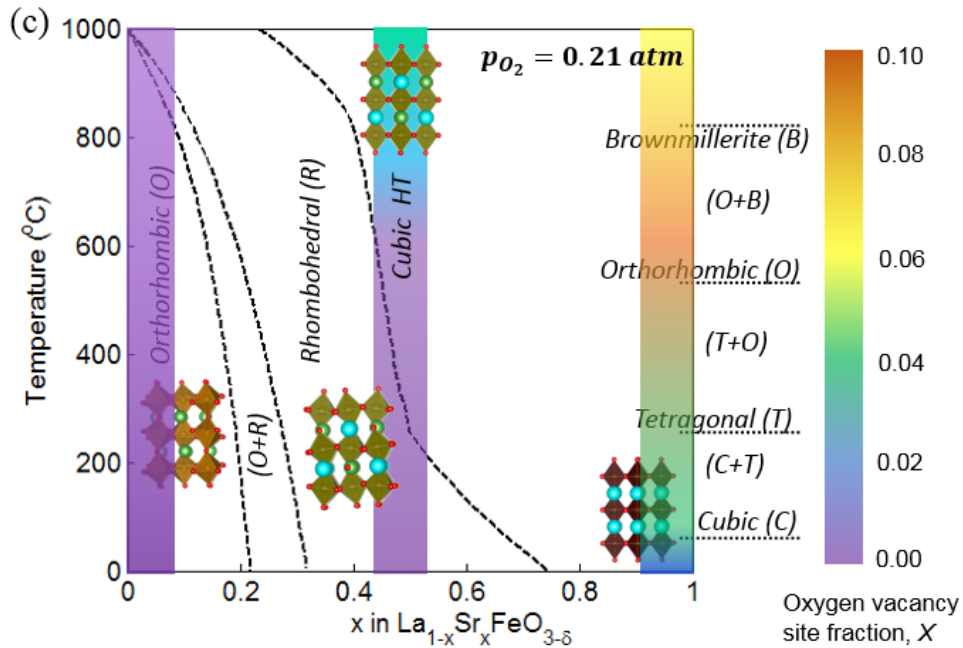


Figure 6.3. (a) The oxygen non-stoichiometry versus temperature in air, (b) the oxygen vacancy site fraction as a function of temperature in air, and (c) the oxygen vacancy site fraction as a function of temperature and La/Sr ratio for various $\text{La}_x\text{Sr}_{1-x}\text{FeO}_3$ phases. Note, the lines in (a-b) and (c) are guides to the eye and the lines in (c) are the experimentally determined phase boundaries.^{44,65} The oxygen vacancy site fraction in (c) is denoted by the color overlay and the right-hand color scale. The X values in b) and c) are never zero. They are just smaller than can be resolved with the linear X scale chosen to highlight the X trends discussed here.

Figure 6.3 (cont'd)



As discussed previously, rhombohedral LSF55 generally has a lower oxygen vacancy formation energy, and therefore Figure 6.3(a) shows a higher $\square \square$ for rhombohedral LSF than for cubic LSF at similar temperatures. The rhombohedral to cubic LSF phase transformation temperature increases with higher La:Sr ratio, as shown in the experimentally overlaid phase diagrams of Figure 6.3(c). For example, the phase transition temperature occurs at $\sim 450^{\circ}\text{C}$ for LSF55 but is increased to 800°C for $\text{La}_{0.6}\text{Sr}_{0.4}\text{FeO}_{3-\delta}$ (LSF64). Hence, it is beneficial to adjust the La:Sr ratio so that a highly oxygen deficient rhombohedral LSF, instead of cubic LSF, is formed. This likely contributes to the high performance of $\text{La}_{0.6}\text{Sr}_{0.4}\text{FeO}_{3-\delta}$ (LSF64) at traditional 800°C SOFC operation, as LSF64 retains the rhombohedral phase at 800°C according to the experimental phase diagram,

Considering the various phase transitions occurring in LSF, the oxygen vacancy site fraction, X , was computed for the specific phase occurring at that temperature according to the experimental phase diagrams from Fossdal *et al.*,⁶⁵ and Takeda *et al.*⁴⁴ The computed X values for LFO, SFO,

and LSF55 are plotted in Figure 6.3(b). Figure 6.3(b) shows that due to the oxygen vacancy formation energies are shown in Figure 5.3 and those calculated for other phases, increasing La:Sr ratio tends to result in a lower X at a given temperature. In LFO, there were almost no oxygen vacancy sites till 1000°C. In contrast, SFO is highly oxygen deficient SFO but experiences a reduction in X with increasing temperature due to oxygen vacancy ordering once brownmillerite is formed. Figure 6.3(b) also shows that the X in orthorhombic $\text{SrFeO}_{3-\square}$, is larger than in LSF55 at ~600°C. Additional studies on the oxygen ion conductivity are performed to determine if this results in a higher (~600°C) SFO ionic conductivity than LSF55 and reported in Chapter 7.^{31,160}

6.3. Effect of the Variation of U-Parameter on Oxygen Vacancy Formation

The qualitative trends in oxygen vacancy formation energy with vacancy concentration do not depend on the selection of U parameter, and that $U_{eff} = 3$ gives the best match to the measured oxygen nonstoichiometry. This is shown in Figure 6.4(b) where the oxygen vacancy formation energies for four different phases at different oxygen nonstoichiometries using $U_{eff} = 2, 3$, and 4 are shown. The solid black line shows the trend of oxygen vacancy formation energy with increasing oxygen nonstoichiometry at $U_{eff} = 3$ as presented in Figure 6.2(b). The dotted and dashed line showed results corresponding to $U_{eff} = 2$ and 4 respectively. It is important to note that oxygen vacancy formation energies calculated with $U_{eff} = 2$ overestimate the results for cubic and tetragonal phase by ~ 0.3 eV, whereas, calculations made with $U_{eff} = 4$ underestimates the results by ~ 0.3 eV. Further, the effect of a change in U parameter (from 2 to 3, or 3 to 4) on the calculated oxygen vacancy formation energies for orthorhombic and brownmillerite phases were insignificant (< 0.1 eV).

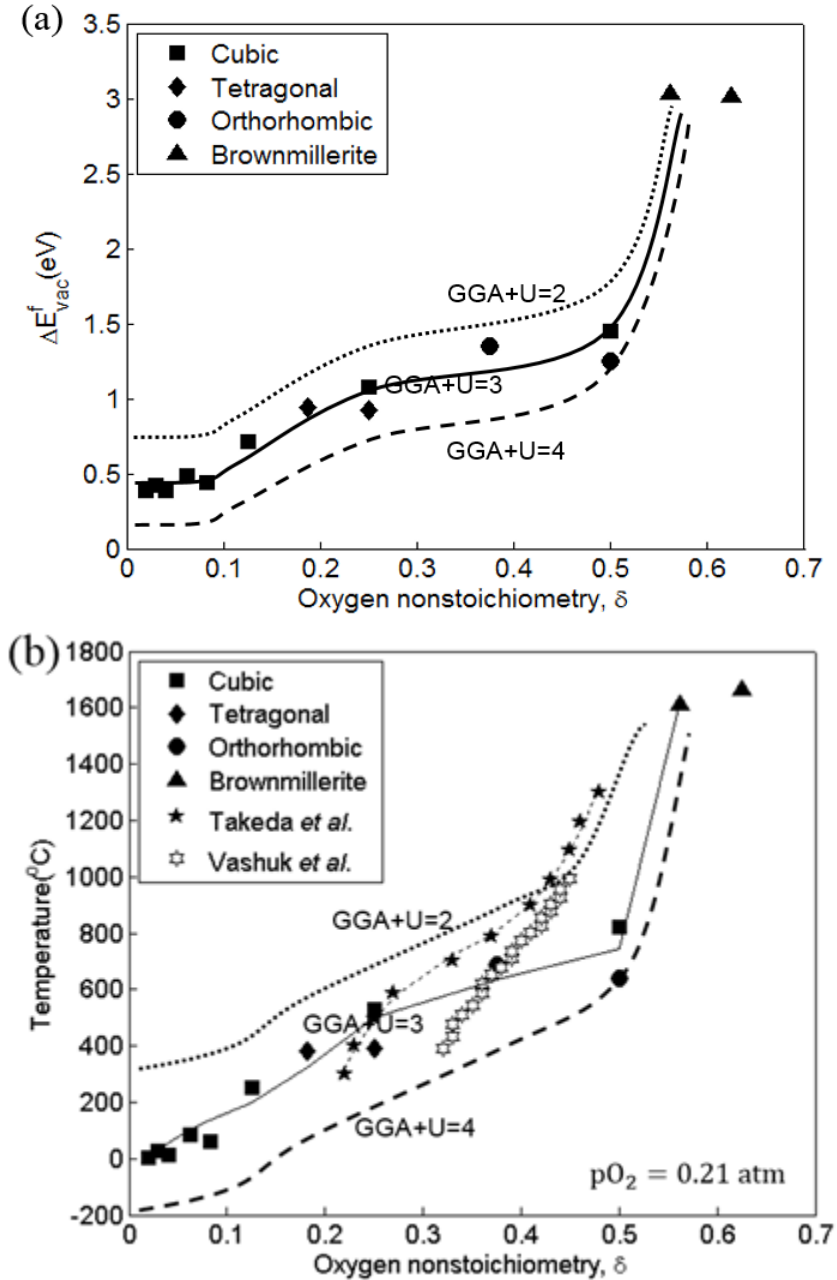


Figure 6.4. (a) Compare the impact of U parameters on oxygen vacancy formation energy as a function of oxygen nonstoichiometry; (b) compare the calculated oxygen nonstoichiometry as a function of temperature with different U parameters with experimental values.

The oxygen nonstoichiometry and temperature relation, $\delta(T)$ were also calculated with $U_{\text{eff}} = 2$ and $U_{\text{eff}} = 4$ and plotted in Figure 6.4(b) and compared with the results of $U_{\text{eff}} = 3$. At lower oxygen nonstoichiometries ($\delta = \sim 0 - 0.3$) they respectively overestimated and underestimated the

temperature, required to generate the experimentally reported δ , by $\sim 200^\circ\text{C}$. Overall, $U_{eff} = 3$ led to predicted $\delta(T)$ relationship more consistent with experimental data for $\text{SrFeO}_3\text{-}\delta$ phases, mainly due to it is suited for both Fe^{+3} and Fe^{+4} .

7. Oxygen Ionic Conductivity in $\text{La}_{1-x}\text{Sr}_x\text{FeO}_{3-\delta}$ – Considering Oxygen Vacancy Interaction and Phase Change

Oxygen vacancy concentration and diffusion in any perovskite is central to its ion conduction capability. The product of oxygen vacancy concentration, diffusivity, and charge on the oxygen ion gives the total ionic conductivity (Equation 1.1). Chapter 6 showed the oxygen vacancy concentration as a function of La/Sr ratio and temperature. Present chapter will focus on how diffusivity and ionic conductivity vary with La/Sr ratio and try to locate the composition with the maximum ionic conductivity at SOFC operating conditions. Patrakeev *et al.*⁶² have shown LSF55 possesses the highest oxygen ionic conductivity within LSF family at 950°C in the air in their experimental study. Whereas, most of the previous experimental studies to improve ionic conductivity or oxygen surface exchange in LSF, were performed with a different composition, $\text{La}_{0.6}\text{Sr}_{0.4}\text{FeO}_{3-\delta}$ (LSF64).^{6,47,166–169} With this computational study on ionic conductivity we have explained the reason for the selection of LSF64 over LSF55.

Oxygen vacancy formation energy and oxygen migration barrier are the major controlling factors for oxygen vacancy concentration and diffusion respectively, while temperature and pressure kept constant. Computational study on the oxygen vacancy formation energy shows, it varies by ~3 eV with change in La/Sr ratio at the A site of ABO_3 -perovskite, LSF (Figure 5.3). Also, significant variation (~2.5 eV) was observed in oxygen vacancy formation energy due to phase change in LSF end member SFO (Figure 5.1). Whereas, previous experimental and computational studies on oxygen vacancy migration in LSF predicted that A-site doping has negligible effect on oxygen migration barrier in LSF.^{18,20,43,55} This was confirmed from the computational work of Mastrikov *et al.*⁵⁵ They mentioned in their paper, “In $(\text{La},\text{Sr})(\text{Mn},\text{Fe},\text{Co})\text{O}_3$.

δ perovskites, the oxygen vacancy diffusion coefficients were experimentally found to be almost independent of the cation composition, with a typical migration barrier of ≈ 0.8 eV⁷⁰. However, these earlier studies on oxygen migration barrier in LSF are not complete for a broader range of La/Sr ratio, phase change and/or varying non-stoichiometry in LSF.

In this Chapter we have computationally evaluated oxygen vacancy migration barrier in different LSF compositions and phases, then predicted oxygen ion diffusivity, mobility and ultimately oxygen ionic conductivity to understand the effect of oxygen vacancy concentration and diffusion barrier separately, on the oxygen ion conduction. Previously calculated oxygen vacancy site fraction data is used to calculate oxygen vacancy concentration as a function of temperature, in the air.

7.1 Oxygen Vacancy Migration in $\text{La}_{1-x}\text{Sr}_x\text{FeO}_{3-\delta}$

It was shown by Chroneos *et al.*¹⁷⁰ that oxygen ion/vacancy moves via a vacancy hopping mechanism in a perovskite, like LSF. Using the CINEB calculation method described in Section 2.3.3 oxygen ion migration barriers were calculated in different LSF phases. From the oxygen vacancy site fraction calculations shown in Figure 6.2 and 6.3 within SOFC operating temperature (in air), it can be noticed the oxygen vacancy concentration remains close to dilute in most phases, except high temperature cubic SFO and cubic LSF55.

Therefore, oxygen vacancy migration barrier was calculated at different representative concentrations in all phases including: orthorhombic LFO, rhombohedral LSF55, cubic LSF55, cubic SFO, tetragonal SFO, and orthorhombic SFO. Due to the extremely high oxygen vacancy

formation energy of ~3 eV in brownmillerite SFO, this material is of less interest for MIEC applications, and therefore its migration barrier calculations were not performed.

7.1.1 Oxygen Vacancy Migration in $\text{LaFeO}_{3-\delta}$

Figure 7.1(a) shows the oxygen migration pathway in LFO, highlighted with pink atoms. Lattice distortion shown in the figure corresponds to the transition state lattice distortion. Calculated migration barrier at two different δ ($= 0.06$ and 0.25), shown in Figure 7.1(b), possess the same migration energy barrier of 0.89 eV. This confirms that even at $\delta=0.25$, the vacancies do not interact in LFO, which agrees with our dilute vacancy concept in LFO, described in Section 4.2.1. This calculated oxygen vacancy migration barrier in LFO is comparable to experimentally observed oxygen migration barrier of 0.77 eV obtained via oxygen tracer diffusion⁴³ and 1.1 eV obtained in conductivity relaxation experiment.¹⁷¹ Figure 7.1(c) shows how the magnetic moment changes on the oxygen-vacancy-neighboring Fe atoms during oxygen vacancy migration. This calculation shows that magnetic moment interpreted oxidation state of the second nearest neighboring Fe remains constant at 3+ during oxygen vacancy migration.²⁷ This finding is consistent with the small polaron volume calculated earlier for this material. Further, it can be noticed that when an oxygen atom moved from $\zeta = 0$ to $\zeta = 1$, the Fe2 atom reduced its charge from 3+ to 2+, as it changes from the 2NN to the 1NN of the oxygen vacancy. The magnetic moment on Fe1, oxygen vacancy adjacent Fe, maintained same magnetic moment (corresponding to Fe^{2+}) before and after migration, while at the transition state it was reduced due to gain in electron but the oxidation state was beyond our scale of measurement, defined in Section 2.1.2.

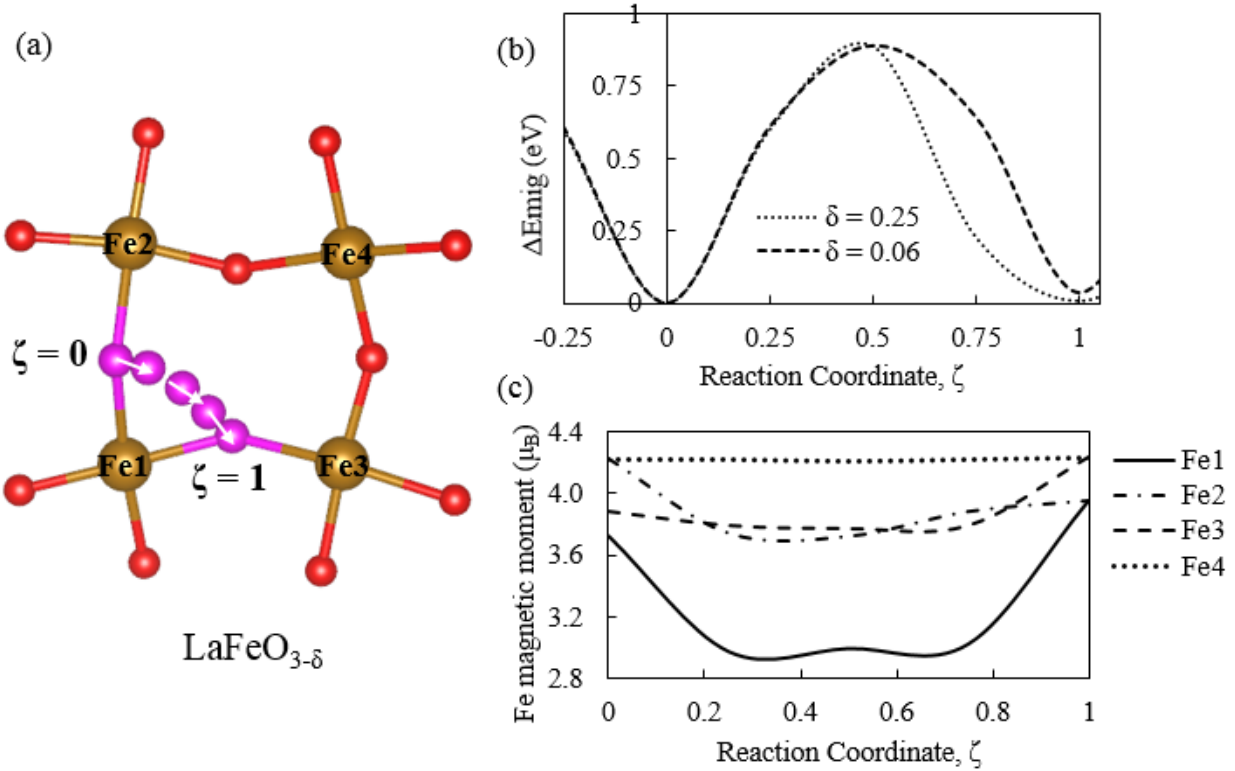


Figure 7.1. Oxygen migration in $\text{LaFeO}_{3-\delta}$. The pink atoms in (a) highlight the oxygen migration path, (b) shows the oxygen migration barrier along this path for two different δ , and (c) shows the charge change on the neighboring Fe atoms as a function of oxygen atom coordinate on its path (at $\delta = 0.06$).

7.1.2 Oxygen Vacancy Migration in $\text{La}_{0.5}\text{Sr}_{0.5}\text{FeO}_{3-\delta}$

Figure 7.2(a) and (b) show the oxygen migration path in rhombohedral and cubic LSF55 respectively. The calculated oxygen migration barriers are shown in Figure 7.2(c), for rhombohedral and cubic LSF55. The calculated migration barrier in rhombohedral LSF55 was 0.45 eV for both dilute and interacting vacancies (at $\delta = 0.04$ and 0.17). The calculated migration barrier in cubic LSF55 was 0.7 eV at $\delta = 0.12$. Due to the lattice distortion in cubic LSF55, lattice locally transformed towards “rhombohedral LSF55” distortion with a significant reduction in structural energy at $\zeta = 0.25/0.75$ which can be called as “trapped state” in vacancy migration path.

These results show, the effect of phase change on the oxygen vacancy migration barrier is not as substantial (differ by $\sim 0.25\text{eV}$), as it was on oxygen vacancy formation energy (differ by $\sim 0.5\text{eV}$ Figure 5.3).

In Figure 7.2(d) and (e), change of the magnetic moment on oxygen vacancy neighboring Fe atoms are shown in rhombohedral and cubic LSF55, respectively. Oxygen vacancy adjacent Fe1 maintained the same oxidation state before and after oxygen vacancy migration in both, rhombohedral and cubic LSF55. Whereas, the oxidation state on Fe4 (second nearest neighbor to oxygen vacancy) was reduced due to partial charge transfer after oxygen vacancy migration in rhombohedral LSF55. After the migration of the oxygen vacancy from Fe3 adjacent site to Fe2 adjacent site, the oxidation state on Fe2 and Fe3 interchanged in cubic LSF55. However, the magnetic moments Fe2 and Fe3 did not simply interchange in rhombohedral LSF55, due to the anisotropic shape of polaron (Figure 4.2(b) and (f)). Due to symmetric polaron shape in cubic LSF55, the magnetic moment on Fe4 did not change, as it remains as the second nearest neighbor to the oxygen vacancy. A sudden dip in calculated magnetic moment or increase in Fe oxidation state can be observed at $\zeta = 0.25/0.75$, due to the “trapped state” in the migration path. The larger change of the magnetic moment on Fe is in coordination with the higher migration energy barrier in cubic LSF55.

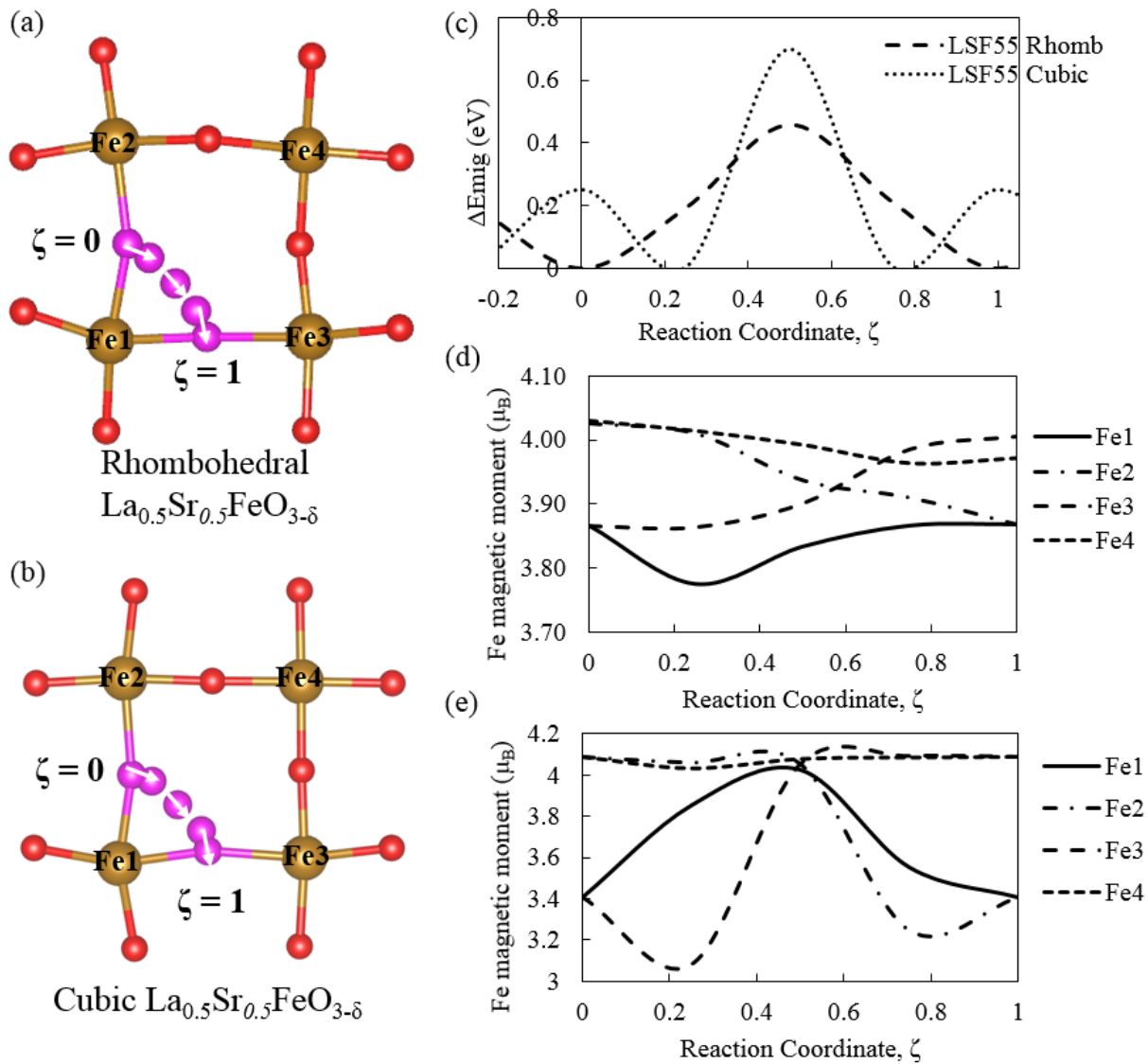


Figure 7.2. Oxygen migration in LSF55. The pink atoms in (a) highlight the oxygen migration path in Rhombohedral LSF55 with $\delta = 0.04$, and (b) highlight the oxygen migration path in cubic LSF55 with $\delta = 0.13$. Figure (c) shows the oxygen migration barrier in rhombohedral and cubic LSF55. (d) shows the charge change on the oxygen vacancy neighboring Fe atoms in rhombohedral LSF55 as a function of oxygen atom coordinate (corresponds to Figure (a)). Figure (e) shows the charge change on the oxygen vacancy neighboring Fe atoms in cubic LSF55 as a function of oxygen atom coordinate (corresponds to Figure (b)).

7.1.3 Oxygen Vacancy Migration in SrFeO_{3-δ}

Figure 7.3(a) shows the oxygen migration path (pink atoms) in cubic SFO. The lattice distortion shown in the figure corresponds to the transition state lattice distortion. As shown in Figure 7.3(b), the calculated oxygen migration barriers for cubic SFO were 0.58, 0.62 and 1.07 eV at $\delta = 0.04$, 0.12, and 0.5 respectively. These results show that the effect of oxygen nonstoichiometry on the oxygen vacancy migration barrier is insignificant (<0.05 eV) below a critical nonstoichiometry, above which oxygen vacancy strongly interacts (at $\delta = 0.5$). From the oxygen vacancy site fraction calculations shown in Figure 6.2 and 6.3 within SOFC operating temperature (in air), it can be noticed the oxygen vacancy concentration is less than ~0.125 in cubic SFO until it transforms to tetragonal phase. Below this concentration, the migration energy barrier is ~0.6eV and does not change with δ .

Figure 7.3(c) shows the magnetic moment change on neighboring Fe atoms during the migration. The magnetic moment on vacancy adjacent Fe1 goes through a minimum during oxygen vacancy migration, i.e., Fe oxidation state was increased at transition state during oxygen vacancy migration, because excess electrons were pushed to the second nearest neighboring Fe4. Fe1 maintained same oxidation state, ~4.1+ before and after oxygen vacancy migration due to its square pyramidal coordination with neighboring oxygen atoms. Initially ($\zeta = 0$), the oxygen vacancy was between Fe1 and Fe3. Therefore, the oxidation state on square pyramidal-Fe1 and Fe3 were same, (~4.1+) corresponding to vacancy adjacent or nearest neighboring Fe and magnetic moment on Fe2 and Fe4 were same, (~3.8+) corresponding to oxygen vacancy second nearest neighboring Fe (Figure 7.3(c)). After oxygen vacancy moved to the site between Fe1 and Fe2 ($\zeta = 1$), oxidation state on Fe2 increased to 4.1+ due to square pyramidal coordination and second nearest

neighboring Fe3 and Fe4 have oxidation state of 3.8+ due to octahedral coordination. So, the oxidation state on Fe2 and Fe3 interchanged due to oxygen vacancy migration. Same as cubic LSF55, in cubic SFO (which has a large polaron volume Figure 4.2(d)) the charge on the second nearest neighboring Fe4 remained constant during oxygen migration (Figure 7.3(c)). Overall, Figure 7.3(c) also shows that the extent of magnetic moment/Fe oxidation change on the oxygen-vacancy-neighboring Fe ($\sim 0.3 \mu_B$) was not as large as it was for LFO ($\sim 1.3 \mu_B$), due to the distributed nature of the polaron.

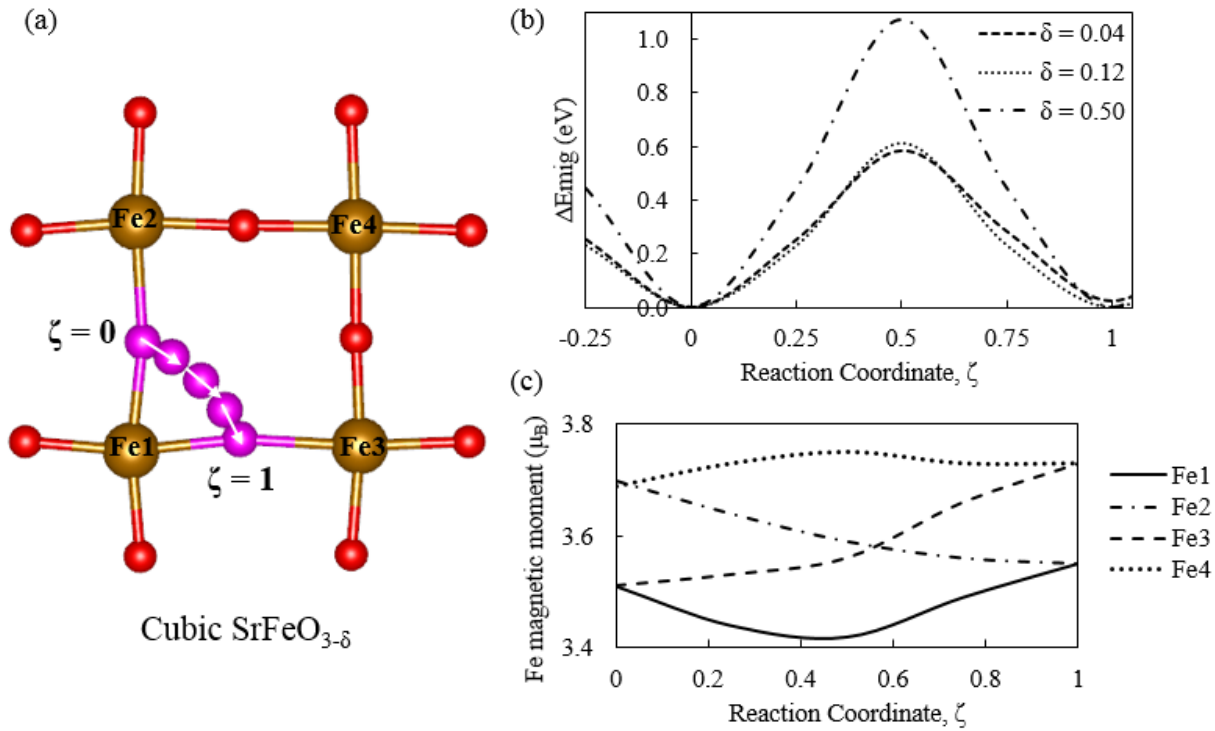


Figure 7.3. Oxygen migration in cubic $\text{SrFeO}_{3-\delta}$. The pink atoms in Figure (a) highlight the oxygen migration path, Figure (b) shows the oxygen migration barrier along this path for two different δ , and Figure (c) shows the charge change on the neighboring Fe atoms as a function of oxygen atom coordinate on its path.

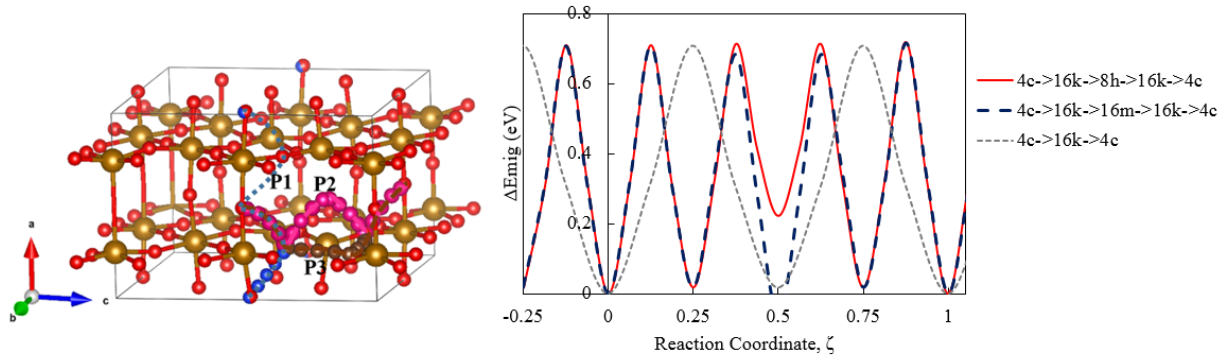


Figure 7.4. Oxygen migration in tetragonal $\text{SrFeO}_{3-\delta}$. (Left) non-red smaller atoms highlight the oxygen migration paths. Paths are defined with Wyckoff positions of oxygen atoms in the perfect lattice; P1: $4c \rightarrow 16k \rightarrow 8h \rightarrow 16k \rightarrow 4c$; P2: $4c \rightarrow 16k \rightarrow 16m \rightarrow 16k \rightarrow 4c$; P3: $4c \rightarrow 16k \rightarrow 4c$. (Right) oxygen migration barrier at different coordinates (ζ) of the path.

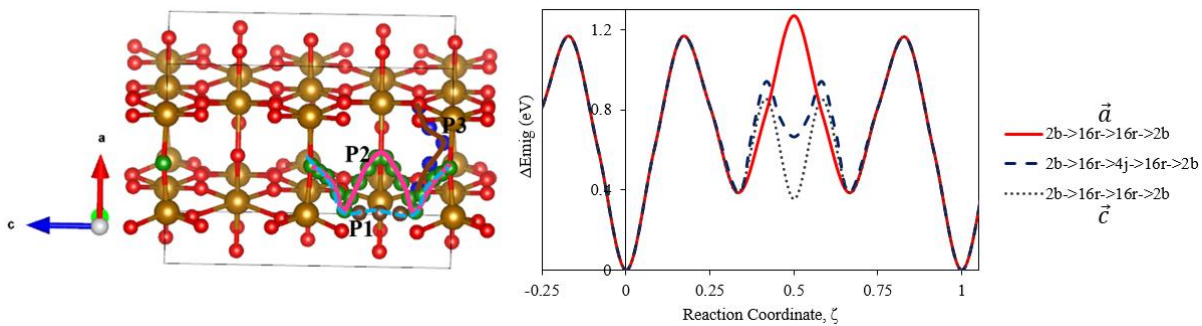


Figure 7.5. Oxygen migration in orthorhombic $\text{SrFeO}_{3-\delta}$. (Left) non-red smaller atoms highlight the oxygen migration paths. Paths are defined with Wyckoff positions of oxygen atoms in the perfect lattice; P1: $2b \rightarrow 16r \rightarrow 16r \rightarrow 2b$ (c -direction); P2: $2b \rightarrow 16r \rightarrow 4j \rightarrow 16r \rightarrow 2b$; P3: $2b \rightarrow 16r \rightarrow 16r \rightarrow 2b$ (a -direction). (Right) oxygen migration barrier at different coordinates (ζ) of the path.

Due to the presence of multiple oxygen vacancy migration paths in tetragonal and orthorhombic strontium ferrite (multiple migration paths are designated in Figure 7.4-7.5 by the Wyckoff positions of the oxygen atoms in perfect lattice along each path), the minimum energy path for oxygen ion migration was used to estimate the vacancy migration barrier. Figure 7.4 and 7.5 show that for tetragonal and orthorhombic SFO, the migration barriers are 0.71 and 1.17 eV, respectively.

Figure 7.4 shows in tetragonal SFO, three different migration paths: P1, P2, and P3 have almost the same oxygen vacancy migration barrier of ~ 0.7 eV. Therefore, migration barrier in tetragonal SFO is isotropic in nature, independent of direction of migration. Whereas, Figure 7.5 shows oxygen vacancy migration barrier in orthorhombic SFO is anisotropic in nature.

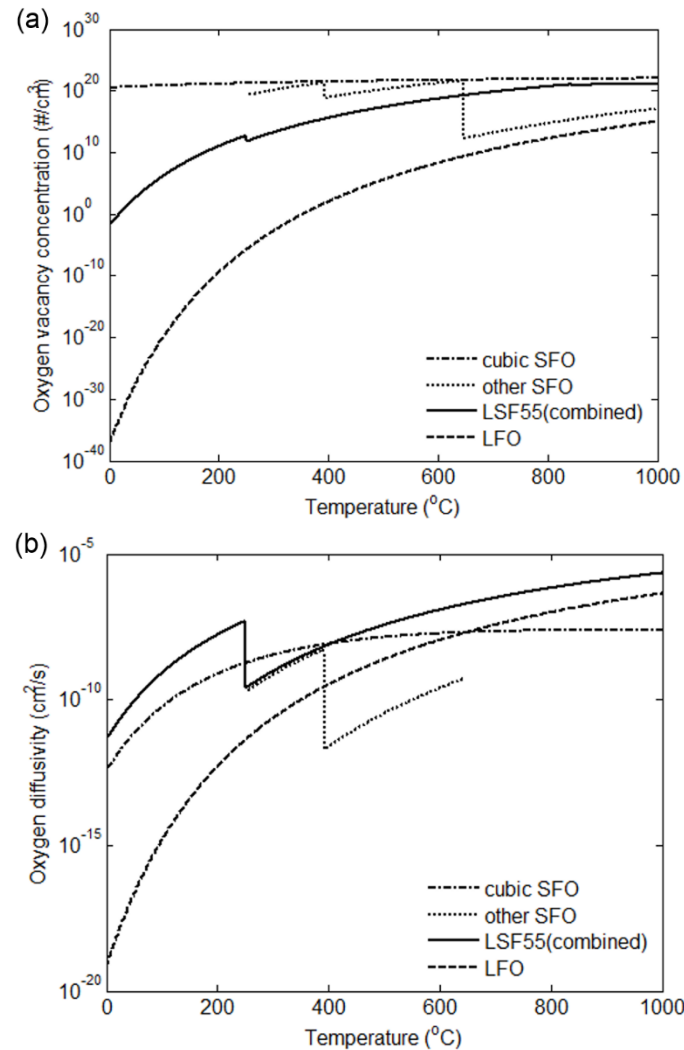
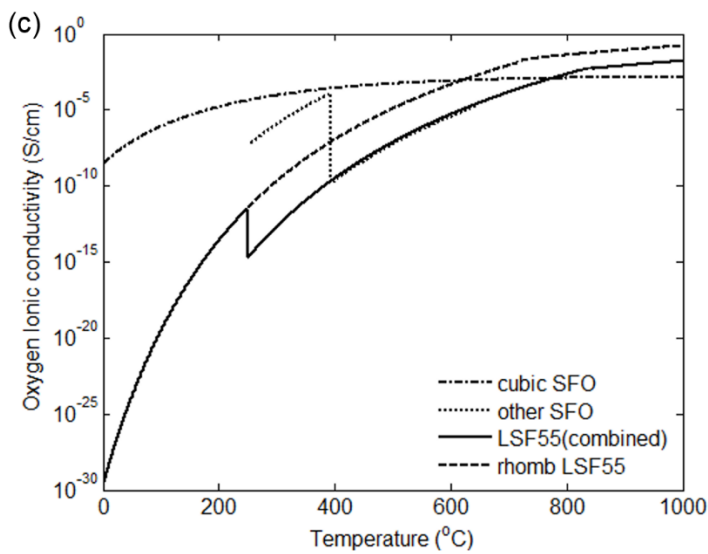


Figure 7.6. Oxygen vacancy (a) concentration (b) ion diffusivity, and (c) ion conductivity in different LSF compositions as a function of temperature in air. In Figure legends ‘cubic SFO’ represent cubic $\text{SrFeO}_{3-\delta}$ data. ‘other SFO’ represent combined data for tetragonal, orthorhombic, and brownmillerite phase in Figure 7.6(a) and tetragonal and orthorhombic phases in Figure 7.6(b,c). ‘LSF55(combined)’ represents the LSF55 data with phase change from rhombohedral to cubic. ‘rhomb LSF55’ in Figure 7.6(c) represent the computed oxygen ionic conductivity data for rhombohedral LSF55 phase.

Figure 7.6 (cont'd)



7.2 Oxygen Ionic Conductivity in $\text{La}_{1-x}\text{Sr}_x\text{FeO}_{3-\delta}$ as a Function of Temperature (in Air)

Using oxygen vacancy site fractions calculated in Chapter 6, oxygen vacancy concentration was calculated for different LSF compositions, with Equation 1.5. Oxygen ion diffusion coefficient or diffusivity in different LSF compositions and phases were calculated from the migration barrier (discussed in Section 7.1) using Equation 1.8. The overall oxygen ion conductivity was calculated using Equation 1.1. The data was plotted as a function of temperature in air in Figure 7.6. As the phase diagram (Figure 6.3(c)) have shown several phase transformations. This was included in the calculation for “LSF55 (combined)”, in which the rhombohedral to cubic phase transformation occurs at $250 \pm 50^\circ\text{C}$.⁶⁵ To illustrate the impact of phase change on ionic conductivity, individual phases, such as “cubic SFO” and “rhomb LSF55” were calculated (ignoring the phase change) for comparison. “other SFO” means tetragonal, orthorhombic and brownmillerite SFO phases were considered in their specific phase stable temperature range. The ionic conductivity for LFO were too low to show in Figure 7.6(c).

Figure 7.6(a) shows oxygen vacancy concentration in different phases of LSF. Due to very high oxygen vacancy formation energy, ~3.5 eV in LFO (Figure 5.3), vacancy concentration in it was relatively low. Oxygen vacancy concentration data for LSF55 shows a kink around 250°C due to rhombohedral to cubic phase transition in bulk structure.⁶⁵ Cubic SFO remains almost constant due to low oxygen vacancy formation energy in this material. Whereas, oxygen vacancy concentration in other (tetragonal, orthorhombic, brownmillerite) SFO phases fluctuates with temperature, due to oxygen vacancy ordered phase transition which causes loss in mobile oxygen vacancy concentration from vacancy site ordering. Once brownmillerite SFO formed at high temperature, the vacancy concentration in it also drastically reduced due to high oxygen vacancy formation energy, ~3 eV. As a result, oxygen vacancy concentration in brownmillerite SFO becomes comparable to vacancy concentration in LFO. Maximum oxygen vacancy concentration can be observed in orthorhombic SFO at ~ 650°C in the air.

The oxygen diffusivity in LFO is lower than the other LSF compositions. Rhombohedral LSF55 shows the highest oxygen ionic diffusivity in LSF family at low temperature but it drops after 250°C, due to rhombohedral to cubic phase transition and oxygen vacancy migration barrier in cubic LSF55 was higher than rhombohedral LSF55 (Section 7.1.2). Diffusivity of oxygen ion in tetragonal and orthorhombic SFO was lower than cubic SFO due to higher migration barrier in previous phases as reported in Section 7.1.3.

Figure 7.6(c) shows the ionic conductivity comparison in different LSF compositions. It clearly captured LSF55 possesses the highest ionic conductivity at or above 800°C in the air. The dotted line represent hypothetical rhombohedral LSF55 phase (as rhombohedral LSF55 transform to cubic at ~250°C in air). The calculated ionic conductivity for LSF55 at 950°C was 0.3977 S/cm was comparable to experimentally measured ionic conductivity (0.5 S/cm) at the same

temperature.⁶² As LSF64 has better stability for rhombohedral phase, this may be the reason for the broader application of LSF64 as the best MIEC candidate in LSF family.¹⁶⁶ If the rhombohedral LSF55 can be stabilized at a higher temperature, it will be even more desirable than LSF64, due to its higher oxygen vacancy concentration. On the other-hand, SFO will lose its ionic conductivity at high temperature due to continuous phase change, starting from the tetragonal phase. Though it was previously shown in Figure 6.3(b-c) orthorhombic SFO possess highest oxygen vacancy concentration within the SOFC operating window (0 – 1000°C) in the air but due to high oxygen ion migration barrier, it is not best candidate as oxygen ion conductor. Due to low oxygen vacancy formation energy, cubic SFO possess the highest oxygen ionic conductivity at low temperature (below 300°C). Therefore, stabilizing cubic SFO (avoiding phase transformation) to higher temperature will lead to higher oxygen ionic conductivity.

8. Anisotropic Chemical Strain Produced by Non-Stoichiometric Cubic CeO_{2-δ}

It can be noticed from Figure 2.5(a) each oxygen atom/ oxygen vacancy site ($V_0^{\bullet\bullet}$) in Ceria is coordinated with four Cerium atoms. As discussed in Section 2.6 on neutral oxygen vacancy formation two electrons are generated, it can be distributed to four adjacent Ce-atoms (symmetric distribution) or can remain localized to two Ce atoms (asymmetric distribution).

8.1 Charge Disproportionation in Non-stoichiometric Ceria

The asymmetric scenario provided energetically favorable minima. The details of calculation results are tabulated in Table 8.1. The non-uniform distortion was energetically favorable over uniform distortion by 0.55 eV. Without initial perturbation, four Ce-atoms will show a 3.5+ charge due to an equal share of electrons (GGA calculations symmetrically distribute the electron cloud). Whereas in energetically favored case, two perturbed-Ce maintained 4+ charge and the other two Ce became 3+ (Figure 8.1(a)). According to the bond distance calculation, oxygen atoms (O-Ce- $V_0^{\bullet\bullet}$) opposite to $V_0^{\bullet\bullet}$ of Ce, moved closer to the Ce in <111>.

Table 8.1. Comparing calculated energy and bond lengths for different Vo-formation cases.

Ceria Structure (2x2x2)	0 K Formation Energy (eV)	Charge on Ce	Ce – O bond distance (Å)	Ce – $V_0^{\bullet\bullet}$ bond distance (Å)	$V_0^{\bullet\bullet}$ /O – Ce – O distance (Å)
Perfect lattice	-783.63	4+	2.38	-	4.76
With symmetric $V_0^{\bullet\bullet}$	-775.20	3.5+	3x2.38, 3x2.37, 1x2.29 2x2.44,	2.53	4.82
With asymmetric $V_0^{\bullet\bullet}$	-775.75	3+ 4+	3x2.42, 1x2.43, 1x2.33 2x2.31, 2x2.35, 1x2.33, 1x2.34, 1x2.27	2.52 2.56	4.85 4.82

This observation is opposite to the hypothesis of Korobko *et al.*⁷⁵ All Ce ions moved away from the $V_0^{\bullet\bullet}$ -site along $\langle 111 \rangle$, Ce^{4+} moved further than Ce^{3+} . Four O-atoms along the O-Ce- $V_0^{\bullet\bullet}$ direction moved away from $V_0^{\bullet\bullet}$, O-Ce³⁺- $V_0^{\bullet\bullet}$ moved further than O-Ce⁴⁺- $V_0^{\bullet\bullet}$ (Table 8.1). The complicated local distortion due to the $V_0^{\bullet\bullet}$ formation is shown in Figure 8.1(b). It is the core of lattice distortion from the 2x2x2 supercell after oxygen vacancy formation. The complicated distortion was partially hypothesized before^{136,137} but here the complete description along with its' effect on chemical strain is described. All the (seven) Ce⁴⁺-O²⁻ bonds were shortened (blue). Six Ce³⁺-O²⁻ bonds were elongated (red) except the O-Ce³⁺ bond, with O-atom diagonally opposite to the $V_0^{\bullet\bullet}$ -site (blue). Green-O came closer to the $V_0^{\bullet\bullet}$ -site and other red-O moved away from $V_0^{\bullet\bullet}$. O-O distance in a perfect ceria lattice was 2.75 Å. Four O-atoms (green) connected to both Ce³⁺ and Ce⁴⁺ came closer to $V_0^{\bullet\bullet}$ and was 2.62 Å from the $V_0^{\bullet\bullet}$ -site. O-atom (green) connected to two Ce³⁺ moved away from $V_0^{\bullet\bullet}$, was 2.76 Å away from the $V_0^{\bullet\bullet}$ -site. O-atom (red) connected to two Ce³⁺ moved away from $V_0^{\bullet\bullet}$, was 2.76 Å away from the $V_0^{\bullet\bullet}$ -site.

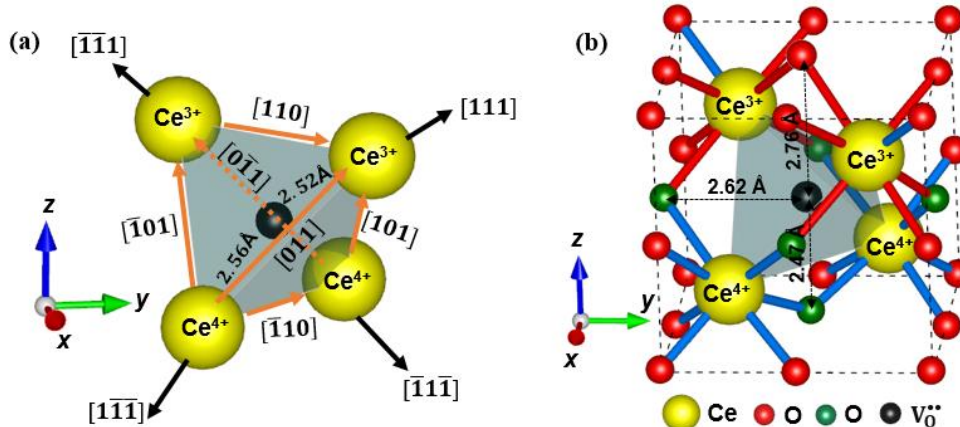


Figure 8.1. Charge distribution on Ce and displacement of O-atoms around neutral oxygen vacancy ($V_0^{\bullet\bullet}$). Red-O moved away from oxygen vacancy site. Green-O came closer to oxygen vacancy site. Red Ce-O bond signify elongation with respect to bond length in perfect structure and blue Ce-O bond signify contraction.

8.2 PDOS of Perfect and Oxygen Vacancy Adjacent Ce

Partial density of states (PDOS) was calculated for Ce and O atoms in the perfect CeO_2 lattice and shown in Figure 8.2. Figure 8.3(a-c) show the Ce- $5d$ and $4f$ orbitals in vacancy containing lattice for two different scenarios. Analysis of the PDOS for Ce- $5d$ and $4f$ orbitals before and after the formation of oxygen vacancy has shown the charge localization in $4f$ orbital after $V_0^{\bullet\bullet}$ formation. Electron localization in Ce- $4f$ orbital observed in Figure 8.3(b) is consistent with previous computational studies.^{69,172} Whereas, Figure 8.3(a) shows the Ce^{4+} state which is comparable to PDOS of Ce^{4+} present in the perfect lattice (Figure 8.2). PDOS plot for $\text{Ce}^{3.5+}$ in Figure 8.3(c) shows electron density in the $4f$ orbital of Ce is clearly in between of PDOS for Ce^{3+} and Ce^{4+} .

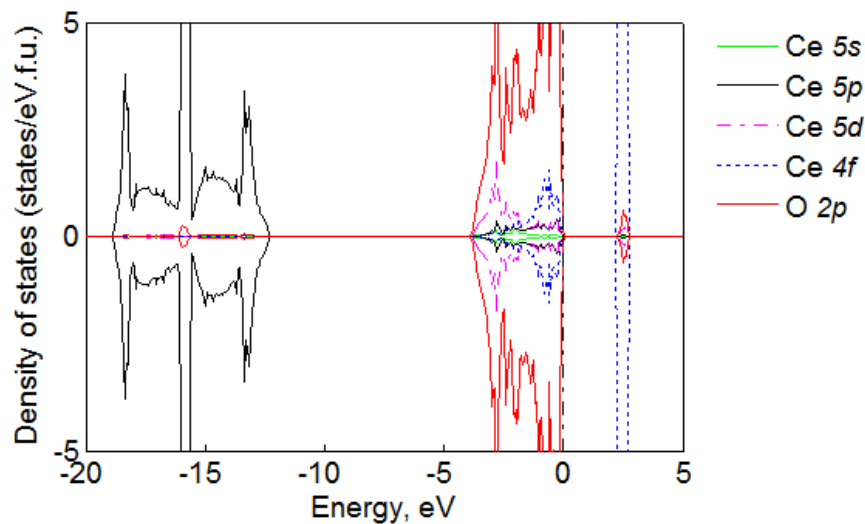


Figure 8.2. Partial density of states plot for Ce- $5s$, $5p$, $5d$, $4f$ and O- $2p$ orbitals in pure CeO_2

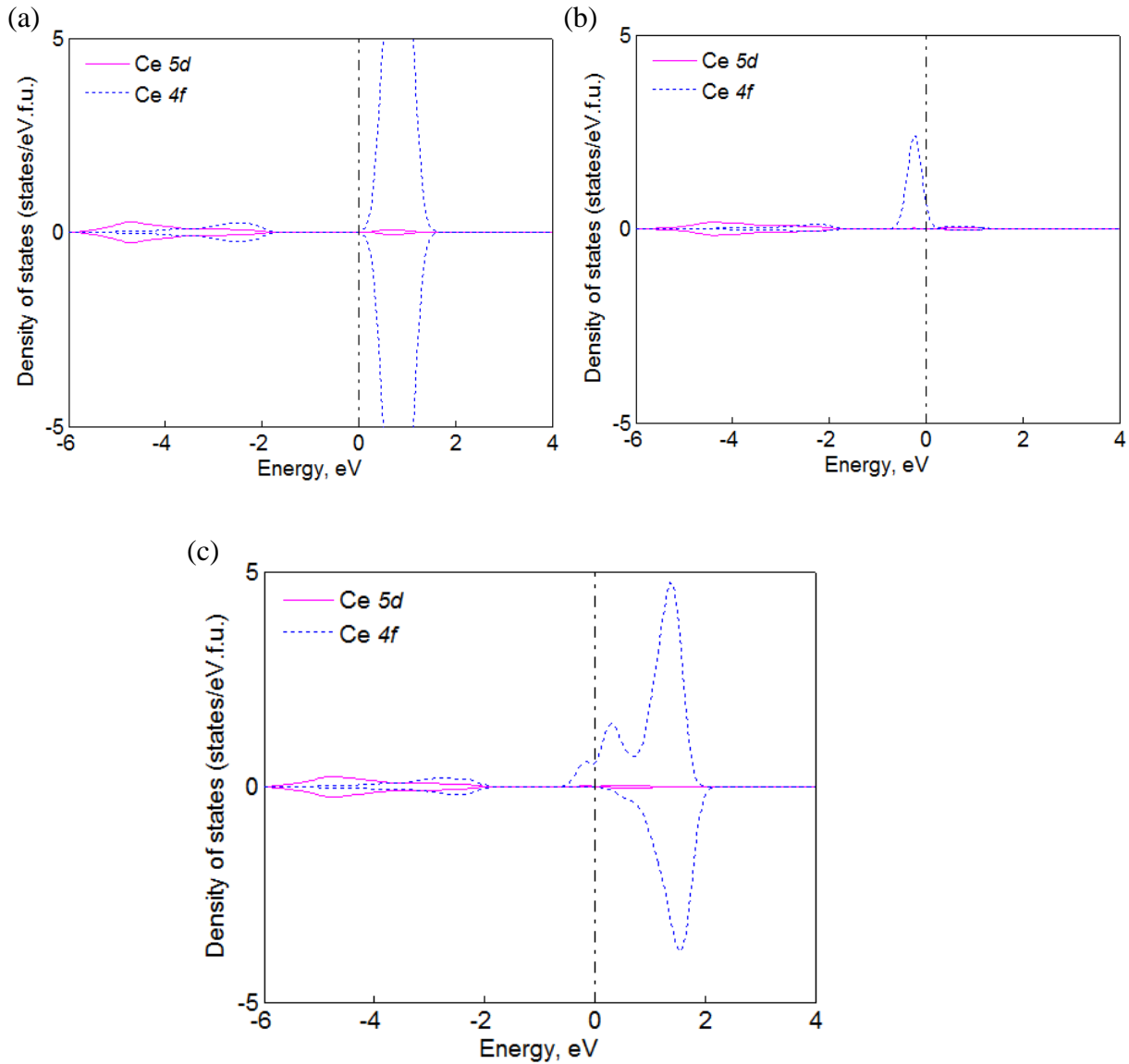


Figure 8.3.(a) PDOS for Ce^{4+} -5d and Ce^{4+} -4f orbital for Ce^{4+} adjacent to $V_O^{\bullet\bullet}$, after $V_O^{\bullet\bullet}$ formation in asymmetric case. Orbitals show same shape as Ce^{4+} in perfect CeO_2 . (b) PDOS for Ce^{3+} -5d and Ce^{3+} -4f orbital for Ce^{3+} adjacent to $V_O^{\bullet\bullet}$, after $V_O^{\bullet\bullet}$ formation in asymmetric case. Figure shows localization of excess electron in 4f orbital. (c) PDOS for $\text{Ce}^{3.5+}$ -5d and $\text{Ce}^{3.5+}$ -4f orbital for $\text{Ce}^{3.5+}$ adjacent to $V_O^{\bullet\bullet}$, after $V_O^{\bullet\bullet}$ formation in symmetric case. Figure shows localization of excess electron in 4f orbital. This scenario is computational artifact as the structure was energetically unfavorable.

8.3 Calculating Anisotropic Chemical Strain

It was interesting to notice how the non-uniform local deformation is impacting the overall chemical strain. Method to calculate the anisotropic chemical strain coefficient tensor is described in Section 2.6. G tensor is calculated from the slope of $dE_{V_0^*, \varepsilon}^f$ versus ε as shown in Figure 8.4.

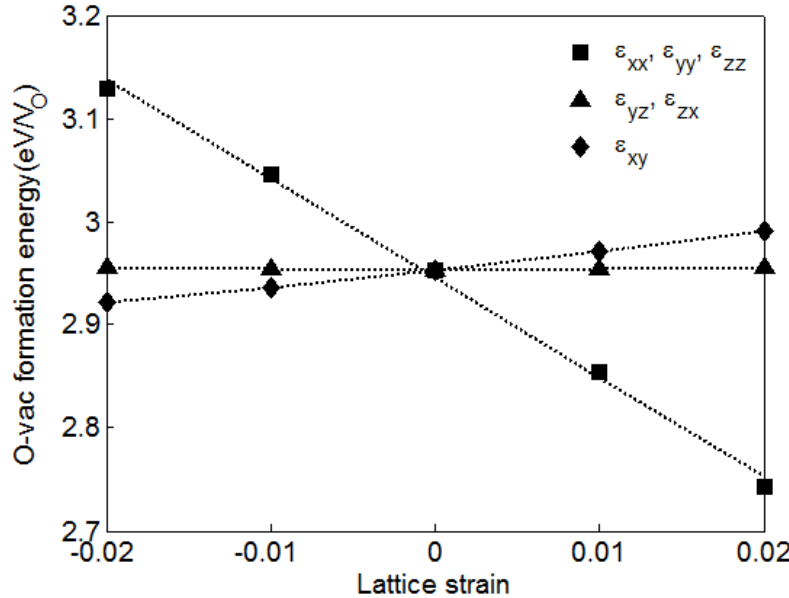


Figure 8.4. The oxygen vacancy formation energy varies with an applied strain in different directions. The slope of the strain versus energy curve gives the elastic dipole tensor mapped with applied strain direction.

$$G = \begin{bmatrix} -9.633 & 0.001 & 0.001 \\ 0.001 & -9.633 & 1.734 \\ 0.001 & 1.734 & -9.633 \end{bmatrix}$$

Energy for the short and long range interaction was calculated using Equation 2.22 and 2.23 respectively. V_U for this calculation is 41.50\AA^3 , volume per formula unit of the perfect CeO_2 . Due to cubic symmetry of the perfect lattice components of the elastic stiffness tensor, \mathbb{C} can be defined as $C_{11} = 343 \text{ GPa}$, $C_{22} = 103 \text{ GPa}$, and $C_{44} = 54 \text{ GPa}$, was comparable to previous calculations.¹⁷³ Calculated Young's modulus of 198 GPa was also comparable to previous experimental study.¹⁷⁴

Calculated ε_C at $\delta = 0.03$ and α_C is provided below. The mean chemical expansion coefficient $\alpha_{C,M} = 0.067$ was comparable to experimentally obtained average α_C .^{40,175}

$$\varepsilon_C = \begin{bmatrix} 0.002 & 0.000 & 0.000 \\ 0.000 & 0.002 & -0.039 \\ 0.000 & -0.039 & 0.002 \end{bmatrix}, \quad \alpha_C = \begin{bmatrix} 0.067 & 0.000 & 0.000 \\ 0.000 & 0.067 & -0.124 \\ 0.000 & -0.124 & 0.067 \end{bmatrix}$$

The α_C calculated above was not able to show the anisotropic effect in principle directions. On diagonalization of the α_C , one can obtain the total effect of the chemical strain projected in principle directions. Therefore, the Eigen values and Eigen vectors were calculated. Where, Eigen vectors provides the rotation matrix, R and Eigen values show components of the chemical expansion coefficient mapped to the principle directions, $\alpha_{C,P}$.

$$R = \begin{bmatrix} 0 & 0 & 1 \\ 1 & 1 & 0 \\ 1 & 1 & 0 \end{bmatrix}, \quad \alpha_{C,P} = \begin{bmatrix} 0.191 & 0.000 & 0.000 \\ 0.000 & -0.057 & 0.000 \\ 0.000 & 0.000 & 0.067 \end{bmatrix}$$

On close observation of the rotation matrix (or the Eigen vectors), one can notice that the x and y-axis of the diagonalized tensor was mapped to $[0\bar{1}1]$ and $[011]$ direction respectively. This is the direction between Ce^{3+} and Ce^{4+} (Figure 8.1(a)). Therefore, orienting the lattice in $<110>$ one can maximize the anisotropic chemical strain effect. After diagonalizing the strain tensor, the anisotropic effect is clearly observed. The maximum possible chemical expansion coefficient was 0.191, and in perpendicular direction, there was compressive strain effect with $\alpha_{C,yy} = -0.057$. Principle positive chemical expansion coefficient, $\alpha_{C,PP}$ for ceria was calculated as 0.129. The average ε_C with δ , observed in the experiment is comparable to the calculated average ε_C with δ in this study (Figure 8.5(a)). $\alpha_{C,PP}$ provided the upper bound for all the experimental data, whereas $\alpha_{C,M}$ is comparable to previous experimental observations (Figure 8.5(a)).

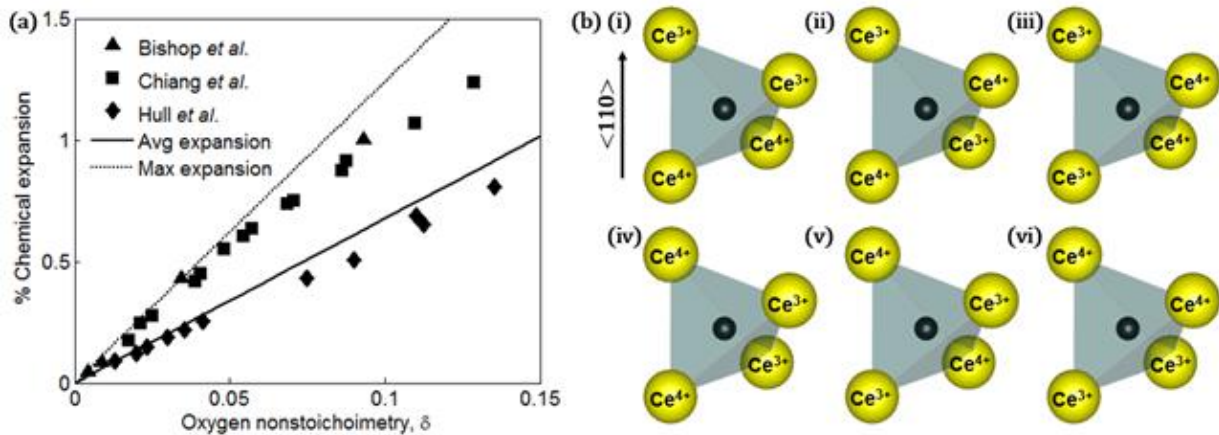


Figure 8.5.(a) Average expansion of single crystal ceria with increasing oxygen nonstoichiometry. (b) possible orientations of Ce^{3+} and Ce^{4+} atoms around oxygen vacancy.

There are six possible directions in nonstoichiometric ceria for local orientation in $<110>$ among Ce^{3+} and Ce^{4+} ions around the V_0^{2-} -site (Figure 8.5(b)) but without any applied electric field they are randomly oriented giving the average effect of the chemical strain ($\alpha_{C,M} = 0.067$). Assuming an electric field applied in $<110>$ direction of the Figure 8.5(b), it can be noticed only in Figure 8.5(b)(i-ii) Ce^{4+} - Ce^{3+} are oriented in preferred direction of applied bias but other Ce atoms in Figure 8.5(b)(iii-vi) are randomly oriented. On application of the electric field electrons got transferred from Ce^{3+} to Ce^{4+} to align the polaron in the preferred orientation of the applied bias so there are less degenerated states. The resultant effect of the preferred orientation produce the amplified chemical strain in the material. If the crystal orientation is known then chemical strain due to electric field, E_{α_C} can be calculated as $E_{\alpha_C} = \text{Oriented}(\alpha_C) - \text{tr}(\alpha_C)$.

9. Conclusion and Future Work

9.1 Thesis Summary and Conclusion

This thesis performed DFT-based investigations on the oxygen vacancy formation, interaction, transport, and its' chemical strain effect in perovskite LSF, and fluorite $\text{CeO}_{2-\delta}$, as two important members of oxide families for SOFC applications. Several computational challenges were solved and many insights were developed from these calculations.

To elucidate the effect of oxygen vacancy polaron shape and size on the vacancy interaction in LSF, three different LSF compositions were computationally studied with GGA+U. Hubbard- U ($= 3$) parameter was calibrated in order to predict the magnetic moment on Fe as a function of La/Sr ratio and oxygen non-stoichiometry. The magnetic moment on Fe was utilized to interpret the formal charge on Fe. The oxidation state change on Fe upon oxygen vacancy generation outlined the shape and size of the oxygen polarons. When an oxygen vacancy is formed in a perovskite lattice, the two neighboring Fe-O coordinated octahedra collapse into two square pyramids. It was found that in LaFeO_3 the excess electrons produced during oxygen vacancy formation were localized at the square pyramidally (Fe-O₅) coordinated Fe atoms adjacent to the oxygen vacancy, resulting in a small polaron. In contrast, in SrFeO_3 the excess electrons produced during oxygen vacancy formation were transferred to the octahedrally (Fe-O₆) coordinated second-nearest-neighbor Fe atoms, resulting in a pancake-shaped large polarons. This difference is well explained by the electron occupancy and crystal-field-splitting-induced differences between the Fe 3d-orbitals of the square pyramidally coordinated, oxygen-vacancy-adjacent Fe atoms and the octahedrally-coordinated, oxygen-vacancy-second-nearest-neighbor Fe atoms. For $\text{La}_{0.5}\text{Sr}_{0.5}\text{FeO}_{3-\delta}$, the polaron size in the rhombohedral phase was smaller than that in cubic phase, due to the tilt of Fe-O₆ octahedra. In all cases, larger oxygen vacancy polarons resulted in higher oxygen vacancy

interactions. In fact, in multiple phases, the oxygen vacancy formation energy started to increase with oxygen non-stoichiometry beyond a critical value when the polarons began to overlap. There has been a long-standing debate in the literature on the mixed charge states of Fe in the $\text{SrFeO}_{3-\delta}$. The magnetic moment interpreted charge state correlations presented here clearly show that square pyramidal Fe always remains +4 in $\text{SrFeO}_{3-\delta}$. The charges of Fe in the distorted octahedra in $\text{SrFeO}_{3-\delta}$ vary from +4 to +3 depending on δ , and they are easier to reduce than those in square pyramidal coordination, as explained with crystal field theory. As a result, in all strontium ferrite structures 1) oxygen vacancies are always formed at the site shared by the two highest charged octahedral Fe (except brownmillerite) and 2) the oxygen vacancy formation energy increases after each phase transformation.

Overall, the calculated polaron shape changes and progressively increased polaron sizes with increasing Sr-doping, resulted in increasing oxygen vacancy formation energies in $\text{La}_{1-x}\text{Sr}_x\text{FeO}_{3-\delta}$. This was consistent with experimental results showing that Sr-rich LSF and highly oxygen deficient compositions are more prone to oxygen-vacancy-ordering-induced phase transformations, while Sr-poor and oxygen rich LSF compositions are not. Since oxygen vacancy induced phase transformations cause a decrease in the mobile oxygen vacancy site fraction (X), both δ and X were also predicted as a function of temperature and oxygen partial pressure, for multiple LSF compositions and phases using a combined thermodynamics and DFT approach.

The oxygen vacancy migration barrier did not change with the oxygen nonstoichiometry in rhombohedral LSF55 and orthorhombic LFO, due to smaller polaron volume. With stronger oxygen vacancy interaction, SFO demonstrated increasing oxygen vacancy migration barrier with phase change (cubic < tetragonal <orthorhombic). LSF55 also showed increased oxygen vacancy migration barrier due to rhombohedral to cubic phase change. Finally, computationally predicted

ionic conductivity showed rhombohedral LSF has higher conductivity than cubic LSF at the same SOFC operating conditions. Cubic SFO is promising at low temperature, as it possess the highest ionic conductivity than other phases until its cubic to tetragonal phase transition at ~250°C. Comparing all the phases and compositions of LSF, the overall effect of phase change on the oxygen vacancy migration barrier is not as substantial (differ by ~0.7eV), as it was on oxygen vacancy formation energy (differ by ~3eV). Therefore increasing oxygen vacancy site fraction can be more beneficial in improving the conductivity.

Computationally predicted anisotropic chemical strain in cubic ceria explained the reason behind observed anomalous strain effect in this material on application of electric field. The presence of highly localized $4f$ valance orbital in Ce causes charge disproportionation on the formation of neutral oxygen vacancy, producing anisotropic chemical strain in crystal with cubic symmetry. Calculated average chemical expansion was comparable to experimental observation. Without application of external bias, strain field polaron remain randomly oriented giving average effect of anisotropic chemical strain. On the application of electric field, Ce^{3+} - Ce^{4+} bonds orient perpendicular to the thin film enhancing chemical strain effect.

9.2 Future Work

Cubic SFO has shown a good ionic conductivity at relatively low temperature due to very low oxygen vacancy formation energy (0.4 eV) at the dilute condition.¹⁷⁶ But due to vacancy ordering induced phase change to tetragonal structure, it loses its ionic conductivity even at ~250°C. To resist the vacancy ordering induced phase transition, a Ruddlesden-Popper (RP)¹⁷⁷ type strontium ferrite structure can be investigated in future.¹⁷⁸ As shown in Figure 10.1 the RP type $\text{Sr}_3\text{Fe}_2\text{O}_7$ (RP-SFO) has layered FeO_6 octahedral structure, where Fe maintains its 4+ charge state.¹⁷⁹ Further, it was discussed in Chapter 5, that it was easier to form oxygen vacancy adjacent to Fe^{4+} and

prevent vacancy ordered phase transition. However, its diffusion mechanism is largely unknown. Maljuk *et al.*¹⁸⁰ have grown high purity RP-SFO single crystal, experimentally. Its potential as a SOFC cathode material is worth to investigate.

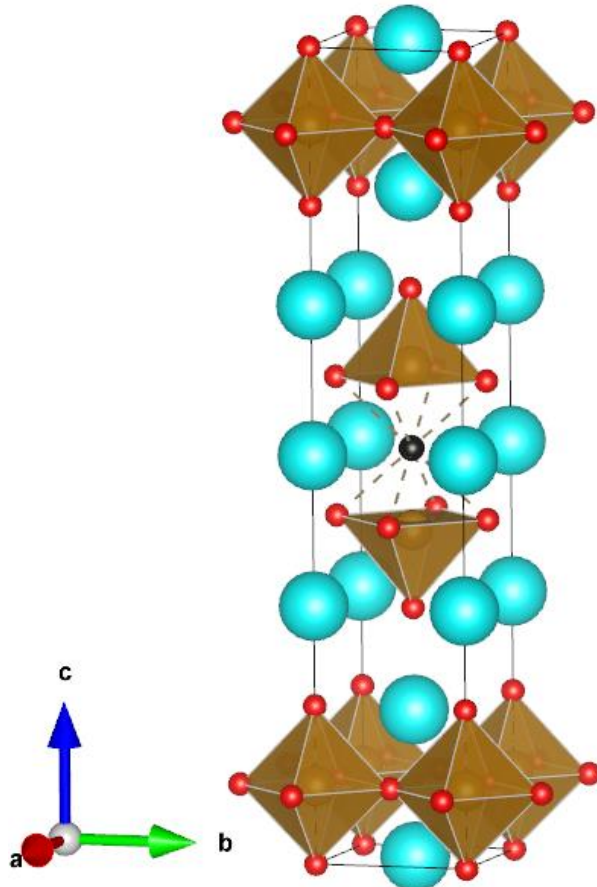


Figure 9.1. Ruddlesden-Popper type $\text{Sr}_3\text{Fe}_2\text{O}_7$ lattice with single oxygen vacancy (black atom) at the center. Blue, brown, and red atoms are Sr, Fe, and O respectively. $\text{Sr}_3\text{Fe}_2\text{O}_7$ can be a promising compound for low-temperature SOFC cathode.

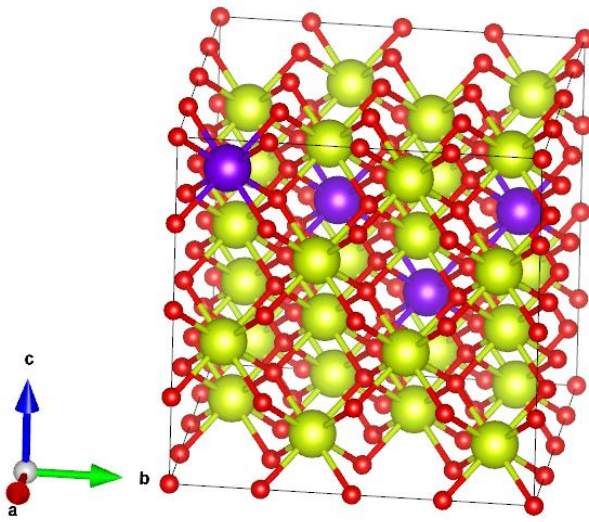


Figure 9.2. Crystal structure of 12.5% Gd/Sm/Pr (purple atoms) doped ceria (GDC/SDC/PDC). Here, Ce and O atoms are colored in yellow and red respectively. Gd/Sm/Pr atoms are randomly distributed in the lattice.

Gd, Sm, or Pr doped ceria is commonly used in place of pure ceria due to increased oxygen vacancy concentration in it via doping, under same operating environment. Chapter 8 elucidates how the presence of dilute oxygen vacancy produces anisotropic chemical strain in the cubic lattice and described the complicated lattice distortion around oxygen vacancy. Further studies are required to understand the effect of the highly doped ceria and how the presence of foreign element around oxygen vacancy influences the shape and size of the polaron. In addition, studies are required to understand the effect of oxygen vacancy interaction in doped ceria with higher oxygen vacancy concentration.

APPENDIX

APPENDIX

Numerical Method to Find Temperature Corresponding to an Oxygen Nonstoichiometry for Certain O₂ Partial Pressure (MATLAB code) to Solve Equation 2.17.

```
% Temperature from nonstoichiometry
TC = 0:0.1:2000; % Temperature range in deg C
T = TC+273.15; % T in K
p = 0.21; % atm
R = 8.314e-3; % kJ/mol-K
cF = 96.485; % 1eV = 96.485 kJ/mol --> conversion Factor
Nv = 3; % # of available sites/ formula unit
x = 0.0625; % Nonstoichiometry
Evac_DFT = 0.56; % Vacancy formation energy
%
for i = 1:length(T)
    mu_O2_corr = O2_correction(T(i),p)/cF;
    %
    G_vac(i) = Evac_DFT + 0.5 * mu_O2_corr;
    %
    A_fac = exp(-G_vac(i)*cF/(R*T(i)));
    nonstoi(i) = Nv*A_fac/(1+A_fac);
%
if nonstoi(i) >= x
    vac_form = E_vac(i);
    TempK=T(i);
    delta = nonstoi(i);
    break;
end
end
%
TempC = TempK-273.15% Temperature in deg C
```

Function: O2_correction

```
function mu_O2_corr = O2_correction(T,p)
% This function returns connection energy in eV for oxygen MOLECULE
% between room temperature(298.15K) at 1 bar (0.987 atm) and
% any other temperature (K) and pressure (atm)
%
Tr = 298.15; % K
Sr = 205.152e-3; % kJ/mol-K
p0 = 0.986923267; % atm
R = 8.314e-3; % kJ/mol-K
cF = 96.485; % 1eV = 96.485 kJ/mol --> conversion Factor
```

```

%
delG_O2 = -0.28*2; % Ref # 123 Average for O2
%
if T < 700
    % for Temp range 100 to 700 K
    A = 31.32234; % J/(mol-K) *****
http://webbook.nist.gov/cgi/cbook.cgi?ID=C7782447&Units=SI&Mask=1#Thermo-Gas
*****
B = -20.23531; % J/(mol-K^2)
C = 57.86644; % J/(mol-K^3)
D = -36.50624; % J/(mol-K^4)
E = -0.007374; % J-K/mol
F = -8.903471; % kJ/mol
G = 246.7945; % J/(mol-K)
else
    % for Temp range 700 to 2000 K
    A = 30.03235; % J/(mol-K) *****
http://webbook.nist.gov/cgi/cbook.cgi?ID=C7782447&Units=SI&Mask=1#Thermo-Gas
*****
B = 8.772972; % J/(mol-K^2)
C = -3.988133; % J/(mol-K^3)
D = 0.788313; % J/(mol-K^4)
E = -0.741599; % J-K/mol
F = -11.32468; % kJ/mol
G = 236.1663; % J/(mol-K)
end
%
t = T/1000; % T in K
% del_H = H(pr,T) - H(pr,Tr)
del_H = A*t +(B/2)*t^2 +(C/3)*t^3 +(D/4)*t^4 -E/t+F; % kJ/mol
%
% del_S = S(pr,T) - S(pr,Tr)
S = A*log(t) +B*t +(C/2)*t^2 +(D/3)*t^3-E/(2*t^2)+G; % J/mol-K
S = S/1000; % kJ/mol-K
del_S = S - Sr;
%
mu_O2_corr = delG_O2*cF + del_H - T*del_S - (T-Tr)*Sr + R*T*log(p/p0); % as p0 = 1 bar
end

```

BIBLIOGRAPHY

BIBLIOGRAPHY

- (1) Yadav, A. K.; Singh, R. K.; Singh, P. Fabrication of Lanthanum Ferrite Based Liquefied Petroleum Gas Sensor. *Sens. Actuators B Chem.* **2016**, 229, 25–30.
- (2) Brisotto, M.; Cernuschi, F.; Drago, F.; Lenardi, C.; Rosa, P.; Meneghini, C.; Merlini, M.; Rinaldi, C. High Temperature Stability of Ba_{0.5}Sr_{0.5}Co_{0.8}Fe_{0.2}O₃– δ and La_{0.6}Sr_{0.4}Co₁– y FeyO₃– δ Oxygen Separation Perovskite Membranes. *J. Eur. Ceram. Soc.* **2016**, 36 (7), 1679–1690.
- (3) Magyari-Köpe, B.; Park, S. G.; Lee, H.-D.; Nishi, Y. First Principles Calculations of Oxygen Vacancy-Ordering Effects in Resistance Change Memory Materials Incorporating Binary Transition Metal Oxides. *J. Mater. Sci.* **2012**, 47 (21), 7498–7514.
- (4) Baumann, F. S.; Fleig, J.; Cristiani, G.; Stuhlhofer, B.; Habermeier, H.-U.; Maier, J. Quantitative Comparison of Mixed Conducting SOFC Cathode Materials by Means of Thin Film Model Electrodes. *J. Electrochem. Soc.* **2007**, 154 (9), B931–B941.
- (5) Nicholas, J.; Highlights from the 2013 National Science Foundation Solid Oxide Fuel Cell Promise, Progress, and Priorities (SOFC-PPP) Workshop. *Electrochim. Soc. Interface* **2013**, No. Winter 2013, 49.
- (6) Yang, Q.; Burye, T. E.; Lunt, R. R.; Nicholas, J. D. In Situ Oxygen Surface Exchange Coefficient Measurements on Lanthanum Strontium Ferrite Thin Films via the Curvature Relaxation Method. *Solid State Ionics*. **2013**, 249–250 (0), 123–128.
- (7) Burye, T. E.; Tang, H.; Nicholas, J. D. The Effect of Precursor Solution Desiccation or Nano-Ceria Pre-Infiltration on Various La_{0.6}Sr_{0.4}FeyCo₁–YO₃– x Infiltrate Compositions. *J. Electrochem. Soc.* **2016**, 163 (9), F1017–F1022.
- (8) Celorio, V.; Bradley, K.; Weber, O. J.; Hall, S. R.; Fermín, D. J. Photoelectrochemical Properties of LaFeO₃ Nanoparticles. *ChemElectroChem* **2014**, 1 (10), 1667–1671.
- (9) Wachsman, E. D.; Lee, K. T. Lowering the Temperature of Solid Oxide Fuel Cells. *Science* **2011**, 334 (6058), 935–939.
- (10) Mogensen, M.; Nigel, S.; Geoff, T. Physical, Chemical and Electrochemical Properties of Pure and Doped Ceria. *Solid State Ionics*. **2000**, 129 (1–4), 63–94.
- (11) Yoo, J. Determination of the Equilibrium Oxygen Non-Stoichiometry and the Electrical Conductivity of La_{0.5}Sr_{0.5}FeO₃–X. *Solid State Ionics*. **2004**, 175 (1–4), 55–58.
- (12) Liu, Z.; Ding, D.; Liu, M.; Ding, X.; Chen, D.; Li, X.; Xia, C.; Liu, M. High-Performance, Ceria-Based Solid Oxide Fuel Cells Fabricated at Low Temperatures. *J. Power Sources* **2013**, 241, 454–459.

- (13) Dalslet, B.; Blennow, P.; Hendriksen, P. V.; Bonanos, N.; Lybye, D.; Mogensen, M. Assessment of Doped Ceria as Electrolyte. *J. Solid State Electrochem.* **2006**, *10* (8), 547–561.
- (14) Ruiz de Larramendi, I.; Ortiz-Vitoriano, N.; Acebedo, B.; Jimenez de Aberasturi, D.; Gil de Muro, I.; Arango, A.; Rodriguez-Castellon, E.; Ruiz de Larramendi, J. I.; Rojo, T. Pr-Doped Ceria Nanoparticles as Intermediate Temperature Ionic Conductors. *Int. J. Hydrot. Energy* **2011**, *36* (17), 10981–10990.
- (15) Spiridigliozi, L.; Biesuz, M.; Dell’Agli, G.; Bartolomeo, E. D.; Zurlo, F.; Sglavo, V. M. Microstructural and Electrical Investigation of Flash-Sintered Gd/Sm-Doped Ceria. *J. Mater. Sci.* **2017**, *52* (12), 7479–7488.
- (16) Liu, T.; Zhang, X.; Wang, X.; Yu, J.; Li, L. A Review of Zirconia-Based Solid Electrolytes. *Ionics* **2016**, *22* (12), 2249–2262.
- (17) Mizusaki, J.; Sasamoto, T.; Cannon, W. R.; Bowen, H. K. Electronic Conductivity, Seebeck Coefficient, and Defect Structure of La_{1-X}Sr_XFeO₃ (X=0.1, 0.25). *J. Am. Ceram. Soc.* **1983**, *66* (4), 247–252.
- (18) Berenov, A. V.; Atkinson, A.; Kilner, J. A.; Bucher, E.; Sitte, W. Oxygen Tracer Diffusion and Surface Exchange Kinetics in La_{0.6}Sr_{0.4}CoO_{3-δ}. *Solid State Ionics* **2010**, *181* (17–18), 819–826.
- (19) Grundy, A. N.; Hallstedt, B.; Gauckler, L. J. Assessment of the La–Sr–Mn–O System. *Calphad* **2004**, *28* (2), 191–201.
- (20) De Souza, R. A.; Kilner, J. A. Oxygen Transport in La_{1-x}Sr_xMn_{1-y}CoyO_{3±δ} Perovskites: Part I. Oxygen Tracer Diffusion. *Solid State Ionics* **1998**, *106* (3–4), 175–187.
- (21) Bansal, N. P.; Zhong, Z. Synthesis of Sm_{0.5}Sr_{0.5}CoO_{3-x} and La_{0.6}Sr_{0.4}CoO_{3-x} Nanopowders by Solution Combustion Process. In *Novel Processing of Ceramics and Composites*; Bansal, N. P., Singh, J. P., Smay, J. E., Ohji, T., Eds.; John Wiley & Sons, Inc.: Hoboken, NJ, USA, 2011; pp 21–32.
- (22) Ahmed, B.; Lee, S.-B.; Song, R.-H.; Lee, J.-W.; Lim, T.-H.; Park, S.-J. Development of Novel LSM/GDC Composite and Electrochemical Characterization of LSM/GDC Based Cathode-Supported Direct Carbon Fuel Cells. *J. Solid State Electrochem.* **2014**, *18* (2), 435–443.
- (23) Liu, M.; Ding, D.; Blinn, K.; Li, X.; Nie, L.; Liu, M. Enhanced Performance of LSCF Cathode Through Surface Modification. *Int. J. Hydrot. Energy* **2012**, *37* (10), 8613–8620.
- (24) Ritzmann, A. M.; Muñoz-García, A. B.; Pavone, M.; Keith, J. A.; Carter, E. A. Ab Initio DFT+U Analysis of Oxygen Vacancy Formation and Migration in La_{1-X}Sr_XFeO_{3-δ} = 0, 0.25, 0.50). *Chem. Mater.* **2013**, *25* (15), 3011–3019.
- (25) Cassir, M.; Gourba, E. Reduction in the Operating Temperature of Solid Oxide Fuel Cells—Potential Use in Transport Applications. *Ann. Chim. Sci. Matér.* **2001**, *26* (4), 49–58.

- (26) Steele, B. C. H.; Heinzel, A. Materials for Fuel-Cell Technologies. *Nature* **2001**, *414* (6861), 345–352.
- (27) Das, T.; Nicholas, J. D.; Qi, Y. Long-Range Charge Transfer and Oxygen Vacancy Interactions in Strontium Ferrite. *J. Mater. Chem. A* **2017**, *5* (9), 4493–4506.
- (28) Lee, Y.-L.; Morgan, D. Ab Initio and Empirical Defect Modeling of $\text{LaMnO}_3\pm\delta$ for Solid Oxide Fuel Cell Cathodes. *Phys. Chem. Chem. Phys.* **2012**, *14* (1), 290–302.
- (29) Kuklja, M. M.; Mastrikov, Y. A.; Jansang, B.; Kotomin, E. A. The Intrinsic Defects, Disorder, and Structural Stability of $\text{Ba}_x\text{Sr}_{1-x}\text{Co}_y\text{Fe}_{1-y}\text{O}_3-\delta$ Perovskite Solid Solutions. *J. Phys. Chem. C* **2012**, *116* (35), 18605–18611.
- (30) Kuklja, M. M.; Kotomin, E. A.; Merkle, R.; Mastrikov, Y. A.; Maier, J. Combined Theoretical and Experimental Analysis of Processes Determining Cathode Performance in Solid Oxide Fuel Cells. *Phys. Chem. Chem. Phys.* **2013**, *15* (15), 5443.
- (31) Das, T.; Nicholas, J. D.; Qi, Y. First-Principles Studies of Oxygen Vacancy Interactions and Their Impact on Oxygen Migration in Lanthanum Strontium Ferrite. *ECS Trans.* **2017**, *78* (1), 2807–2814.
- (32) Hodges, J. P.; Short, S.; Jorgensen, J. D.; Xiong, X.; Dabrowski, B.; Mini, S. M.; Kimball, C. W. Evolution of Oxygen-Vacancy Ordered Crystal Structures in the Perovskite Series $\text{Sr}_n\text{Fe}_n\text{O}_{3n-1}$ ($n=2, 4, 8$, and ∞), and the Relationship to Electronic and Magnetic Properties. *J. Solid State Chem.* **2000**, *151* (2), 190–209.
- (33) Schmidt, M.; Hofmann, M.; Campbell, S. J. Magnetic Structure of Strontium Ferrite $\text{Sr}_4\text{Fe}_4\text{O}_{11}$. *J. Phys. Condens. Matter* **2003**, *15* (50), 8691.
- (34) Vidya, R.; Ravindran, P.; Fjellvåg, H.; Kjekshus, A. Spin- and Charge-Ordering in Oxygen-Vacancy-Ordered Mixed-Valence $\text{Sr}_4\text{Fe}_4\text{O}_{11}$. *Phys. Rev. B* **2006**, *74* (5), 054422.
- (35) Adler, P. Comment on ``Spin and Charge Ordering in Oxygen Vacancy Ordered Mixed-Valence $\text{Sr}_4\text{Fe}_4\text{O}_{11}$. *Phys. Rev. B* **2008**, *77* (13), 136401.
- (36) Ravindran, P.; Vidya, R.; Fjellvåg, H.; Kjekshus, A. Reply to ``Comment on `Spin- and Charge-Ordering in Oxygen-Vacancy-Ordered Mixed-Valence $\text{Sr}_4\text{Fe}_4\text{O}_{11}$. *Phys. Rev. B* **2008**, *77* (13), 136402.
- (37) Hombo, J.; Matsumoto, Y.; Kawano, T. Electrical Conductivities of $\text{SrFeO}_3-\delta$ and $\text{BaFeO}_3-\delta$ Perovskites. *J. Solid State Chem.* **1990**, *84* (1), 138–143.
- (38) Kharton, V.; Kovalevsky, A.; Tsipis, E.; Viskup, A.; Naumovich, E.; Jurado, J.; Frade, J. Mixed Conductivity and Stability of A-Site-Deficient $\text{Sr}(\text{Fe},\text{Ti})\text{O}_3-\delta$; Perovskites. *J. Solid State Electrochem.* **2002**, *7* (1), 30–36.

- (39) Li, Y.; Kraynis, O.; Kas, J.; Weng, T.-C.; Sokaras, D.; Zacharowicz, R.; Lubomirsky, I.; Frenkel, A. I. Geometry of Electromechanically Active Structures in Gadolinium - Doped Cerium Oxides. *AIP Adv.* **2016**, *6* (5), 055320.
- (40) Marrocchelli, D.; Bishop, S. R.; Tuller, H. L.; Yildiz, B. Understanding Chemical Expansion in Non-Stoichiometric Oxides: Ceria and Zirconia Case Studies. *Adv. Funct. Mater.* **2012**, *22* (9), 1958–1965.
- (41) Er, D.; Li, J.; Cargnello, M.; Fornasiero, P.; Gorte, R. J.; Shenoy, V. B. A Model to Determine the Chemical Expansion in Non-Stoichiometric Oxides Based on the Elastic Force Dipole. *J. Electrochem. Soc.* **2014**, *161* (11), F3060–F3064.
- (42) James, C.; Wu, Y.; Sheldon, B.; Qi, Y. Computational Analysis of Coupled Anisotropic Chemical Expansion in $\text{Li}_2\text{-XMnO}_3\text{-}\delta$. *MRS Adv.* **2016**, *1* (15), 1037–1042.
- (43) Ishigaki, T.; Yamauchi, S.; Kishio, K.; Mizusaki, J.; Fueki, K. Diffusion of Oxide Ion Vacancies in Perovskite-Type Oxides. *J. Solid State Chem.* **1988**, *73* (1), 179–187.
- (44) Takeda, Y.; Kanno, K.; Takada, T.; Yamamoto, O.; Takano, M.; Nakayama, N.; Bando, Y. Phase Relation in the Oxygen Nonstoichiometric System, SrFeO_x ($2.5 \leq x \leq 3.0$). *J. Solid State Chem.* **1986**, *63* (2), 237–249.
- (45) Choi, S.; Yoo, S.; Kim, J.; Park, S.; Jun, A.; Sengodan, S.; Kim, J.; Shin, J.; Jeong, H. Y.; Choi, Y.; Kim, G.; Liu, M. Highly Efficient and Robust Cathode Materials for Low-Temperature Solid Oxide Fuel Cells: $\text{PrBa}_0.5\text{Sr}_0.5\text{Co}_{2-x}\text{Fe}_x\text{O}_{5+\delta}$. *Sci. Rep.* **2013**, *3*.
- (46) Kharton, V. V.; Kovalevsky, A. V.; Patrakeev, M. V.; Tsipis, E. V.; Viskup, A. P.; Kolotygin, V. A.; Yaremchenko, A. A.; Shaula, A. L.; Kiselev, E. A.; Waerenborgh, J. C. Oxygen Nonstoichiometry, Mixed Conductivity, and Mössbauer Spectra of $\text{Ln}_0.5\text{A}_0.5\text{FeO}_3\text{-}\delta$ ($\text{Ln} = \text{La-Sm}$, $\text{A} = \text{Sr, Ba}$): Effects of Cation Size. *Chem. Mater.* **2008**, *20* (20), 6457–6467.
- (47) Burye, T. E.; Nicholas, J. D. Nano-Ceria Pre-Infiltration Improves $\text{La}_0.6\text{Sr}_0.4\text{Co}_0.8\text{Fe}_0.2\text{O}_{3-x}$ Infiltrated Solid Oxide Fuel Cell Cathode Performance. *J. Power Sources* **2015**, *300*, 402–412.
- (48) Pavone, M.; Muñoz-García, A. B.; Ritzmann, A. M.; Carter, E. A. First-Principles Study of Lanthanum Strontium Manganite: Insights into Electronic Structure and Oxygen Vacancy Formation. *J. Phys. Chem. C* **2014**, *118* (25), 13346–13356.
- (49) Muñoz-García, A. B.; Pavone, M.; Ritzmann, A. M.; Carter, E. A. Oxide Ion Transport in $\text{Sr}_2\text{Fe}_1.5\text{Mo}_0.5\text{O}_6\text{-}\delta$, a Mixed Ion-Electron Conductor: New Insights From First Principles Modeling. *Phys. Chem. Chem. Phys.* **2013**, *15* (17), 6250.
- (50) Muñoz-García, A. B.; Ritzmann, A. M.; Pavone, M.; Keith, J. A.; Carter, E. A. Oxygen Transport in Perovskite-Type Solid Oxide Fuel Cell Materials: Insights from Quantum Mechanics. *Acc. Chem. Res.* **2014**, *47* (11), 3340–3348.

- (51) Burbano, M.; Norberg, S. T.; Hull, S.; Eriksson, S. G.; Marrocchelli, D.; Madden, P. A.; Watson, G. W. Oxygen Vacancy Ordering and the Conductivity Maximum in Y₂O₃-Doped CeO₂. *Chem. Mater.* **2012**, *24* (1), 222–229.
- (52) Kittel, C. *Introduction to Solid State Physics*, 8 edition.; Wiley: Hoboken, NJ, 2004.
- (53) Ritzmann, A. M.; Pavone, M.; Muñoz-García, A. B.; Keith, J. A.; Carter, E. A. Ab Initio DFT+U Analysis of Oxygen Transport in LaCoO₃: The Effect of Co³⁺ Magnetic States. *J Mater Chem A* **2014**, *2* (21), 8060–8074.
- (54) Rothschild, A.; Meneskou, W.; Tuller, H. L.; Ivers-Tiffée, E. Electronic Structure, Defect Chemistry, and Transport Properties of SrTi_{1-x}FexO_{3-y} Solid Solutions. *Chem. Mater.* **2006**, *18* (16), 3651–3659.
- (55) Mastrikov, Y. A.; Merkle, R.; Kotomin, E. A.; Kuklja, M. M.; Maier, J. Formation and Migration of Oxygen Vacancies in La_{1-x}SrxCo_{1-y}FeyO_{3-δ} Perovskites: Insight from Ab Initio Calculations and Comparison with Ba_{1-x}SrxCo_{1-y}FeyO_{3-δ}. *Phys Chem Chem Phys* **2013**, *15* (3), 911–918.
- (56) Gryaznov, D.; Finnis, M. W.; Evarestov, R. A.; Maier, J. Oxygen Vacancy Formation Energies in Sr-Doped Complex Perovskites: Ab Initio Thermodynamic Study. *Solid State Ionics* **2014**, *254*, 11–16.
- (57) Vashuk, V. V.; Kokhanovskii, L. V.; Yushkevich, I. I. Electrical Conductivity and Oxygen Stoichiometry of SrFeO_{3-δ}. *Neorganicheskie Mater.* **2000**, *36* (1), 90–96.
- (58) Gao, M.; Li, C.-J.; Li, C.-X.; Yang, G.-J.; Fan, S.-Q. Microstructure, Oxygen Stoichiometry and Electrical Conductivity of Flame-Sprayed Sm_{0.7}Sr_{0.3}CoO_{3-δ}. *J. Power Sources* **2009**, *191* (2), 275–279.
- (59) Lankhorst, M. H. R.; Bouwmeester, H. J. M. Determination of Oxygen Nonstoichiometry and Diffusivity in Mixed Conducting Oxides by Oxygen Coulometric Titration II. Oxygen Nonstoichiometry and Defect Model for La_{0.8}Sr_{0.2}CoO₃-Delta. *J. Electrochem. Soc.* **1997**, *144* (4), 1268–1273.
- (60) Ravindran, P.; Vidya, R.; Fjellvåg, H.; Kjekshus, A. Validity of Bond-Length and Mössbauer Parameters to Assign Oxidation States in Multicomponent Oxides: Case Study of Sr₄Fe₄O₁₁. *Phys. Rev. B* **2008**, *77* (13), 134448.
- (61) Mizusaki, J.; Yoshihiro, M.; Yamauchi, S.; Fueki, K. Nonstoichiometry and Defect Structure of the Perovskite-Type Oxides La_{1-x}SrxFeO_{3-δ}. *J. Solid State Chem.* **1985**, *58* (2), 257–266.
- (62) Patrakeev, M. V.; Bahteeva, J. A.; Mitberg, E. B.; Leonidov, I. A.; Kozhevnikov, V. L.; Poeppelmeier, K. R. Electron/Hole and Ion Transport in La_{1-x}SrxFeO_{3-δ}. *J. Solid State Chem.* **2003**, *172* (1), 219–231.

- (63) Bahteeva, J. A.; Leonidov, I. A.; Patrakeev, M. V.; Mitberg, E. B.; Kozhevnikov, V. L.; Poeppelmeier, K. R. High-Temperature Ion Transport in $\text{La}_{1-x}\text{Sr}_x\text{FeO}_3-\delta$. *J. Solid State Electrochem.* **2004**, *8* (9), 578–584.
- (64) Dann, S. E.; Currie, D. B.; Weller, M. T.; Thomas, M. F.; Al-Rawwas, A. D. The Effect of Oxygen Stoichiometry on Phase Relations and Structure in the System $\text{La}_{1-x}\text{Sr}_x\text{FeO}_3-\delta$ ($0 \leq x \leq 1$, $0 \leq \delta \leq 0.5$). *J. Solid State Chem.* **1994**, *109* (1), 134–144.
- (65) Fosdal, A.; Menon, M.; Wærnhus, I.; Wiik, K.; Einarsrud, M.-A.; Grande, T. Crystal Structure and Thermal Expansion of $\text{La}_{1-x}\text{Sr}_x\text{FeO}_3-\delta$ Materials. *J. Am. Ceram. Soc.* **2004**, *87* (10), 1952–1958.
- (66) Taylor, F. H.; Buckeridge, J.; Catlow, C. R. A. Defects and Oxide Ion Migration in the Solid Oxide Fuel Cell Cathode Material LaFeO_3 . *Chem. Mater.* **2016**, *28* (22), 8210–8220.
- (67) Landau, L. D. Über die Bewegung der Elektronen in Kristallgitter. *Phys Z Sowjetunion* **1933**, *3*, 644–645.
- (68) Jung, W.-H. Transport Mechanisms in $\text{La}_{0.7}\text{Sr}_{0.3}\text{FeO}_3$: Evidence for Small Polaron Formation. *Phys. B Condens. Matter* **2001**, *299* (1), 120–123.
- (69) Castleton, C. W. M.; Lee, A. L.; Kullgren, J.; Hermansson, K. Description of Polarons in Ceria Using Density Functional Theory. *J. Phys. Conf. Ser.* **2014**, *526* (1), 012002.
- (70) Das, T.; Nicholas, J. D.; Qi, Y. In Preparation: Anisotropic Chemical Expansion in Nonstoichiometric Ceria. **2017**.
- (71) Taylor, D. D.; Schreiber, N. J.; Levitas, B. D.; Xu, W.; Whitfield, P. S.; Rodriguez, E. E. Oxygen Storage Properties of $\text{La}_{1-x}\text{Sr}_x\text{FeO}_3-\delta$ for Chemical-Looping Reactions—An In Situ Neutron and Synchrotron X-Ray Study. *Chem. Mater.* **2016**, *28* (11), 3951–3960.
- (72) Ren, Y.; Küngas, R.; Gorte, R. J.; Deng, C. The Effect of A-Site Cation (Ln=La, Pr, Sm) on the Crystal Structure, Conductivity and Oxygen Reduction Properties of Sr-Doped Ferrite Perovskites. *Solid State Ionics* **2012**, *212*, 47–54.
- (73) Bishop, S. R. Chemical Expansion of Solid Oxide Fuel Cell Materials: A Brief Overview. *Acta Mech. Sin.* **2013**, *29* (3), 312–317.
- (74) Bishop, S. R.; Stefanik, T. S.; Tuller, H. L. Electrical Conductivity and Defect Equilibria of $\text{Pr}_{0.1}\text{Ce}_{0.9}\text{O}_2-\delta$. *Phys. Chem. Chem. Phys.* **2011**, *13* (21), 10165.
- (75) Korobko, R.; Patlolla, A.; Kossov, A.; Wachtel, E.; Tuller, H. L.; Frenkel, A. I.; Lubomirsky, I. Giant Electrostriction in Gd-Doped Ceria. *Adv. Mater.* **2012**, *24* (43), 5857–5861.
- (76) Nicholas, J. D.; Qi, Y.; Bishop, S. R.; Mukherjee, P. P. Introduction to Mechano-Electro-Chemical Coupling in Energy Related Materials and Devices. *J. Electrochem. Soc.* **2014**, *161* (11), Y11–Y12.

- (77) Kresse, G.; Furthmüller, J. Efficient Iterative Schemes for Ab Initio Total-Energy Calculations Using a Plane-Wave Basis Set. *Phys. Rev. B* **1996**, *54* (16), 11169–11186.
- (78) Kresse, G.; Joubert, D. From Ultrasoft Pseudopotentials to the Projector Augmented-Wave Method. *Phys. Rev. B* **1999**, *59* (3), 1758–1775.
- (79) Blöchl, P. E. Projector Augmented-Wave Method. *Phys. Rev. B* **1994**, *50* (24), 17953–17979.
- (80) Perdew, J. P.; Burke, K.; Ernzerhof, M. Generalized Gradient Approximation Made Simple. *Phys. Rev. Lett.* **1996**, *77* (18), 3865–3868.
- (81) Perdew, J. P.; Burke, K.; Ernzerhof, M. Generalized Gradient Approximation Made Simple [Phys. Rev. Lett. *77*, 3865 (1996)]. *Phys. Rev. Lett.* **1997**, *78* (7), 1396–1396.
- (82) Terakura, K.; Oguchi, T.; Williams, A. R.; Kübler, J. Band Theory of Insulating Transition-Metal Monoxides: Band-Structure Calculations. *Phys. Rev. B* **1984**, *30* (8), 4734–4747.
- (83) Anisimov, V. I.; Zaanen, J.; Andersen, O. K. Band Theory and Mott Insulators: Hubbard U Instead of Stoner I. *Phys. Rev. B* **1991**, *44* (3), 943–954.
- (84) Blöchl, P. E.; Jepsen, O.; Andersen, O. K. Improved Tetrahedron Method for Brillouin-Zone Integrations. *Phys. Rev. B* **1994**, *49* (23), 16223–16233.
- (85) Lee, C.-W.; Behera, R. K.; Wachsman, E. D.; Phillpot, S. R.; Sinnott, S. B. Stoichiometry of the LaFeO₃ (010) Surface Determined from First-Principles and Thermodynamic Calculations. *Phys. Rev. B* **2011**, *83* (11), 115418.
- (86) Marezio, M.; Dernier, P. D. The Bond Lengths in LaFeO₃. *Mater. Res. Bull.* **1971**, *6* (1), 23–29.
- (87) Shimony, U.; Knudsen, J. M. Mössbauer Studies on Iron in the Perovskites La_{1-X}Sr_XFeO₃ (0<~x<~1). *Phys. Rev.* **1966**, *144* (1), 361–366.
- (88) Tang, W.; Sanville, E.; Henkelman, G. A Grid-Based Bader Analysis Algorithm without Lattice Bias. *J. Phys. Condens. Matter* **2009**, *21* (8), 084204.
- (89) Bouibes, A.; Zaoui, A. High-Pressure Polymorphs of ZnCO₃: Evolutionary Crystal Structure Prediction. *Sci. Rep.* **2014**, *4*.
- (90) Dudarev, S. L.; Botton, G. A.; Savrasov, S. Y.; Humphreys, C. J.; Sutton, A. P. Electron-Energy-Loss Spectra and the Structural Stability of Nickel Oxide: An LSDA+U Study. *Phys. Rev. B* **1998**, *57* (3), 1505–1509.
- (91) Jain, A.; Hautier, G.; Ong, S. P.; Moore, C. J.; Fischer, C. C.; Persson, K. A.; Ceder, G. Formation Enthalpies by Mixing GGA and GGA + U Calculations. *Phys. Rev. B* **2011**, *84* (4), 045115.

- (92) Wang, L.; Maxisch, T.; Ceder, G. Oxidation Energies of Transition Metal Oxides within the GGA+U Framework. *Phys. Rev. B* **2006**, *73* (19), 195107.
- (93) Ceder, G.; Hautier, G.; Jain, A.; Ong, S. P. Recharging Lithium Battery Research with First-Principles Methods. *MRS Bull.* **2011**, *36* (3), 185–191.
- (94) Anisimov, V. I.; Aryasetiawan, F.; Lichtenstein, A. I. First-Principles Calculations of the Electronic Structure and Spectra of Strongly Correlated Systems: The LDA+ U Method. *J. Phys. Condens. Matter* **1997**, *9* (4), 767.
- (95) Mosey, N. J.; Liao, P.; Carter, E. A. Rotationally Invariant Ab Initio Evaluation of Coulomb and Exchange Parameters for DFT+U Calculations. *J. Chem. Phys.* **2008**, *129* (1), 014103.
- (96) Akriche, A.; Bouafia, H.; Hiadsi, S.; Abidri, B.; Sahli, B.; Elchikh, M.; Timaoui, M. A.; Djebour, B. First-Principles Study of Mechanical, Exchange Interactions and the Robustness in Co₂MnSi Full Heusler Compounds. *J. Magn. Magn. Mater.* **2017**, *422*, 13–19.
- (97) Bentouaf, A.; Mebsout, R.; Rached, H.; Amari, S.; Reshak, A. H.; Aïssa, B. Theoretical Investigation of the Structural, Electronic, Magnetic and Elastic Properties of Binary Cubic C₁₅-Laves Phases TbX₂ (X = Co and Fe). *J. Alloys Compd.* **2016**, *689*, 885–893.
- (98) Gallagher, P. K.; MacChesney, J. B. Mössbauer Effect in the System Sr_{1-x}LaxFeO₃. *Symp Faraday Soc* **1967**, *1* (0), 40–47.
- (99) Gryaznov, D.; Heifets, E.; Kotomin, E. The First-Principles Treatment of the Electron-Correlation and Spin-orbital Effects in Uranium Mononitride Nuclear Fuels. *Phys. Chem. Chem. Phys.* **2012**, *14* (13), 4482–4490.
- (100) Koehler, W. C.; Wollan, E. O. Neutron-Diffraction Study of the Magnetic Properties of Perovskite-like Compounds LaBO₃. *J. Phys. Chem. Solids* **1957**, *2* (2), 100–106.
- (101) Shein, I. R.; Shein, K. I.; Kozhevnikov, V. L.; Ivanovskii, A. L. Band Structure and the Magnetic and Elastic Properties of SrFeO₃ and LaFeO₃ Perovskites. *Phys. Solid State* **2005**, *47* (11), 2082–2088.
- (102) Zhang, Q.; Yunoki, S. A First-Principles Study for Electronic and Magnetic Properties of LaFeO₃/LaCrO₃ Superlattices. *J. Phys. Conf. Ser.* **2012**, *400* (3), 032126.
- (103) Hoffmann, A.; Seo, J. W.; Fitzsimmons, M. R.; Siegwart, H.; Fompeyrine, J.; Locquet, J.-P.; Dura, J. A.; Majkrzak, C. F. Induced Magnetic Moments at a Ferromagnet-Antiferromagnet Interface. *Phys. Rev. B* **2002**, *66* (22), 220406.
- (104) Takano, M.; Takeda, Y. Electronic State of Fe⁴⁺ Ions in Perovskite-Type Oxides. *Bull. Inst. Chem. Res. Kyoto Univ.* **1983**, *61* (5–6), 406–425.
- (105) Reehuis, M.; Ulrich, C.; Maljuk, A.; Niedermayer, C.; Ouladdiaf, B.; Hoser, A.; Hofmann, T.; Keimer, B. Neutron Diffraction Study of Spin and Charge Ordering in SrFeO₃–δ. *Phys. Rev. B* **2012**, *85* (18), 184109.

- (106) Xiao, G.; Liu, Q.; Wang, S.; Komvokis, V. G.; Amiridis, M. D.; Heyden, A.; Ma, S.; Chen, F. Synthesis and Characterization of Mo-Doped SrFeO₃- δ as Cathode Materials for Solid Oxide Fuel Cells. *J. Power Sources* **2012**, *202*, 63–69.
- (107) Takeda, T; Komura, S; Watanabe, N. In *FERRITES: Proc. Int. Conf. Sept.-Oct. 1980*; Center for Academic Publication, Japan: Japan; p 385.
- (108) Watanabe, H.; Oda, H.; Nakamura, E.; Yamaguchi, Y.; Takei, H. In *FERRITES: Proc. Int. Conf. Sept.-Oct. 1980*; Center for Academic Publication, Japan: Japan; p 381.
- (109) Takeda, T.; Watanabe, T.; Komura, S.; Fujii, H. Magnetic Properties of SrFe_{1-X}CoxO₃. *J. Phys. Soc. Jpn.* **1987**, *56* (2), 731–735.
- (110) Muñoz-García, A. B.; Pavone, M.; Carter, E. A. Effect of Antisite Defects on the Formation of Oxygen Vacancies in Sr₂FeMoO₆: Implications for Ion and Electron Transport. *Chem. Mater.* **2011**, *23* (20), 4525–4536.
- (111) Yang, Z.; Huang, Z.; Ye, L.; Xie, X. Influence of Parameters U and J in the LSDA+U Method on Electronic Structure of the Perovskites LaMO₃ (M=Cr,Mn,Fe,Co,Ni). *Phys. Rev. B* **1999**, *60* (23), 15674–15682.
- (112) Tsujimoto, Y.; Tassel, C.; Hayashi, N.; Watanabe, T.; Kageyama, H.; Yoshimura, K.; Takano, M.; Ceretti, M.; Ritter, C.; Paulus, W. Infinite-Layer Iron Oxide with a Square-Planar Coordination. *Nature* **2007**, *450* (7172), 1062–1065.
- (113) Wißmann, S.; Becker, K. D. Localization of Electrons in Nonstoichiometric SrFeO₃ – Δ . *Solid State Ionics*. **1996**, *85* (1–4), 279–283.
- (114) David Sholl; Janice A Steckel. *Density Functional Theory: A Practical Introduction*, April 2009.; WILEY, 2009.
- (115) Giannozzi, P.; Car, R.; Scoles, G. Oxygen Adsorption on Graphite and Nanotubes. *J. Chem. Phys.* **2003**, *118* (3), 1003–1006.
- (116) Herzberg, G.; Huber, K. P. *Molecular Spectra and Molecular Structure*; Van Nostrand Reinhold: New York ;London, 1979.
- (117) Greg Mills, K. W. J. Nudged Elastic Band Method for Finding Minimum Energy Paths of Transitions. **1998**.
- (118) Sheppard, D.; Terrell, R.; Henkelman, G. Optimization Methods for Finding Minimum Energy Paths. *J. Chem. Phys.* **2008**, *128* (13), 134106.
- (119) Tucker, M. C. Progress in Metal-Supported Solid Oxide Fuel Cells: A Review. *J. Power Sources* **2010**, *195* (15), 4570–4582.

- (120) Henkelman, G.; Uberuaga, B. P.; Jónsson, H. A Climbing Image Nudged Elastic Band Method for Finding Saddle Points and Minimum Energy Paths. *J. Chem. Phys.* **2000**, *113* (22), 9901–9904.
- (121) Zhang, W.; Smith, J. R.; Wang, X.-G. Thermodynamics from Ab Initio Computations. *Phys. Rev. B* **2004**, *70* (2), 024103.
- (122) Hine, N. D. M.; Frensch, K.; Foulkes, W. M. C.; Finnis, M. W. Supercell Size Scaling of Density Functional Theory Formation Energies of Charged Defects. *Phys. Rev. B* **2009**, *79* (2), 024112.
- (123) Lee, Y.-L.; Kleis, J.; Rossmeisl, J.; Morgan, D. Ab Initio Energetics of LaBO₃(001) (B=Mn, Fe, Co, and Ni) for Solid Oxide Fuel Cell Cathodes. *Phys. Rev. B* **2009**, *80* (22), 224101.
- (124) Reuter, K.; Scheffler, M. Composition, Structure, and Stability of RuO₂(110) as a Function of Oxygen Pressure. *Phys. Rev. B* **2001**, *65* (3), 035406.
- (125) Lide, D. R. *CRC Handbook of Chemistry and Physics*; CRC Pr: Boca Raton, 1994.
- (126) Chase, M. W. NIST-JANAF Thermochemical Tables, Fourth Edition. *J. Phys. Chem. Ref. Data, Monograph 9* **1998**, 1–1951.
- (127) *JANAF Thermochemical Tables, 2nd Edition*, 2nd edition.; Stull, D. R., Prophet, H., Eds.; National Bureau of Standards U.S, 1971.
- (128) Xi, L.; Qiu, Y.; Zheng, S.; Shi, X.; Yang, J.; Chen, L.; Singh, D. J.; Yang, J.; Zhang, W. Complex Doping of Group 13 Elements In and Ga in Caged Skutterudite CoSb₃. *Acta Mater.* **2015**, *85*, 112–121.
- (129) Loftager, S.; García-Lastra, J. M.; Vegge, T. A Density Functional Theory Study of the Ionic and Electronic Transport Mechanisms in LiFeBO₃ Battery Electrodes. *J. Phys. Chem. C* **2016**, *120* (33), 18355–18364.
- (130) Mantina, M.; Chen, L. Q.; Liu, Z. K. Predicting Diffusion Coefficients from First Principles via Eyring’s Reaction Rate Theory. *Defect Diffus. Forum* **2009**, *294*, 1–13.
- (131) Mantina, M.; Wang, Y.; Chen, L. Q.; Liu, Z. K.; Wolverton, C. First Principles Impurity Diffusion Coefficients. *Acta Mater.* **2009**, *57* (14), 4102–4108.
- (132) Compaan, K.; Haven, Y. Correlation Factors for Diffusion in Solids. *Trans. Faraday Soc.* **1956**, *52* (0), 786–801.
- (133) Fabris, S.; de Gironcoli, S.; Baroni, S.; Vicario, G.; Balducci, G. Taming Multiple Valency with Density Functionals: A Case Study of Defective Ceria. *Phys. Rev. B* **2005**, *71* (4), 041102.

- (134) Chen, L.-J.; Tang, Y.; Cui, L.; Ouyang, C.; Shi, S. Charge Transfer and Formation of Ce³⁺ upon Adsorption of Metal Atom M (M = Cu, Ag, Au) on CeO₂ (100) Surface. *J. Power Sources* **2013**, *234*, 69–81.
- (135) Balaji Gopal, C.; García-Melchor, M.; Lee, S. C.; Shi, Y.; Shavorskiy, A.; Monti, M.; Guan, Z.; Sinclair, R.; Bluhm, H.; Vojvodic, A.; Chueh, W. C. Equilibrium Oxygen Storage Capacity of Ultrathin CeO₂- δ Depends Non-Monotonically on Large Biaxial Strain. *Nat. Commun.* **2017**, *8*, 15360.
- (136) Scavini, M.; Coduri, M.; Allieta, M.; Brunelli, M.; Ferrero, C. Probing Complex Disorder in Ce_{1-x}Gd_xO_{2-x/2} Using the Pair Distribution Function Analysis. *Chem. Mater.* **2012**, *24* (7), 1338–1345.
- (137) Tang, Y.; Zhang, H.; Cui, L.; Ouyang, C.; Shi, S.; Tang, W.; Li, H.; Lee, J.-S.; Chen, L. First-Principles Investigation on Redox Properties of M-Doped CeO₂ (M = Mn, Pr, Sn, Zr). *Phys. Rev. B* **2010**, *82* (12).
- (138) Esch, F.; Fabris, S.; Zhou, L.; Montini, T.; Africh, C.; Fornasiero, P.; Comelli, G.; Rosei, R. Electron Localization Determines Defect Formation on Ceria Substrates. *Science* **2005**, *309* (5735), 752–755.
- (139) Nolan, M.; Fearon, J.; Watson, G. Oxygen Vacancy Formation and Migration in Ceria. *Solid State Ionics*. **2006**, *177* (35–36), 3069–3074.
- (140) Tang, Y.; Zhang, H.; Cui, L.; Ouyang, C.; Shi, S.; Tang, W.; Li, H.; Chen, L. Electronic States of Metal (Cu, Ag, Au) Atom on CeO₂(111) Surface: The Role of Local Structural Distortion. *J. Power Sources* **2012**, *197*, 28–37.
- (141) Castleton, C. W. M.; Kullgren, J.; Hermansson, K. Tuning LDA+U for Electron Localization and Structure at Oxygen Vacancies in Ceria. *J. Chem. Phys.* **2007**, *127* (24), 244704.
- (142) Takeda, T.; Yamaguchi, Y.; Watanabe, H. Magnetic Structure of SrFeO₃. *J. Phys. Soc. Jpn.* **1972**, *33* (4), 967–969.
- (143) Yang, J. B.; Yelon, W. B.; James, W. J.; Chu, Z.; Kornecki, M.; Xie, Y. X.; Zhou, X. D.; Anderson, H. U.; Joshi, A. G.; Malik, S. K. Crystal Structure, Magnetic Properties, and Mössbauer Studies of La_{0.6}Sr_{0.4}FeO₃- δ Prepared by Quenching in Different Atmospheres. *Phys. Rev. B* **2002**, *66* (18).
- (144) Seo, J. W.; Fullerton, E. E.; Nolting, F.; Scholl, A.; Fompeyrine, J.; Locquet, J.-P. Antiferromagnetic LaFeO₃ Thin Films and Their Effect on Exchange Bias. *J. Phys. Condens. Matter* **2008**, *20* (26), 264014.
- (145) Haas, O.; Vogt, U. F.; Soltmann, C.; Braun, A.; Yoon, W.-S.; Yang, X. Q.; Graule, T. The Fe K-Edge X-Ray Absorption Characteristics of La_{1-x}Sr_xFeO₃- δ Prepared by Solid State Reaction. *Mater. Res. Bull.* **2009**, *44* (6), 1397–1404.

- (146) Arima, T.; Tokura, Y.; Torrance, J. B. Variation of Optical Gaps in Perovskite-Type 3d Transition-Metal Oxides. *Phys. Rev. B* **1993**, *48* (23), 17006–17009.
- (147) Galakhov, V. R.; Kurmaev, E. Z.; Kuepper, K.; Neumann, M.; McLeod, J. A.; Moewes, A.; Leonidov, I. A.; Kozhevnikov, V. L. Valence Band Structure and X-Ray Spectra of Oxygen-Deficient Ferrites SrFeO_x. *J. Phys. Chem. C* **2010**, *114* (11), 5154–5159.
- (148) Waerenborgh, J. C.; Tsipis, E. V.; Auckett, J. E.; Ling, C. D.; Kharton, V. V. Magnetic Structure of Sr₂Fe₂O₅ Brownmillerite by Single-Crystal Mössbauer Spectroscopy. *J. Solid State Chem.* **2013**, *205*, 5–9.
- (149) Haavik, C.; Atake, T.; Stølen, S. On the Enthalpic Contribution to the Redox Energetics of SrFeO₃–δ. *Phys. Chem. Chem. Phys.* **2002**, *4* (6), 1082–1087.
- (150) Greaves, C.; Jacobson, A. J.; Tofield, B. C.; Fender, B. E. F. A Powder Neutron Diffraction Investigation of the Nuclear and Magnetic Structure of Sr₂Fe₂O₅. *Acta Crystallogr. B* **1975**, *31* (3), 641–646.
- (151) Nakamura, S.; Iida, S. New Data on Electrical Properties and Antiferromagnetism of Highly Oxidized Perovskite SrFeO_x (2.5 < x < 3.0). *Jpn. J. Appl. Phys.* **1995**, *34* (Part 2, No. 3A), L291–L293.
- (152) Okube, M.; Furukawa, Y.; Yoshiasa, A.; Hashimoto, T.; Sugahara, M.; Nakatsuka, A. Oxidation State and Effective Pair Potential of Fe 4+ Ions in Perovskite-Type SrFeO₃ Annealed under High Oxygen Pressure. *J. Phys. Conf. Ser.* **2008**, *121* (9), 092004.
- (153) Williams, G. V. M.; Hemery, E. K.; McCann, D. Magnetic and Transport Properties of SrFeO_x. *Phys. Rev. B* **2009**, *79* (2), 024412.
- (154) Wang, Q.-B.; Zhou, C.; Wu, J.; Lü, T.; He, K.-H. GGA+U Study of the Electronic and Optical Properties of Hexagonal BN Phase ZnO Under Pressure. *Comput. Mater. Sci.* **2015**, *102*, 196–201.
- (155) Fuks, D.; Mastrikov, Y.; Kotomin, E.; Maier, J. Ab Initio Thermodynamic Study of (Ba,Sr)(Co,Fe)O₃ Perovskite Solid Solutions for Fuel Cell Applications. *J. Mater. Chem. A* **2013**, *1* (45), 14320.
- (156) Cheng, J.; Navrotsky, A.; Zhou, X.-D.; Anderson, H. U. Thermochemistry of La_{1-x}Sr_xFeO₃–δ Solid Solutions (0.0 ≤ x ≤ 1.0, 0.0 ≤ δ ≤ 0.5). *Chem. Mater.* **2005**, *17* (8), 2197–2207.
- (157) MacChesney, J. B.; Sherwood, R. C.; Potter, J. F. Electric and Magnetic Properties of the Strontium Ferrates. *J. Chem. Phys.* **1965**, *43* (6), 1907–1913.
- (158) Mizusaki, J.; Okayasu, M.; Yamauchi, S.; Fueki, K. Nonstoichiometry and Phase Relationship of the SrFeO_{2.5}-SrFeO₃ System at High Temperature. *J. Solid State Chem.* **1992**, *99* (1), 166–172.

- (159) Navrotsky, A. Energetics and Crystal Chemical Systematics among Ilmenite, Lithium Niobate, and Perovskite Structures. *Chem. Mater.* **1998**, *10* (10), 2787–2793.
- (160) Das, T.; Nicholas, J. D.; Qi, Y. Polaron Size and Shape Effects on Oxygen Vacancy Interactions in Lanthanum Strontium Ferrite. *JMCA submitted* **2017**.
- (161) Kawakami, T.; Nasu, S.; Sasaki, T.; Morimoto, S.; Endo, S.; Kawasaki, S.; Takano, M. Charge Disproportionation and Magnetic Order of CaFeO₃ under High Pressure up to 65 GPa. *J. Phys. Soc. Jpn.* **2001**, *70* (6), 1491–1494.
- (162) Mueller, D. N.; Machala, M. L.; Bluhm, H.; Chueh, W. C. Redox Activity of Surface Oxygen Anions in Oxygen-Deficient Perovskite Oxides During Electrochemical Reactions. *Nat. Commun.* **2015**, *6*, 6097.
- (163) Hirai, K.; Kan, D.; Ichikawa, N.; Mibu, K.; Yoda, Y.; Andreeva, M.; Shimakawa, Y. Strain-Induced Significant Increase in Metal-Insulator Transition Temperature in Oxygen-Deficient Fe Oxide Epitaxial Thin Films. *Sci. Rep.* **2015**, *5*, 7894.
- (164) Mastrikov, Y. A.; Merkle, R.; Heifets, E.; Kotomin, E. A.; Maier, J. Pathways for Oxygen Incorporation in Mixed Conducting Perovskites: A DFT-Based Mechanistic Analysis for (La, Sr)MnO₃–δ. *J. Phys. Chem. C* **2010**, *114* (7), 3017–3027.
- (165) Das, T.; Qi, Y.; Nicholas, J. D. In Preparation.
- (166) ten Elshof, J. E.; Lankhorst, M. H. R.; Bouwmeester, H. J. M. Chemical Diffusion and Oxygen Exchange of La_{0.6}Sr_{0.4}Co_{0.6}Fe_{0.4}O₃–δ. *Solid State Ionics*. **1997**, *99* (1–2), 15–22.
- (167) Mosleh, M.; Søgaard, M.; Hendriksen, P. V. Kinetics and Mechanisms of Oxygen Surface Exchange on La_{0.6}Sr_{0.4}FeO₃ – δ Thin Films. *J. Electrochem. Soc.* **2009**, *156* (4), B441–B457.
- (168) Søgaard, M.; Vang Hendriksen, P.; Mogensen, M. Oxygen Nonstoichiometry and Transport Properties of Strontium Substituted Lanthanum Ferrite. *J. Solid State Chem.* **2007**, *180* (4), 1489–1503.
- (169) Søgaard, M.; Bieberle-Hütter, A.; Hendriksen, P. V.; Mogensen, M.; Tuller, H. L. Oxygen Incorporation in Porous Thin Films of Strontium Doped Lanthanum Ferrite. *J. Electroceramics* **2011**, *27* (3–4), 134–142.
- (170) Chroneos, A.; Yıldız, B.; Tarancón, A.; Parfitt, D.; Kilner, J. A. Oxygen Diffusion in Solid Oxide Fuel Cell Cathode and Electrolyte Materials: Mechanistic Insights from Atomistic Simulations. *Energy Environ. Sci.* **2011**, *4* (8), 2774.
- (171) Wærnhus, I.; Grande, T.; Wiik, K. Surface Exchange of Oxygen in La_{1-x} Sr_x FeO₃–δ (x = 0, 0.1). *Top. Catal.* **2011**, *54* (13–15), 1009–1015.

- (172) Loschen, C.; Carrasco, J.; Neyman, K. M.; Illas, F. First-Principles LDA + U and GGA + U Study of Cerium Oxides: Dependence on the Effective U Parameter. *Phys. Rev. B* **2007**, *75* (3).
- (173) Shi, S.; Tang, Y.; Ouyang, C.; Cui, L.; Xin, X.; Li, P.; Zhou, W.; Zhang, H.; Lei, M.; Chen, L. O-Vacancy and Surface on CeO₂: A First-Principles Study. *J. Phys. Chem. Solids* **2010**, *71* (5), 788–796.
- (174) Yavo, N.; Noiman, D.; Wachtel, E.; Kim, S.; Feldman, Y.; Lubomirsky, I.; Yeheskel, O. Elastic Moduli of Pure and Gadolinium Doped Ceria Revisited: Sound Velocity Measurements. *Scr. Mater.* **2016**, *123*, 86–89.
- (175) Bishop, S. R.; Duncan, K. L.; Wachsman, E. D. Defect Equilibria and Chemical Expansion in Non-Stoichiometric Undoped and Gadolinium-Doped Cerium Oxide. *Electrochimica Acta* **2009**, *54* (5), 1436–1443.
- (176) Khare, A.; Shin, D.; Yoo, T. S.; Kim, M.; Kang, T. D.; Lee, J.; Roh, S.; Jung, I.-H.; Hwang, J.; Kim, S. W.; Noh, T. W.; Ohta, H.; Choi, W. S. Topotactic Metal-Insulator Transition in Epitaxial SrFeO_x Thin Films. *Adv. Mater.* **2017**, 1606566.
- (177) Amow, G.; Skinner, S. J. Recent Developments in Ruddlesden–Popper Nickelate Systems for Solid Oxide Fuel Cell Cathodes. *J. Solid State Electrochem.* **2006**, *10* (8), 538–546.
- (178) Mori, K.; Kamiyama, T.; Kobayashi, H.; Torii, S.; Izumi, F.; Asano, H. Crystal Structure of Sr₃Fe₂O₇–δ. *J. Phys. Chem. Solids* **1999**, *60* (8–9), 1443–1446.
- (179) Adler, P. Electronic State, Magnetism, and Electrical Transport Behavior of Sr₃–xAxFe₂O₇(X≤0.4,A=Ba, La). *J. Solid State Chem.* **1997**, *130* (1), 129–139.
- (180) Maljuk, A.; Stempfer, J.; Ulrich, C.; Sofin, M.; Capogna, L.; Lin, C. T.; Keimer, B. Growth of Sr₃Fe₂O₇–x Single Crystals by the Floating Zone Method. *J. Cryst. Growth* **2004**, *273* (1), 207–212.